

NOVEL VIBRATIONAL ENERGY HARVESTERS UTILIZING  
PIEZOELECTRIC Li-DOPED ZnO NANOWIRES AND THE  
TRIBOELECTRIC EFFECT

by

H M ASHFIQUL HAMID

Ph.D. DISSERTATION

Presented to the Faculty of the Graduate School of  
The University of Texas at Arlington in Partial Fulfillment  
of the Requirements for the Degree of

DOCTOR OF PHILOSOPHY

THE UNIVERSITY OF TEXAS AT ARLINGTON

August 2020

Copyright © by H M Ashfiqul Hamid, 2020

All Rights Reserved



## Acknowledgements

To the greatest extent, I am forever indebted to my PhD supervisor Dr. Zeynep Celik-Butler for providing me the opportunity to work under her on the cutting-edge research projects on semiconductor and nanotechnology. Her astute guidance, as well as confidence and patience towards me, were my primary sources of motivation for this dissertation. Her ideas, instructions, and professionalism will always have a profound influence on my academic and professional careers as well as on my personality traits.

I would also like to appreciate the time, reviews, and guidance provided by my PhD dissertation committee members, Dr. Robert Magnusson, Dr. Michael Vasilyev, Dr. Weidong Zhou, and Dr. Yuze Sun towards my dissertation. I also thank the Electrical Engineering Department of the University of Texas at Arlington for giving me the opportunity to teach and conduct lab sessions inside the Nanotechnology Research Center cleanroom as an instructor of the Silicon IC Fabrication Technology (EE 5343) course.

I am grateful to the Shimadzu Institute Nanotechnology Research Center staffs including the facility manager Dr. Nader Hozhabri, Richard Kevin Chambers, Dennis Bueno, Huan Nguyen, and Paul C. Logan. From basic training sessions on different equipment inside the cleanroom to the process recipe development and troubleshooting, they helped me in every step of the fabrication section of my research projects. I also express my appreciation to my fellow colleagues Dr. Bhargav P. Nabar, Dr. Yi Li, Dr. Md. Sohail Mahmood, Dr. Sajeeb Rayhan, Dr. Sk Rubayat Tousif, Dr. Shamsur Rouf, and Tanvir Ahmed for valuable inputs to my research as well as warm friendship and personal memories in the lab.

Finally and most importantly, I thank my parents, Dr. Md. Abdul Hamid and Hamida Akter Hamid for constantly inspiring me in every aspect of my professional life and for inspiring me to dream big. My father earned his PhD back in 1995. It is a moment of pride for me that I am being able to follow his footsteps after 25 years. I also thank my sister Akter Hamid Jerin and my brother-in-law A. T. M. Mahfuzar Rahman for their motivations and prayers. Lastly, I thank my dearest friends Gangotree Chakma, Partha

Sarathi Paul, Rakibul Islam, Saber Nazim Abeer, Ahmad Imraan, and Adib Shaftab Eram for cheering me all the time during my PhD life.

May, 2020

## **Abstract**

# *Novel Vibrational Energy Harvesters Utilizing Piezoelectric Li-doped ZnO Nanowires and the Triboelectric Effect*

H M Ashfiqul Hamid, PhD

The University of Texas at Arlington, 2020

Supervising Professor: Dr. Zeynep Celik-Butler

Vibration sources are omnipresent everywhere in our regular lives including the automobiles, aircraft, human body motion, wind flow, and water waves. Vibrational energy harvesters are electromechanical systems that can convert the ambient vibrations into electrical energy which can be stored to power up small scale electronic devices, essentially converting them into self-powered systems. The electronics industry has always propelled towards the scaling of electronic devices for improved flexibility and reduced production cost. This scaling, combined with the power-efficient designs, is widening the scope of applications for the energy harvesters. For instance, the vibrational energy harvesters have substantial applications in small scale sensor nodes, wearable electronics, robotics and prosthetics systems, mobile and implantable medical devices as well as in many other electronic systems.

This dissertation presents the design, fabrication, and characterization of two such vibrational energy harvesting systems: the first one being a piezoelectric energy harvesting system based on Li-doped ZnO nanowires (NWs); and the second one being a microelectromechanical systems (MEMS) scale triboelectric energy harvesting system with high operating frequency and wide frequency bandwidth.

A complete investigation of the effect of Li doping on the physical, material, electromechanical, and piezoelectric properties of ZnO NWs is presented in the first project. Low-temperature hydrothermal growth technique is used to grow vertically aligned crystalline ZnO NWs doped with different concentrations of Li. Characterization techniques reveal considerable physical, material, and electromechanical property modifications of the ZnO NWs due to the incorporation of Li dopants. Atomic Force Microscope (AFM) is utilized to apply a controlled amount of force on the fabricated NWs to assess their piezoelectric response. More than twenty two-fold improvement is observed in the sensitivity due to the combined effect of modifications in NW geometry and piezoelectric properties with the addition of Li. Finite element method simulations were performed to decouple the individual effect of Li doping on the NW size and on the piezoelectric coefficient as well as to see how much each effect plays a role in the sensitivity improvement. It is estimated that the changes in the material and electromechanical properties alone are responsible for more than seven-fold improvement in the sensitivity. The impact of the ‘kick-out’ diffusion mechanism of Li in ZnO is one of the major factors responsible behind this sensitivity improvement. It is also observed that there is an optimum level of Li doping concentration which can lead to the best piezoelectric performance by the ZnO NWs. The novelty of this work lies in the detailed analyses to illustrate the physics and impact of Li dopants in ZnO NW structures from a piezoelectric point of view towards improving their application as a nano-sensing and nano-energy harvesting element.

For the second project, a novel triboelectric energy harvesting (TEH) and sensing system scaled down to MEMS size is presented. The design is structurally optimized for harvesting the highest average power and power density while ensuring the structural robustness. Unlike traditional triboelectric energy harvesters, this design results in a high operating frequency with a wide bandwidth. Adoption of MEMS

fabrication techniques including the use of spin-coated Teflon AF rather than a Teflon sheet, adaptation of UV-LIGA (Ultra-Violet Lithographie, Galvanoformung, Abformung) with modifications and implementation of a thick polyimide sacrificial layer make the fabrication process unique. If excited by  $\pm 9.33g$  external vibration with a frequency of 1150 Hz, the TEH can generate 0.179  $\mu W$  average power and 0.597  $\mu W$  peak power at an optimum resistive load of 256 k $\Omega$ . The peak surface power density, volumetric power density and acceleration-normalized volumetric power density reach 3.98  $\mu W cm^{-2}$ , 2.64 mWcm $^{-3}$  and 30.3  $\mu W cm^{-3}/g^2$ , respectively. While the surface power density of the presented TEH is moderate, the volumetric power density and acceleration-normalized volumetric power density are quite competitive among the state-of-the-art designs. The TEH also demonstrates a wide operating frequency bandwidth of 920 Hz. If operated as an accelerometer, the device shows a linear sensitivity of 43 mV/g. Although the simulation predicts the optimum operating frequency and load resistance of the system to be at 800 Hz and 10 M $\Omega$ , respectively, the experimental results demonstrate these values to be at 1150 Hz and 256 K $\Omega$ . A few fabrication anomalies, most notably the notching in the Teflon layer and bowing of the proof-mass, are responsible for this deviation. In addition, a distortion is observed in the simulated output voltage profile which is not present in the experimental output voltage profile due to the presence of the parasitic capacitance in the experimental circuit. The aforementioned triboelectric energy harvester can have specific applications in the sensor and actuator systems in the aircraft industry as well as in the automobile industry, micro-robotic systems, prosthetic systems, and sensor nodes in the internet of things (IoT) based on its operating frequency and bandwidth range.

# Table of Contents

Acknowledgements.....	iii
Abstract.....	v
Table of Contents.....	viii
List of Illustrations.....	xiii
List of Tables.....	xxii
List of Symbols.....	xxiii
List of Acronyms.....	xxvii
Chapter 1 : Introduction.....	1
1.1.    Overview of vibrational energy harvesting.....	1
1.1.1.    Motivations for vibrational energy harvesting.....	1
1.1.2.    Sources of vibrations.....	3
1.1.3.    Applications of vibrational energy.....	4
1.2.    Types of vibrational energy harvesters.....	6
1.2.1.    Electromagnetic energy harvesters.....	6
1.2.2.    Electrostatic energy harvesters.....	7
1.2.3.    Piezoelectric energy harvesters.....	8
1.2.4.    Triboelectric energy harvesters.....	9
1.3.    Review of ZnO nanowire based piezoelectric energy harvesters and nano-sensors.....	10
1.3.1.    Review of ZnO as a piezoelectric energy harvesting material.....	10



1.3.2.	Vibrational energy harvesters based on ZnO nanowires.....	14
1.3.3.	Nano-sensors based on ZnO nanowires .....	17
1.3.4.	Motivations for Li doping into ZnO nanowires .....	19
1.3.5.	Challenges associated with Li doping into ZnO nanowires.....	20
1.4.	Review of triboelectric energy harvesters .....	20
1.4.1.	Overview of the triboelectric effect .....	20
1.4.1.1.	Origin of the triboelectric effect .....	20
1.4.1.2.	Selection of the triboelectric pair of materials.....	22
1.4.2.	Operating modes of triboelectric energy harvesters.....	23
1.4.2.1.	Vertical contact separation mode.....	23
1.4.2.2.	In-plane sliding mode .....	24
1.4.2.3.	Single electrode mode .....	24
1.4.2.4.	Freestanding triboelectric layer mode .....	25
1.4.3.	Motivations for a high operating frequency, wide bandwidth MEMS scale triboelectric energy harvester.....	26
1.4.4.	Challenges associated with high operating frequency, wide bandwidth MEMS scale triboelectric energy harvester.....	27
1.5.	Organization of this dissertation.....	28
Chapter 2 : Piezoelectric Energy Harvester Based on Li-doped ZnO Nanowires .....		29
2.1.	Introduction .....	29
2.2.	Fabrication of the Li-doped ZnO nanowire carpet .....	30

2.2.1.	Fabrication process flow .....	30
2.2.2.	Hydrothermal growth process .....	32
2.3.	Characterization of the nanowires .....	35
2.3.1.	Physical property characterization .....	35
2.3.1.1.	Length variation characterization .....	35
2.3.1.2.	Diameter and density variation characterization .....	36
2.3.1.3.	Summary.....	37
2.3.2.	Material and electromechanical property characterization .....	41
2.3.2.1.	Raman spectroscopic analysis .....	41
2.3.2.2.	X-Ray Diffractometric (XRD) analysis.....	43
2.3.2.3.	Energy Dispersive Spectroscopic (EDS) analysis .....	44
2.3.2.4.	X-ray Photoelectron Spectroscopic (XPS) analysis.....	45
2.3.2.5.	Summary.....	45
2.3.3.	Piezoelectric response characterization.....	47
2.3.3.1.	Piezoelectric characterization setup.....	47
2.3.3.2.	Piezoelectric characterization results.....	52
2.3.3.3.	Summary.....	55
2.4.	Piezoelectric performance simulation .....	56
2.4.1.	Average nanowire displacement simulation in Coventorware™ .....	56
2.4.2.	Piezoelectric response simulation in Ansys™.....	57
2.4.3.	Comparison between the experimental measurement and simulation .....	60

2.4.4.	Summary .....	60
2.5.	Analyses and discussions .....	61
2.6.	Performance comparison table .....	65
2.7.	Conclusion.....	67
Chapter 3 : MEMS Scale Triboelectric Energy Harvester with High Operating Frequency and Wide		
	Bandwidth.....	68
3.1.	Introduction.....	68
3.2.	Design and modeling of the triboelectric energy harvester .....	69
3.2.1.	Modeling of the triboelectric energy harvester.....	69
3.2.2.	Optimization of the triboelectric energy harvester .....	74
3.2.3.	Triboelectric energy harvester structure and spring design .....	79
3.2.4.	Stress analysis.....	82
3.2.5.	Summary.....	83
3.3.	Fabrication of the triboelectric energy harvester .....	83
3.4.	Characterization of the triboelectric energy harvester .....	90
3.4.1.	Characterization setup .....	90
3.4.2.	Frequency response and load resistance optimization.....	90
3.4.3.	Bandwidth widening.....	95
3.4.4.	Summary.....	95
3.5.	Analyses and discussions.....	96
3.5.1.	Back simulation with measured structural parameters .....	96

3.5.2. Shifting of the optimum operating condition.....	99
3.5.3. Distortion of the simulated output voltage signal.....	101
3.5.4. Summary.....	104
3.6. Comparison of the triboelectric energy harvester performance with the state-of-the-art .....	104
3.7. Conclusion .....	108
Chapter 4 : Conclusion.....	109
4.1. Piezoelectric performance modification of ZnO nanowires with controlled incorporation of substitutional Li doping.....	109
4.2. A MEMS scale triboelectric energy harvester with high operating frequency and wide bandwidth fabricated using UV LIGA technique.....	110
4.3. Applications.....	111
Appendix A : Derivation of the circuit model for AFM tip-nanowire interaction.....	113
Appendix B : Coventorware™ settings for the ZnO nanowire displacement simulation.....	115
Appendix C : Ansys™ settings for the ZnO nanowire piezoelectric response simulation .....	118
Appendix D : Mask layout for the triboelectric energy harvester.....	121
Appendix E : Coventorware™ settings for the triboelectric energy harvester performance simulation...	123
References.....	126
Biographical Information.....	145

## List of Illustrations

Figure 1.1: Technology roadmap of vibrational energy harvesters and nanogenerators proposed by Wang [3] (Reprinted with permission. Copyright © 2014, Royal Society of Chemistry).....	2
Figure 1.2: The impact of Maxwell's displacement current equation on fundamental science, technology and engineering field [5] (Reprinted with permission. Copyright © 2017, Elsevier) .....	3
Figure 1.3: Designs of vibrational energy harvesters harvesting energy from (a) Human motion [39] (Reprinted with permission. Copyright © 2017, John Wiley and Sons) (b) Textile fabric [40] (Reprinted with permission. Copyright © 2015, John Wiley and Sons) (c) Water wave [17] (Reprinted with permission. Copyright © 2014, American Chemical Society) (d) Wind [14] (Reprinted with permission. Copyright © 2013, American Chemical Society) (e) Tire of a car [29]. (Reprinted with permission. Copyright © 2018, Elsevier).....	5
Figure 1.4: (a) Schematic of a typical electromagnetic energy harvesting system [42] (Reprinted with permission. Copyright © 2009, Springer-Verlag). (b) A cantilever based electromagnetic energy harvesting system [43] (Reprinted with permission. Copyright © 2008, Elsevier).....	7
Figure 1.5: Design of an electrostatic energy harvester [44] (Reproduced with permission. Copyright © 2009, IOP Publishing) .....	8
Figure 1.6: Design of a nanowire based piezoelectric energy harvester [45] (Reprinted with permission. Copyright © 2008, American Chemical Society).....	9
Figure 1.7: Design of a triboelectric energy harvester with Al and PTFE as the triboelectric materials pair [49] (Reprinted with permission. Copyright © 2013, American Chemical Society).....	10

Figure 1.8: Hexagonal Wurtzite crystal structure of ZnO. White and yellow balls represent  $Zn^{2+}$  and  $O^{2-}$  ions, respectively [50]..... 11

Figure 1.9: Nanostructure configurations of ZnO [53] (Reprinted with permission. Copyright © 2004, Elsevier) ..... 13

Figure 1.10: Energy harvester design by Wang et al. (a) – (b) Hydrothermally grown vertically aligned ZnO nanowires. (c) Characterization schematic. An AFM tip is operated in contact mode to horizontally scan and apply force on the nanowires [1] (Reprinted with permission. Copyright © 2006, The American Association for the Advancement of Science) ..... 14

Figure 1.11: Design of a piezoelectric vibrational energy harvester with bulk micro machined pyramidal shaped proof-mass. Zoomed in and cross sectional view of the proof mass, spring and nanowire arrays are also displayed [58] (Reprinted with permission. Copyright © 2014, Elsevier) ..... 16

Figure 1.12: Design of a piezoelectric vibrational harvester where energy is generated from the compression of the ZnO nanowires. The proof-mass compresses the nanowires in vertical direction when subject to vibrations. Figures describe (a) overview (b) cross section and (c) schematic of the design [59] (Reprinted with permission. Copyright © 2016, Elsevier) ..... 17

Figure 1.13: Design of a flexible tactile and pressure sensor. ZnO NWs are sandwiched between the flexible substrate and superstrate. The NWs generate output signal when subject to a pressure through the flexible substrate [31] (Reprinted with permission. Copyright © 2015, IEEE)..... 18

Figure 1.14: Examples of the triboelectric effect in regular life. (a) Comb attracting paper pieces just after a hair brush [90]. (b) Electric shock while grabbing a car door due to the static charge on human skin [91]. ..... 22

Figure 1.15: Undesirable impacts of the triboelectric effect. (a) Wildfire from triboelectric spark [94]. (b) Damage in IC from electrostatic discharge [95]. (c) Communication disturbance from aircraft because of the triboelectric charge accumulation on their body [96]. ..... 22

Figure 1.16: Triboelectric series representing the relative electron affinity between materials [98]. ..... 23

Figure 1.17: Schematic and applications of the four basic operational modes of the triboelectric energy harvesters. (a) Vertical contact separation mode. (b) In-plane sliding mode. (c) Single electrode mode. (d) Freestanding triboelectric layer mode [3] (Reprinted with permission. Copyright © 2014, Royal Society of Chemistry) ..... 26

Figure 2.1: Fabrication process flow for the Li-doped ZnO nanowire device. (a) Deposition of the Si<sub>3</sub>N<sub>4</sub> insulation/passivation layer over a Si wafer. (b) Deposition of 30 nm Cr adhesion and 100 nm Au layers as the bottom electrode. (c) Patterning of the bottom electrode. (d) Deposition of 30 nm Ti Ohmic contact layer and 300 nm ZnO seed layer. (e) Patterning of the Ti/ZnO seed layer. (f) Formation of SU-8 template layer (g) Hydrothermal growth of the undoped or Li-doped ZnO NWs and removal of the SU-8 layer. .... 31

Figure 2.2: SEM image of five NW patches taken after the fabrication of the device. The NW patches are 8×8 μm<sup>2</sup> in size. Each of the fabricated devices contains at least 90 of such NW patches. .... 32

Figure 2.3: Experimental setup for the hydrothermal growth process..... 34

Figure 2.4: (a) – (e) SEM images of the NW patches with the stage tilted at 45°. (a) ZnO-10-10-0 (b) ZnO-10-10-7 (c) ZnO-10-10-10 (d) ZnO-10-10-15 (e) ZnO-10-10-25. .... 38

Figure 2.5: (a) – (e) SEM images of the NW patches without tilting the stage. (a) ZnO-10-10-0 (b) ZnO-10-10-7 (c) ZnO-10-10-10 (d) ZnO-10-10-15 (e) ZnO-10-10-25. .... 39

Figure 2.6: (a) Variation of average NW length and diameter with Li doping concentration. Here, ZnO NWs were assumed to have a circular cross-section instead of the hexagonal in reality. (b) Variation in the average density of NWs with Li doping concentration..... 40

Figure 2.7: NW patch topography from the ZnO-10-10-25 sample created using the tapping mode of an AFM system..... 40

Figure 2.8: A typical line scan profile for the ZnO-10-10-25 sample from the AFM topography using the tapping mode. .... 41

Figure 2.9: (a) A sample Raman spectrum from the ZnO-10-10-0 sample. (b) E2-high Raman active mode position with Li doping concentration. A red shift is observed in this mode due to the incorporation of Li..... 42

Figure 2.10: XRD analysis results on the fabricated NW devices. (a) A sample XRD spectrum from the ZnO-10-10-0 device. (b) High resolution scan around the (0002) peak position. (c) Vertical lattice constant  $c$  variation with Li doping concentration. (d) Crystallite size variation with Li doping concentration..... 44

Figure 2.11: XPS scan around the Li 1s peak position for the ZnO-10-10-10 device. Core level Li 1s peak is observed around 53 eV ~ 54 eV binding energy for all of the doped devices. .... 45

Figure 2.12: SEM image of the Au coated AFM cantilever tip. In addition to applying mechanical excitation to the NWs, the tip also acted as the top electrode for the nanowire devices. (a) AFM tip. (b) AFM tip with cantilever [147]. .... 48

Figure 2.13: Schematic illustration of an AFM tip - NW interaction for the  $d_{31}$  mode. When the NWs are bent, a positive voltage is generated in the side that experiences a tensile stress. On the other hand, negative voltage is generated on the compressively stressed side. .... 49



Figure 2.14: Piezoelectric response measurement setup.....	49
Figure 2.15: Schematic of the AFM cantilever deflection measurement system [58] (Reprinted with permission. Copyright © 2013, Elsevier). .....	50
Figure 2.16: A sample force plot for the AFM tip-nanowire interaction. X axis represents the vertical movement of the AFM tip and the Y axis represents the deflection of the AFM cantilever. For this particular curve, trigger voltage or set point was set to 6V. ....	52
Figure 2.17: Sample piezoelectric output response from the NW devices. An AFM tip was used to apply force on the NWs. Only the $d_{31}$ mode or the positive voltages are analyzed which are associated with the bending of the NWs. The labels for the x-axis are staggered for clarity.....	54
Figure 2.18: Sample log-transformed distribution curves for the piezoelectric output voltage measured on (a) ZnO-10-10-0 and (b) ZnO-10-10-7 samples. Log transformation is implemented to remove the effect of skewness and perform a more accurate statistical analysis. ....	54
Figure 2.19: Average measured generated voltage $\langle V_g \rangle'$ and force-normalized average measured generated voltage $\langle V_g \rangle'_{FN}$ from NWs with respect to doping concentration. $\langle V_g \rangle'_{FN}$ also represents the sensitivity of the NWs. More than 22-fold improvement in the sensitivity is observed due to the incorporation of Li dopants into the ZnO NWs. ....	55
Figure 2.20: (a) – (b) A sample Coventorware™ simulation result for the displacement of the NWs due to the applied force by the AFM tip. (a) Displacement in the entire model. (b) Displacement of the AFM tip and NWs only (zoomed image of (a))......	57
Figure 2.21: Equivalent circuit model for the AFM tip-NW interaction system. ....	58
Figure 2.22: Sample simulation result in Ansys™ showing the piezoelectric output response of a single NW due to the average displacement calculated from Coventorware™ simulations. ....	59

Figure 2.23: Force-normalized simulated piezoelectric output voltage  $\langle V_S \rangle_{FN}$ . Bulk ZnO material properties are used for all of the simulations regardless of the doping concentration. .... 59

Figure 2.24: Comparison of the measured and simulated piezoelectric voltage generated in response to force applied by the AFM tip. For the ZnO-10-10-0 sample, the value of  $\langle V_g \rangle'_{FN} / \langle V_S \rangle_{FN}$  is very close to 1, indicating the close match for our experimental and simulated values. As for all the simulations, the bulk ZnO material properties are used regardless of the doping concentration. Therefore, the values of  $\langle V_g \rangle'_{FN} / \langle V_S \rangle_{FN}$  higher than one are due to the improvement in the piezoelectric response. .... 61

Figure 3.1: Schematic of the TEH for vertical contact separation mode operation. The equivalent circuit of the system is depicted in the inset. .... 71

Figure 3.2: Frequency and load resistance sweep to determine the optimum operating condition in terms of average power. The optimum condition is found to be at 800 Hz frequency and 10 MΩ load resistance. .... 77

Figure 3.3: TEH system response at the optimum simulated operating condition of 800 Hz frequency and 10 MΩ load resistance. (a) Displacement of the suspended structure. (b) Transferred charge and device output voltage profile. (c) Device output power profile. .... 78

Figure 3.4: Structural model of the optimized triboelectric energy harvester. (a) Top view. (b) Tilted view. .... 80

Figure 3.5: (a) Generalized displacement for the vibration modes of the triboelectric energy harvesting system obtained from the modal harmonic analysis. (b) Primary vibration mode (mode 1) of the system is a vertical motion. .... 81

Figure 3.6: Stress analysis on the device model with 50g input acceleration. The maximum von Mises stress shown here at a close-up view is less than the yield strength of all materials, Au, Al and Ni.

..... 82

Figure 3.7: Complete fabrication process flow of the triboelectric energy harvester ..... 86

Figure 3.8: EDS analysis of the ashing of the HD4110 sacrificial polyimide. (a) Before the ashing of the HD4110 polyimide. Spot 1 shows the dominant presence of the C and O atoms which are the constituent atoms of the HD4110 polyimide. Spot 2 demonstrates the dominant presence of Ni which constitutes the anchor for the proof-mass. (b) After the completion of the HD4110 polyimide ashing. Spot 1 shows the dominant presence of the Si and N atoms which constitute the  $Si_3N_4$  passivation layer. The presence of O is also seen at spot 1 which possibly comes from the native oxidation. On the other hand, spot 2 demonstrates the dominant presence of C, O, and F atoms which constitute Teflon. The detection of  $Si_3N_4$  and Teflon verifies that the HD4110 polyimide ashing is complete. Finally, spot 3 demonstrates the presence of Ni anchor for the proof-mass. .... 87

Figure 3.9: SEM image of a part of the triboelectric energy harvester. The stage was tilted at  $45^\circ$ .

..... 88

Figure 3.10: SEM images to observe the bowing of the proof-mass due to residual stress. The stage is tilted at  $45^\circ$ . (a) Near the center of the proof-mass. (b) Near the edge of the proof-mass..... 89

Figure 3.11: Block diagram of the characterization setup for the triboelectric energy harvesting system ..... 91

Figure 3.12: Load resistance and frequency sweep to determine the experimental optimum operating condition in terms of average power per acceleration. The experimental optimum condition is found at 1150 Hz frequency and 256 K $\Omega$  load resistance. .... 92

Figure 3.13: Response from the system at the experimental optimum operating condition. (a) Output voltage from the TEH corresponding to the input acceleration. (b) Output power from the TEH corresponding to the input acceleration. .... 93

Figure 3.14: The phase-corrected output response from the characterization of the triboelectric energy harvester. .... 94

Figure 3.15: Phase-corrected output voltage vs acceleration plot. The response is linear with a sensitivity of  $43 \text{ mVg}^{-1}$  ..... 94

Figure 3.16: SEM image of the bottom triboelectric layer (Teflon) thickness after the Ar plasma etching. The SEM stage was tilted at  $45^{\circ}$  angle. .... 97

Figure 3.17: SEM image of the suspended structure for (a) perforation radius and (b) unit cell radius ..... 98

Figure 3.18: SEM image of the thickness of the suspended structure. The SEM stage was tilted by  $45^{\circ}$  ..... 99

Figure 3.19: Variation of the optimum load resistance with the effective Teflon layer thickness and air gap. .... 100

Figure 3.20: Initial model parameters. The system is simulated at 800 Hz vibration frequency and 1g acceleration. (a) System capacitances. (b) The resultant characteristic electrical frequency of the circuit ( $1/RC_{ideal}$ ) for  $R = 10 \text{ M}\Omega$  and the mechanical vibration frequency of the system ( $\omega$ ) ..... 102

Figure 3.21: The same system in Fig. 3.20 is simulated at the vibration frequency of 2852 Hz and 1g acceleration. (a) The resultant characteristic electrical frequency of the circuit ( $1/RC_{ideal}$ ) for  $R = 10 \text{ M}\Omega$  and the mechanical vibration frequency of the system ( $\omega$ ). (b) TEH output charge and voltage profiles, showing no distortion..... 103

Figure 3.22: Equivalent circuit model of the triboelectric energy harvester. (a) Ideal circuit model.	
(b) Parasitic capacitance model.....	104
Figure A.1: Circuit model for the AFM tip-nanowire interaction .....	113
Figure B.1: Material properties of ZnO in Coventorware™.....	116
Figure B.2: Process flow in Coventorware™ .....	117
Figure B.3: MemMech solver settings in Coventorware™ .....	117
Figure C.1: Element type selection in Ansys™ .....	118
Figure C.2: Material property setting for ZnO nanowire in Ansys™ .....	120
Figure D.1: Mask layout designs for the triboelectric energy harvester. (a) Bottom electrode mask	
(b) Teflon layer mask (c) Anchor mask (d) Anchor_spring_proofmass mask (e) All of the masks combined.	
.....	122
Figure E.1: Coventorware™ settings for the triboelectric energy harvester modal harmonic	
analysis.....	124
Figure E.2: Coventorware™ settings for the triboelectric energy harvester stress analysis. ....	125

## List of Tables

Table 1.1: Primary vibration mode frequencies of mechanical vibration sources [6], [7], [8] .....	4
Table 2.1: Concentrations of the chemical ingredients in hydrothermal growth solution. Molar weights of Zn(CH <sub>3</sub> COO) <sub>2</sub> , HMTA and LiCH <sub>3</sub> COO are 219.51, 140.19 and 102.02 g/mol, respectively. .	35
Table 2.2: Parameters used for the construction of the NW model in Coventorware™ simulations and the resultant NW displacement values .....	57
Table 2.3: Summary of recently reported undoped and doped ZnO nanowire piezoelectric performance .....	66
Table 3.1: Summary of the structurally optimized parameters for the triboelectric energy harvester .....	76
Table 3.2: Serpentine spring parameters.....	79
Table 3.3: Performance comparison of the presented TEH with the state of the art designs from literature .....	106

## List of Symbols

<i>Annotation</i>	<i>Description</i>	<i>Unit</i>
$a(t)$	Acceleration	$\text{ms}^{-2}$
$C_{air}$	Capacitance between the two triboelectric layers	F
$C_{device}$	Capacitance between the bottom electrode and bottom triboelectric layer	F
$C_{ideal}$	Total capacitance for the ideal capacitance model	F
$C_{par}$	Parasitic capacitance	F
$C_{total}$	Total capacitance for the parasitic capacitance model	F
$c$	Vertical lattice constant	Å
$c_{pq}$	Elastic constant matrix	GPa
$D$	Electric displacement field	$\text{C/m}^2$
$D_i$	Electric displacement	$\text{C/m}^2$
$d_{cant}$	Deflection of the cantilever	m
$d_2$	Thickness of the bottom triboelectric layer	m
$E$	Electric field	V/m
$E_k$	Electric field	V/m
$e_{kp}$	Piezoelectric coefficient matrix	$\text{C/m}^2$
$emf$	Electromotive force	V
$F$	Applied force	N
$\langle F_{AFM} \rangle$	Average applied force by the AFM	N

$F_d$	Squeeze film damping force	N
$F_e$	Electrostatic force between the triboelectric layers	N
$F_s$	Force applied by the spring on the suspended assembly	N
$f$	Frequency	Hz
$g$	Gravitational acceleration	$\text{ms}^{-2}$
$H$	Thickness of the suspended assembly	m
$H_{pm}$	Thickness of the proofmass	m
$H_{tml}$	Thickness of the top triboelectric metal layer	m
$h(t)$	Air gap between the triboelectric layers	m
$I_{sc}$	Short circuit current	A
$J_D$	Displacement current density	$\text{A/m}^2$
$K_n$	Knudsen number	
$k$	Spring constant	N/m
$k_{cant}$	Spring constant of the cantilever	N/m
$k_z$	Spring constant in z direction	N/m
$Li_{Zn}$	Substitutional Li in ZnO structure	–
$Li_i$	Interstitial Li in ZnO structure	–
$l_{pm}$	Length of the triboelectric layers	m
$m$	Mass of the suspended assembly	Kg
$P_{avg}$	Average power	W
$P_I$	Instantaneous power	W



$P_s$	Surface polarization field	C/m <sup>2</sup>
$p_a$	Ambient pressure	Pa
$p_0$	Atmospheric pressure	Pa
$Q$	Transferred charge	C
$R$	Load resistance	$\Omega$
$R_i$	Contact resistance	$\Omega$
$R_L$	Load resistance	$\Omega$
$r_c$	Radius of a unit perforation cell	m
$r_0$	Radius of a single perforation	m
$S_{eff}$	Effective triboelectric contact area	m <sup>2</sup>
$S_v$	Sensitivity of the cantilever	m/V
$t$	Time	s
$U$	Electrostatic energy	J
$V$	Voltage	V
$V_g$	Piezoelectric generated voltage	V
$\langle V_g \rangle$	Average piezoelectric generated voltage	V
$\langle V_g \rangle'$	Log transformed average measured generated voltage	V
$\langle V_g \rangle'_{FN}$	Force normalized average generated voltage	V/N
$V_{oc}$	Open circuit voltage	V
$\langle V_s \rangle$	Simulated voltage	V
$\langle V_s \rangle_{FN}$	Force normalized simulated voltage	V/N

$V_t$	Threshold voltage	V
$w_{pm}$	Width of the triboelectric layers	m
$x_0$	Initial air gap	m
$z(t)$	Displacement of the suspended structure from initial position	m
$\epsilon_0$	Vacuum permittivity	F/m
$\epsilon_q$	Mechanical strain matrix	–
$\epsilon_{r2}$	Relative permittivity of the bottom triboelectric layer	–
$\kappa_{ik}$	Dielectric constant matrix	F/m
$\lambda$	Mean free path of gas molecules	m
$\lambda_0$	Mean free path of gas molecules at atmospheric pressure	m
$\mu$	Coefficient of viscosity of air	Pa.s
$\mu_{eff}$	Coefficient of viscosity of air considering rarefaction effect	Pa.s
$v(t)$	Velocity of the suspended structure	ms <sup>-1</sup>
$\sigma$	Triboelectric charge density	C/m <sup>2</sup>
$\sigma_p$	Mechanical stress matrix	Pa
$\phi_B$	Magnetic flux	Wb
$\omega$	Mechanical motion frequency	Hz

## List of Acronyms

<i>Acronym</i>	<i>Abbreviation</i>
AFM	Atomic Force Microscopy
BTO	BaTiO <sub>3</sub>
EDS	Energy Dispersive Spectroscopy
FEM	Finite Element Method
FWHM	Full Width at Half Maximum
HMTA	Hexamethylenetetramine
IoT	Internet of Things
MEMS	Micro Electro Mechanical System
NEMS	Nano Electro Mechanical System
NW	Nanowire
PDMS	Polydimethylsiloxane
PEH	Piezoelectric Energy Harvester
PTFE	Polytetrafluoroethylene
PLD	Pulsed Laser Deposition
PVDF	Polyvinylidene Fluoride
PZT	PbZr <sub>x</sub> Ti <sub>1-x</sub> O <sub>3</sub>
RPM	Revolutions Per Minute
RIE	Reactive Ion Etching
SEM	Scanning Electron Microscopy
SNR	Signal to Noise Ratio
TEH	Triboelectric Energy Harvester

UV-LIGA	Ultra Violet Lithographie, Galvanoformung, Abformung
VEH	Vibrational Energy Harvester
XPS	X-ray Photoelectron Spectroscopy
XRD	X-Ray Diffractometer

# Chapter 1 : Introduction

## 1.1. Overview of vibrational energy harvesting

### 1.1.1. Motivations for vibrational energy harvesting

Driven by mobile and implantable medical device applications, there is a considerable technological push for nanoscale devices to be self-powered. Moreover, the electronics industry has always propelled towards the scaling of electronic devices and sensors for improved flexibility and reduced production cost. This has driven the power requirement for these devices to scale down as well. Furthermore, boosting the power efficiency has become a fundamental feature for any sort of electrical device. As a result, the power requirement for small scale electronics and sensors have gone down dramatically. For this purpose, vibrational energy harvesters (VEH) offer great promise to harvest energy from waste mechanical vibrations and make the nanoscale devices self-powered. This not only relieves the traditional battery requirement from the electronic devices, but also prolongs their reliability and longevity.

The revolution in the current vibrational energy harvesting field was pioneered by Zhong Lin Wang back in 2006 with his ZnO based piezoelectric energy harvesters (PEH) and in 2012 with his triboelectric energy harvesters (TEH) [1], [2]. Since then, the vibrational energy harvesting field is advancing even more rapidly than his initial predicted roadmap as depicted in Fig. 1.1 [3].

The origin of these sorts of energy harvesters lies in Maxwell's continuity equation for electric charges [4]. The displacement current density according to Maxwell's equation is expressed as

$$J_D = \frac{\partial D}{\partial t} = \epsilon \frac{\partial E}{\partial t} + \frac{\partial P_s}{\partial t} \quad (1.1)$$

here,  $J_D$  is the displacement current density,  $D$  is the electric displacement field,  $E$  is the electric field, and  $P_s$  is the surface polarization field.

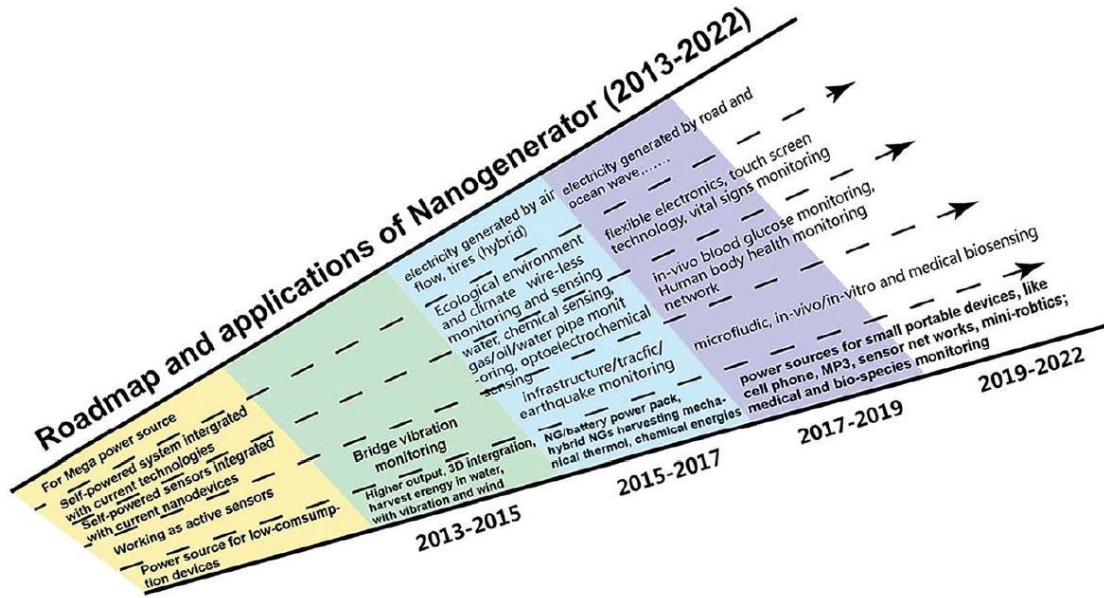


Figure 1.1: Technology roadmap of vibrational energy harvesters and nanogenerators proposed by Wang [3] (Reprinted with permission. Copyright © 2014, Royal Society of Chemistry)

The first term on the right hand side of Eq. 1.1 is induced by the varying electric field whereas the second term is induced by the polarization field due to the surface electrostatic charges. The first term gave birth to the electromagnetic wave and induction theory, which led to the invention of the antenna, radar, telegram, navigation system, wireless communication, and space technology.

On the other hand, the second term containing the polarization field due to the surface electrostatic charges is the theoretical origin for both the piezoelectric and triboelectric energy harvesters. This has given way to new energy harvesting technologies and the idea of self-powered sensors. The two branches of the tree absorbing nutrition from the fundamental Maxwell's displacement current equation is expected to grow even more swiftly in the upcoming future (Fig. 1.2) [5].

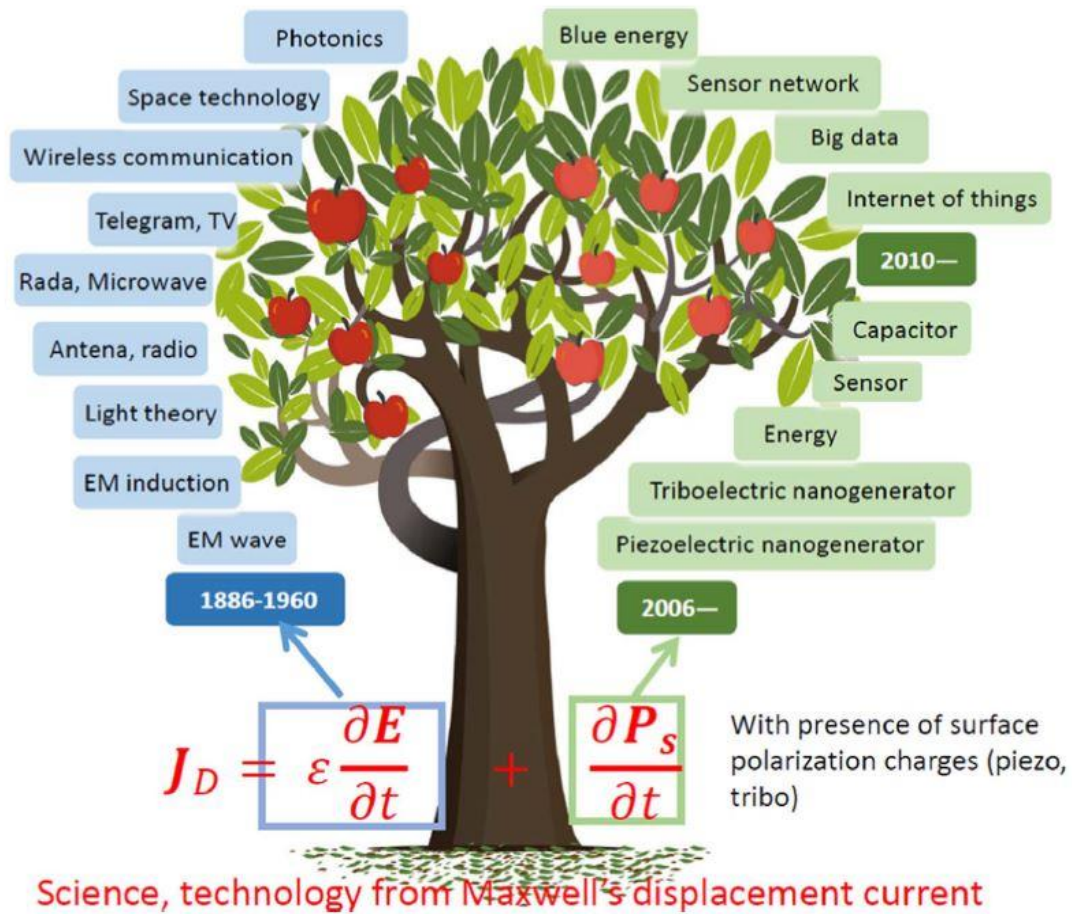


Figure 1.2: The impact of Maxwell's displacement current equation on fundamental science, technology and engineering field [5] (Reprinted with permission. Copyright © 2017, Elsevier)

### 1.1.2. Sources of vibrations

From the vibration of the vocal cords while people talk to the vibration of a car engine, vibration sources are present all around our everyday life. Typically, the vibration frequencies and amplitudes widely vary from source to source. For instance, vibrations from the human body motion usually consist of low frequencies ranging from 3 Hz to 17 Hz [6]. On the other hand, vibration from different types of machinery usually consists of higher frequencies. Nevertheless, numerous of these sources are suitable for vibrational energy harvesting applications. Examples of vibration frequencies from different mechanical vibration sources are presented in Table 1.1 [7], [8].

Table 1.1: Primary vibration mode frequencies of mechanical vibration sources [6], [7], [8]

Source of vibration	Primary mode frequency (Hz)
Car engine	200
Human motion	3 ~ 17
Blender	121
Microwave oven	121
Car instrument panel	13
Frame of door just after closing	125
Cloth dryer	121
CD on computer	75
Vents in office building	60
Window near busy road	100
Aircraft skin	800, 1500
Floor of an office building	100

### 1.1.3. Applications of vibrational energy

The applications of the vibrational energy harvesters can be substantial. For example, implantable devices like pacemakers have been reported to have energy harvesters [9], [10], [11]. Even NASA's forthcoming space exploration programs (e.g. Mars rover) are also incorporating triboelectric energy harvesters [12]. Moreover, vibrational energy harvesters are reported to be implemented to harvest energy from wind flow [13], [14], water flow [15], [16], [17], [18], [19], sound waves [20], [21], [22], human motion [23], [24], [25], [26], and tire pressure [27], [28], [29]. In addition to that, vibrational energy harvesting systems are also integrated in self-powered sensors to detect force [30], pressure [31], [32], [33], [34], vibration [35], acceleration [36], liquid volume [37], and ion concentration [38]. Illustrations of vibrational energy harvester designs from different vibration sources are presented in Fig. 1.3 [39], [40], [17], [14], [29].



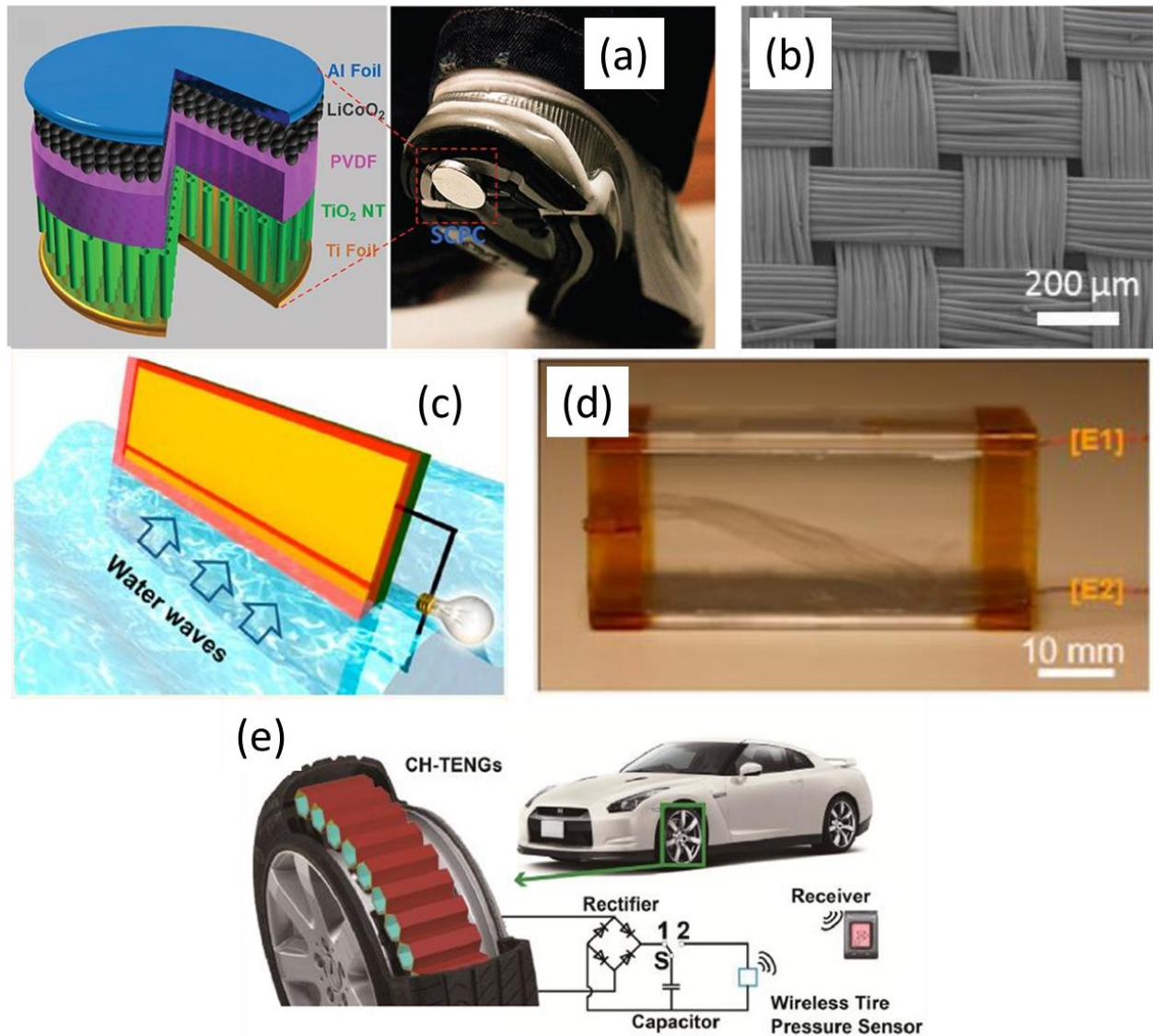


Figure 1.3: Designs of vibrational energy harvesters harvesting energy from (a) Human motion [39] (Reprinted with permission. Copyright © 2017, John Wiley and Sons) (b) Textile fabric [40] (Reprinted with permission. Copyright © 2015, John Wiley and Sons) (c) Water wave [17] (Reprinted with permission. Copyright © 2014, American Chemical Society) (d) Wind [14] (Reprinted with permission. Copyright © 2013, American Chemical Society) (e) Tire of a car [29]. (Reprinted with permission.

Copyright © 2018, Elsevier)

## 1.2. Types of vibrational energy harvesters

Depending on the working principle, the traditional VEHs are classified into four basic categories. They are electromagnetic, electrostatic, piezoelectric and triboelectric energy harvesters. Each of them has several pros and cons. A brief overview of them is presented in this section.

### 1.2.1. Electromagnetic energy harvesters

Conventional electromagnetic energy harvesters are governed by Faraday's law. The electromotive force induced to a system is equal to the rate of change of magnetic flux which is expressed as

$$emf = \left| \frac{d\phi_B}{dt} \right| \quad (1.2)$$

here,  $emf$  is the magnitude of the electromotive force,  $\phi_B$  is the magnetic flux of the system.

Traditional electromagnetic energy harvesting systems consist of a magnet and coil. The system is designed in such a way that if exposed to any external vibration, there is a relative motion between the magnet and coil. As a result, according to Eq. 1.2, the system experiences an electromotive force that drives a current through the circuit. Although these sorts of energy harvesters can achieve a high output power, due to the presence of the magnet, it's very difficult to integrate these systems in electronics and microsystems. Moreover, due to that same magnet, micro or nano level fabrication of these energy harvesters is also a challenge. As a result, electromagnetic energy harvesters are mainly suited for macro-level purposes [7], [41]. The schematic of a few electromagnetic energy harvesting systems are depicted in Fig. 1.4 [42], [43].

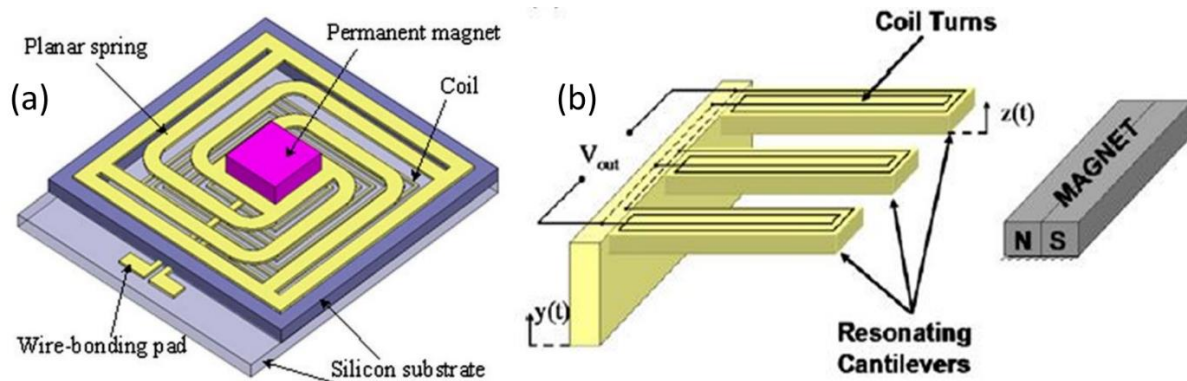


Figure 1.4: (a) Schematic of a typical electromagnetic energy harvesting system [42] (Reprinted with permission. Copyright © 2009, Springer-Verlag). (b) A cantilever based electromagnetic energy harvesting system [43] (Reprinted with permission. Copyright © 2008, Elsevier)

### 1.2.2. Electrostatic energy harvesters

Electrostatic energy harvesters rely on the change of air gap between two externally charged parallel plates which form a capacitor with variable capacitance. One of the plates is usually fixed and the other is suspended through springs. As a result, upon exposure to a vibration, the suspended plate changes its position with respect to the fixed plate, causing a charge flow through the circuit due to the electrostatic induction. The most basic advantage of the electrostatic energy harvesters is their compatibility with electronics, microsystems, and microfabrication. However, there are a few major drawbacks that limit the performance of these systems. Due to the requirement of the external charging on the plates, electrostatic harvesters are technically not self-powered. Moreover, the maximum achievable power density for electrostatic energy harvesters is usually small [7], [41]. As a result, electrostatic energy harvesters are rarely implemented in practical applications. An example of the electrostatic energy harvester is presented in Fig. 1.5 [44].

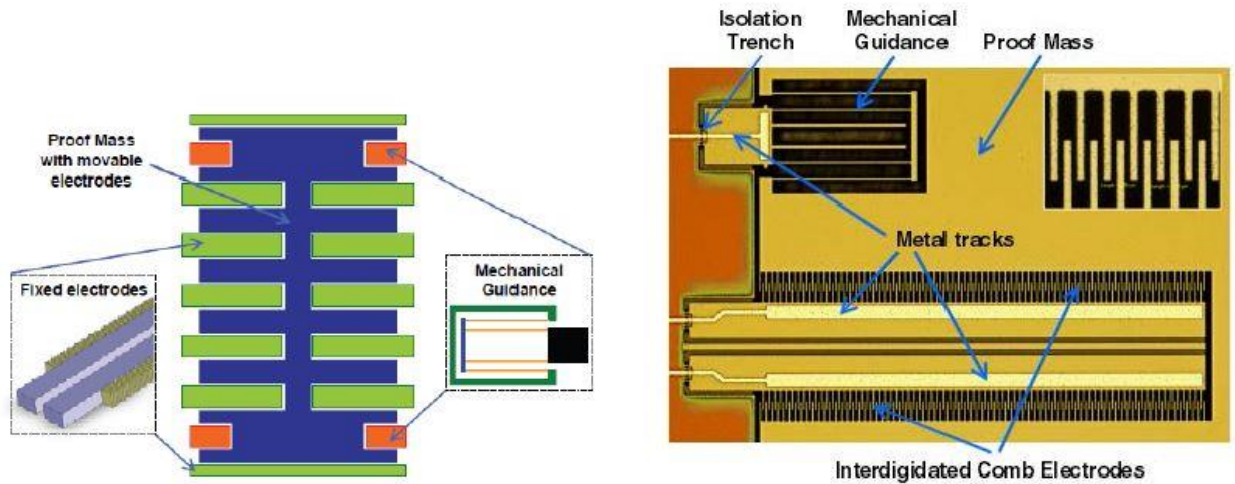


Figure 1.5: Design of an electrostatic energy harvester [44] (Reproduced with permission. Copyright © 2009, IOP Publishing)

### 1.2.3. Piezoelectric energy harvesters

Piezoelectric energy harvesters count on the inherent piezoelectric property of materials where charge separation occurs between two opposite sides of the material surfaces if an external stress is applied. Examples of piezoelectric materials include  $\text{PbZr}_x\text{Ti}_{1-x}\text{O}_3$  (PZT), Polyvinylidene Fluoride (PVDF),  $\text{BaTiO}_3$  (BTO), AlN, ZnO etc. From the material perspective, PEHs are diverse, especially because they can be implemented using different forms of nanostructures. Besides, the PEHs usually demonstrate a very high power density [7]. Furthermore, PEHs are compatible with electronics, microsystems, and nanofabrication. Drawbacks of PEHs include low output current and poor piezo thin-film coupling issues [41]. Fig. 1.6 demonstrates a sample PEH design [45].

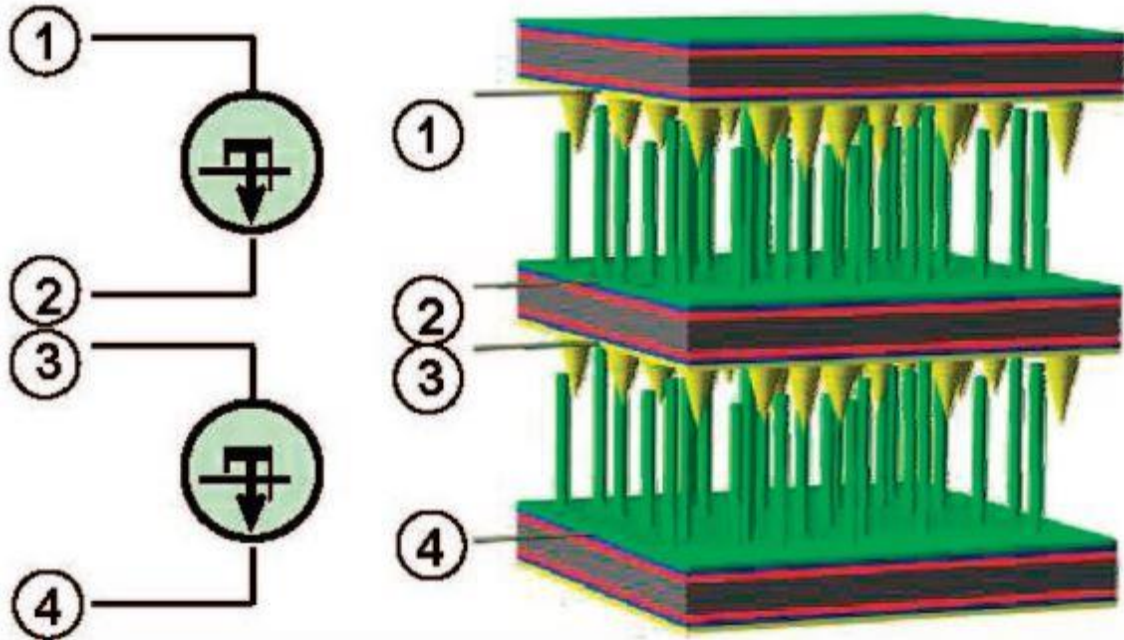


Figure 1.6: Design of a nanowire based piezoelectric energy harvester [45] (Reprinted with permission.

Copyright © 2008, American Chemical Society)

#### 1.2.4. Triboelectric energy harvesters

Triboelectric energy harvesters are based on contact electrification and electrostatic induction process originating from the triboelectric effect. If materials with dissimilar electron affinity get into frictional contact, triboelectric charges are generated on their surfaces. If the materials are separated from each other in the next cycle, the generated charges flow through the external load due to the electrostatic induction process which can be extracted as energy [46], [47], [3], [48], [49]. TEHs are the most recent and most effective type of VEH. They do not suffer from the common drawbacks of the traditional energy harvesters. TEHs are compatible with traditional electronics, microsystems, and nanofabrication techniques. Moreover, because of the superior structural robustness and larger generated power compared to the traditional energy harvesters, TEHs can be employed to harvest not only small-scale energy but also the energy in larger scales. The only major drawback is the requirement of a frictional contact between the triboelectric materials, which, in the long term, can lead to wear and tear problems. However, this drawback

can be mitigated to a minimal level if a careful structural design is implemented to ensure low overall stress on the device in its operating range.

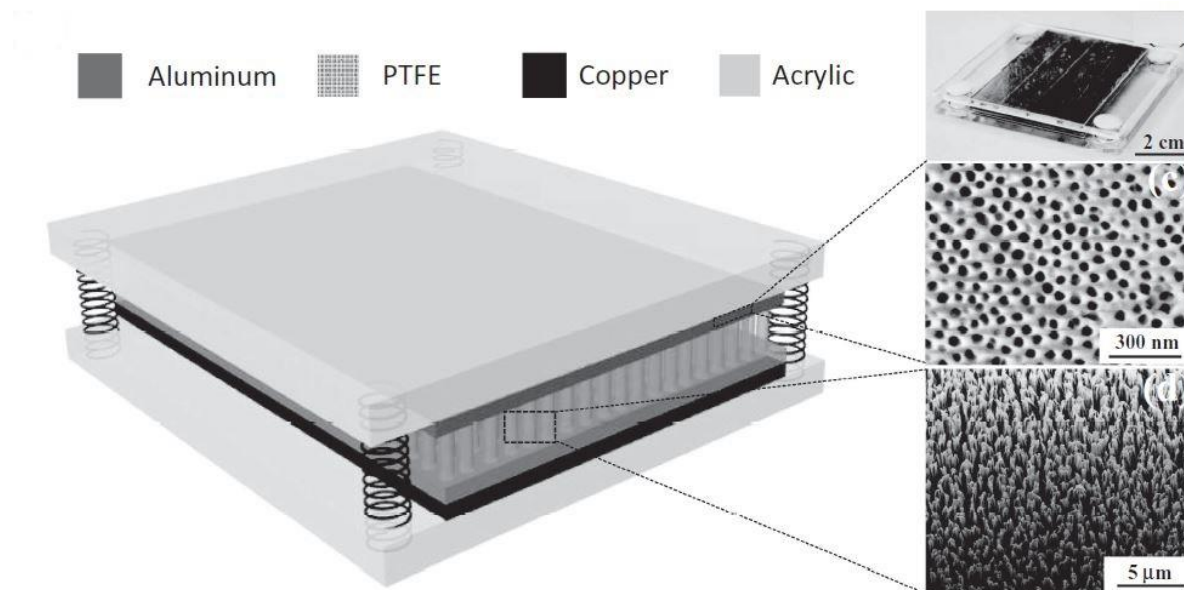


Figure 1.7: Design of a triboelectric energy harvester with Al and PTFE as the triboelectric materials pair [49] (Reprinted with permission. Copyright © 2013, American Chemical Society)

### 1.3. Review of ZnO nanowire based piezoelectric energy harvesters and nano-sensors

This section presents a brief literature review of ZnO as a piezoelectric material and ZnO based PEHs and nano-sensors. It also discusses the motivations and challenges associated with substitutional Li doping on the ZnO nanowires (NWs) which is the major target for a substantial part of this dissertation.

#### 1.3.1. Review of ZnO as a piezoelectric energy harvesting material

Zinc oxide is a II-VI semiconductive material that exhibits piezoelectric, semiconducting and pyroelectric properties. It can be synthesized in three basic crystal structures, the zinc-blende, the rock-salt, and the hexagonal Wurtzite. The zinc blende lattice structure is achieved only if it is grown on substrate material that has a cubic unit cell. On the other hand, Rock salt lattice structure is achieved only at high

pressure (about 10 GPa). Both of these ZnO structures are rare and need special conditioning to synthesize. In contrast, the hexagonal Wurtzite lattice structure of ZnO is thermodynamically stable at ambient conditions. In this structure, each anion is surrounded by four cations at the corners of a tetrahedron and vice versa (Fig. 1.8) [50]. The structure lacks an inversion symmetry, which is the origin of its piezoelectricity. There are two different lattice constants for this structure. The lattice constant along the horizontal axis is 3.296 Å. The lattice constant along the vertical axis is 5.2065 Å and denoted as ‘*c*’. Aside from the aforementioned properties, ZnO has a wide direct bandgap (3.3 eV) and high binding energy (60 meV), which makes it an interesting material for optical devices and sensors [51].

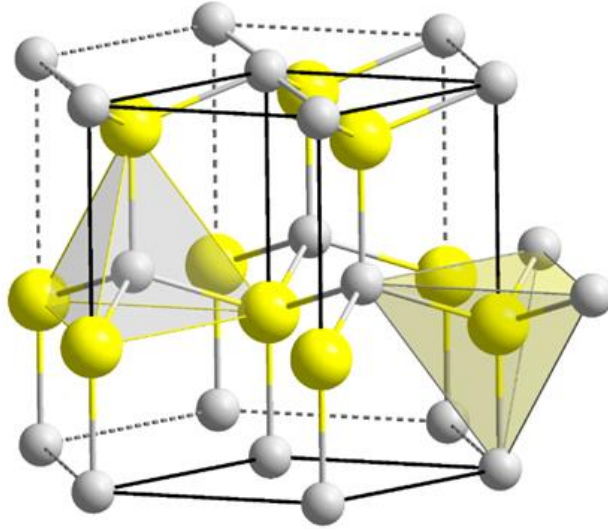


Figure 1.8: Hexagonal Wurtzite crystal structure of ZnO. White and yellow balls represent  $\text{Zn}^{2+}$  and  $\text{O}^{2-}$  ions, respectively [50]

The piezoelectric properties of ZnO are governed by the following expressions:

$$\sigma_p = c_{pq} \varepsilon_q - e_{kp} E_k \quad (1.3)$$

$$D_i = e_{iq} \varepsilon_q + \kappa_{ik} E_k \quad (1.4)$$

here,  $\sigma_p$  is mechanical stress matrix (Pa),  $c_{pq}$  is elastic constant matrix (GPa),  $\varepsilon_q$  is mechanical strain matrix,  $e_{kp}$  is piezoelectric coefficient matrix ( $C/m^2$ ),  $E_k$  is electric field (V/m),  $D_i$  is electric displacement ( $C/m^2$ ),  $\kappa_{ik}$  is dielectric constant matrix (F/m).  $\varepsilon_0$  is vacuum permittivity (F/m). For bulk or thin film ZnO, the values are found in the literature as follows [52]:

$$c_{pq} = \begin{pmatrix} c_{11} & c_{12} & c_{13} & 0 & 0 & 0 \\ c_{12} & c_{11} & c_{13} & 0 & 0 & 0 \\ c_{13} & c_{13} & c_{33} & 0 & 0 & 0 \\ 0 & 0 & 0 & c_{44} & 0 & 0 \\ 0 & 0 & 0 & 0 & c_{55} & 0 \\ 0 & 0 & 0 & 0 & 0 & \frac{c_{11}-c_{12}}{2} \end{pmatrix} = \begin{pmatrix} 207 & 117.7 & 106.1 & 0 & 0 & 0 \\ 117.7 & 207 & 106.1 & 0 & 0 & 0 \\ 106.1 & 106.1 & 209.5 & 0 & 0 & 0 \\ 0 & 0 & 0 & 44.8 & 0 & 0 \\ 0 & 0 & 0 & 0 & 44.6 & 0 \\ 0 & 0 & 0 & 0 & 0 & 44.65 \end{pmatrix} \quad (1.5)$$

$$e_{kp} = \begin{pmatrix} 0 & 0 & 0 & 0 & e_{15} & 0 \\ 0 & 0 & 0 & e_{15} & 0 & 0 \\ e_{31} & e_{31} & e_{33} & 0 & 0 & 0 \end{pmatrix} = \begin{pmatrix} 0 & 0 & 0 & 0 & -0.45 & 0 \\ 0 & 0 & 0 & -0.45 & 0 & 0 \\ -0.51 & -0.51 & 1.22 & 0 & 0 & 0 \end{pmatrix} \quad (1.6)$$

$$\kappa_{ik} = \begin{pmatrix} \kappa_{11} & 0 & 0 \\ 0 & \kappa_{22} & 0 \\ 0 & 0 & \kappa_{33} \end{pmatrix} = \begin{pmatrix} \kappa_{\perp} & 0 & 0 \\ 0 & \kappa_{\perp} & 0 \\ 0 & 0 & \kappa_{\parallel} \end{pmatrix} = \begin{pmatrix} \varepsilon_0 \times 7.77 & 0 & 0 \\ 0 & \varepsilon_0 \times 7.77 & 0 \\ 0 & 0 & \varepsilon_0 \times 8.91 \end{pmatrix} \quad (1.7)$$

For a NW, the piezoelectric effect is observed in two fundamental modes. The first is the piezo potential distribution along the NW cross section due to the bending ( $d_{31}$  mode). The other is the piezo potential distribution along the length of the NW due to the compression or stretching ( $d_{33}$  mode). Although the piezoelectric coefficient is higher for  $d_{33}$  mode, the elastic constant is also higher in this mode compared to the  $d_{31}$  mode. As a result, with the same input force, bending causes a larger deformation and strain in the NW structure compared to the compression. However, if the deformation or strain remains the same for both of these modes, compression generates more piezo potential compared to the bending due to the larger piezoelectric coefficient. This tradeoff between the deformability and piezo potential magnitude is a crucial design parameter for ZnO NW based devices.



ZnO belongs to an elite group of materials that demonstrates both piezoelectric and semiconducting properties. This makes it an exceptionally intriguing material for nano-sensors and nano-energy harvesters. Its piezoelectric properties are exploited to make self-powered devices that do not require any external bias to operate. Moreover, it exhibits a large variety of stable nanostructure configurations which are synthesized at low temperatures. For example, it can be synthesized as nanowire, nanorod, nanobelt, nanospring, nanoring, and many other nanostructure configurations as shown in Fig. 1.9 [53]. All of these nanostructures can be produced at almost 100% purity. In addition, they are synthesized at low temperatures (typically less than 100<sup>o</sup> C) which make them compatible with flexible electronics. These nanostructures are very much resistive to fatigue, thus, they are very stable and robust. On top of that, ZnO is biocompatible and environmentally friendly, making it an excellent material for bio-sensors and bio-devices [54].

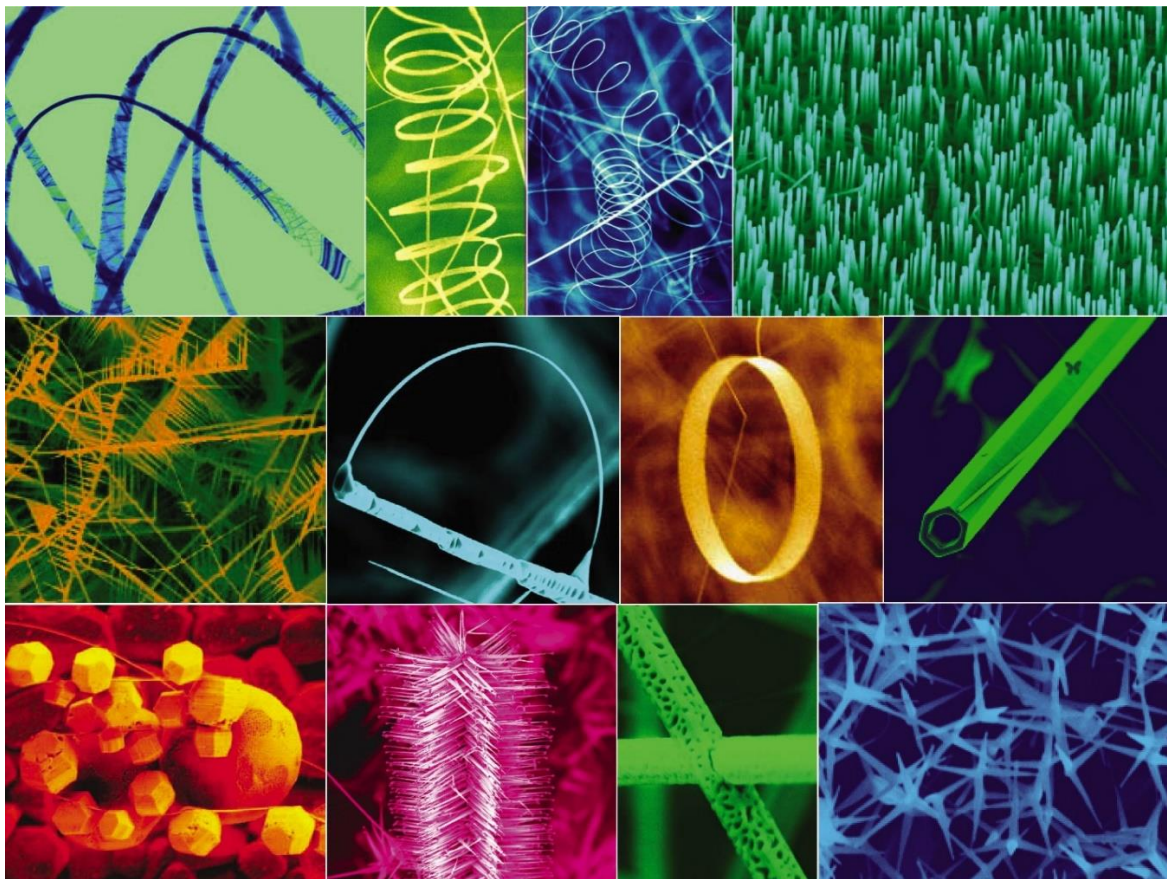


Figure 1.9: Nanostructure configurations of ZnO [53] (Reprinted with permission. Copyright © 2004,

Elsevier)

### 1.3.2. Vibrational energy harvesters based on ZnO nanowires

The first ZnO based piezoelectric VEH was demonstrated by Wang et al. [1]. They used hydrothermal growth technique to grow vertically oriented ZnO NWs. To characterize the NWs, an Atomic Force Microscopy (AFM) system was used to horizontally scan the NWs and apply force on them. This applied force strained the NWs and thus, a voltage was generated due to the piezoelectric effect. The characterization schematic for their work is presented in Fig. 1.10. Since then, numerous energy harvester designs have been published utilizing vertically oriented crystalline ZnO NWs as the fundamental element. Moreover, the most recent of these designs are based on flexible substrates which open up a completely new dimension of application fields for the energy harvesters [55], [56], [57].

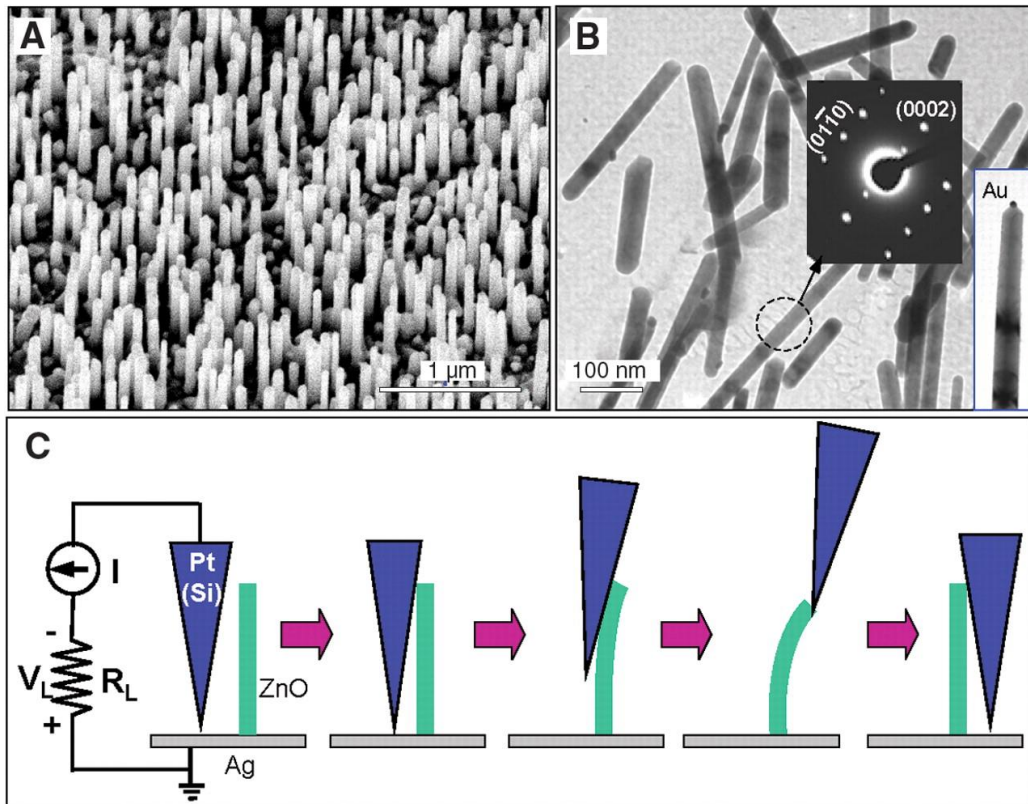


Figure 1.10: Energy harvester design by Wang et al. (a) – (b) Hydrothermally grown vertically aligned ZnO nanowires. (c) Characterization schematic. An AFM tip is operated in contact mode to horizontally scan and apply force on the nanowires [1] (Reprinted with permission. Copyright © 2006, The American

Association for the Advancement of Science)

Design of a NEMS (Nanoelectromechanical System) piezoelectric vibrational energy harvester based on ZnO NWs was previously published by our group (Fig. 1.11). The energy harvester is designed to operate at 1.1 kHz to match one of the vibration modes of an airplane fuselage. A bulk micro machined proof-mass of pyramidal shape is used to mechanically excite the NWs as shown in Fig. 1.11. Because of the pyramidal proof mass, when exposed to vibration, it bends the NWs which generate a piezoelectric output signal of a few hundreds of  $\mu\text{V}$  to a few mV [58].

Our group has also reported another PEH where the energy is harvested from the compression of the NWs as shown in Fig 1.12. In this design, the proof mass is coupled with the NWs through surface micromachining and UV-LIGA process. In addition, to improve the harvested power, several NW patches are connected in series. Characterization circuit parameters such as load resistance are optimized to maximize the harvested power. With 1.4 g maximum acceleration at 40 Hz vibrational frequency using a 7 M $\Omega$  optimal resistive load, the energy harvester can produce a peak power of 70 pW and a peak voltage of 21.4 mV. The normalized power density is 11.4 mWcm<sup>-3</sup>g<sup>-2</sup> for the fabricated device [59].

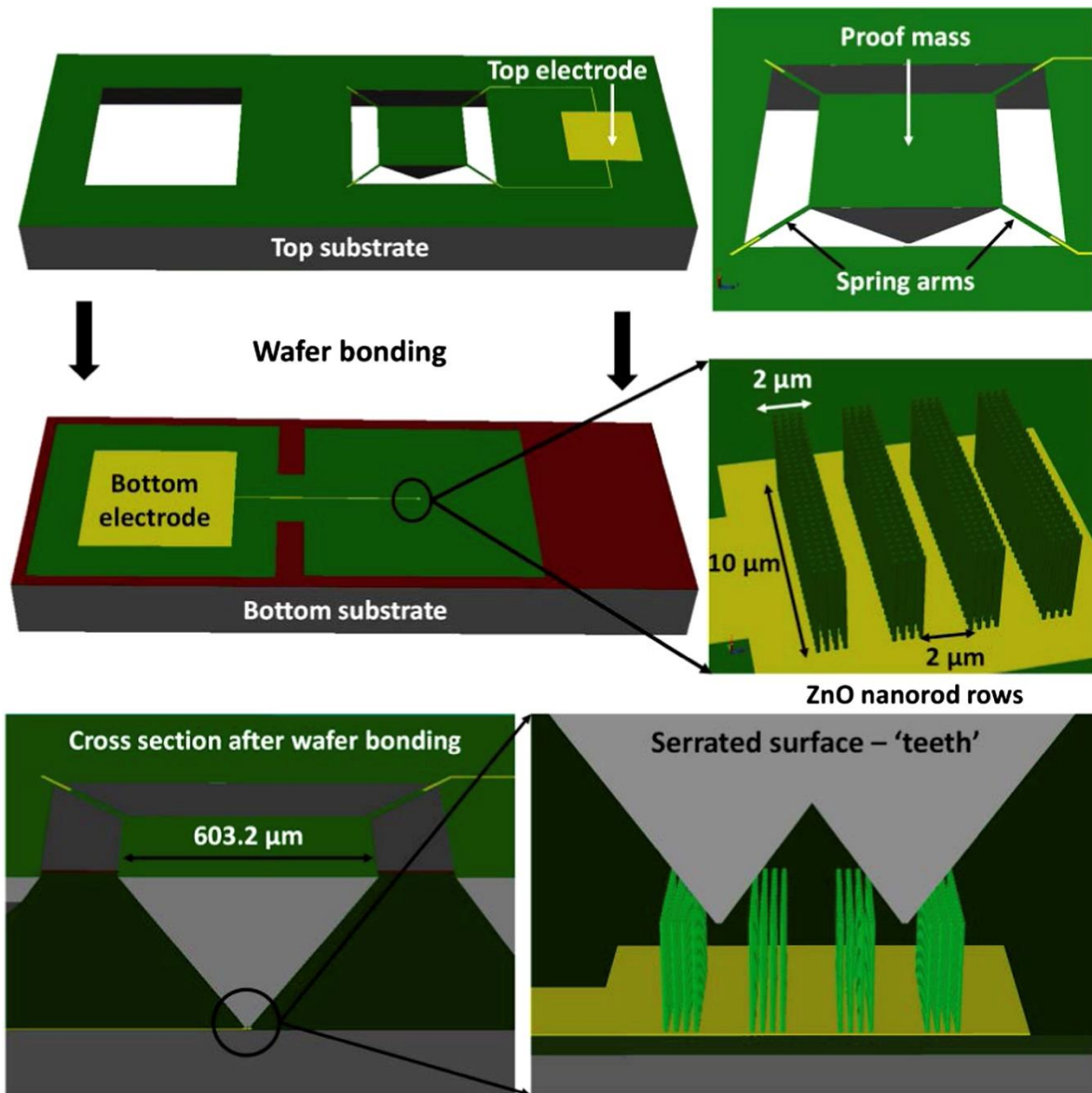


Figure 1.11: Design of a piezoelectric vibrational energy harvester with bulk micro machined pyramidal shaped proof-mass. Zoomed in and cross sectional view of the proof mass, spring and nanowire arrays are also displayed [58] (Reprinted with permission. Copyright © 2014, Elsevier)

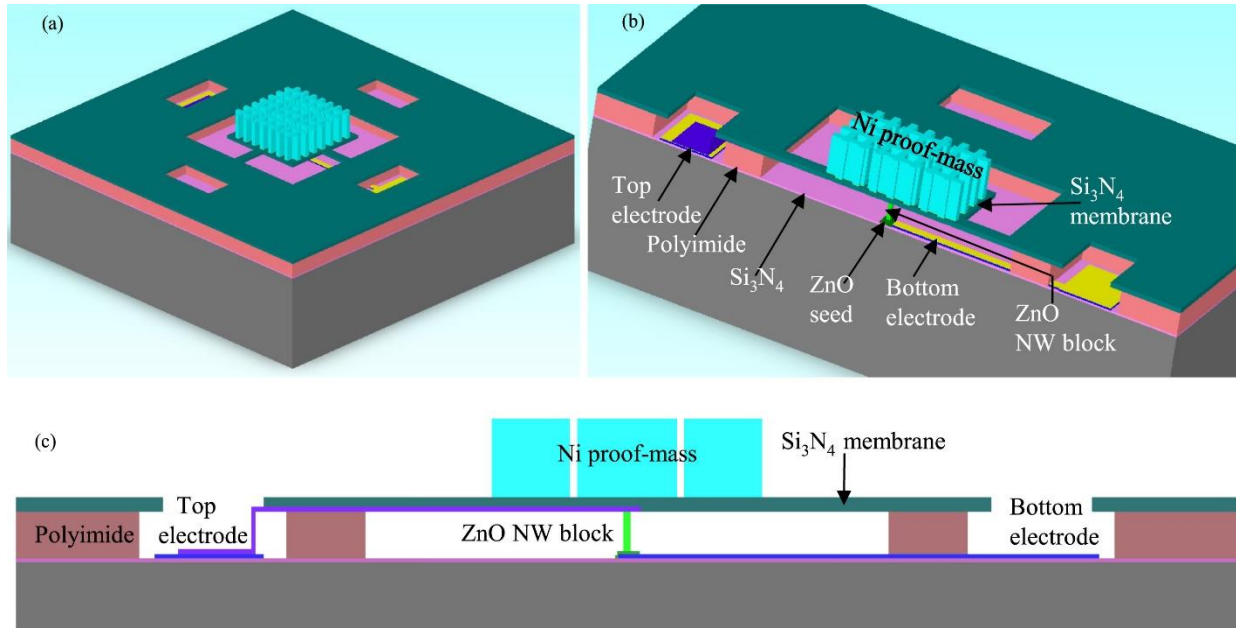


Figure 1.12: Design of a piezoelectric vibrational harvester where energy is generated from the compression of the ZnO nanowires. The proof-mass compresses the nanowires in vertical direction when subject to vibrations. Figures describe (a) overview (b) cross section and (c) schematic of the design [59]

(Reprinted with permission. Copyright © 2016, Elsevier)

### 1.3.3. Nano-sensors based on ZnO nanowires

Compelled by the piezoelectric properties, ZnO based nano-sensors are self-powered and do not require any biasing to operate. This fundamental advantage over traditional sensors improves their endurance and reliability as well as opens up new application scopes. Moreover, the electrical resistivity of ZnO is found to change significantly in the presence of specific chemicals and gases. This principle is utilized to make chemical and gas sensors from ZnO [57], [60], [61], [62], [63]. Furthermore, the high bandgap and binding energy of ZnO make it an attractive material for optical sensors and detectors [64]. On top of that, as ZnO is biocompatible, it is also a well-studied material for bio-sensors [65], [66], [51], [54].

A tactile/pressure nano-sensor using ZnO NWs has been reported by our group previously (Fig. 1.13). The sensor is flexible and can be integrated into robotic skin and garments [31]. Nanoimprint lithography is implemented in the fabrication process to create a template over a ZnO seed layer with an array of circular openings having 200 nm diameter and 500 nm pitch. This ensures the ordered growth of the ZnO NWs. The sensor is fabricated between a flexible substrate and a superstrate. A polyimide layer, encapsulating the NWs, acts as the sacrificial layer, which is plasma etched to expose the NW tips. This sensor can realize a spatial resolution of 1 mm or better. The sensor was characterized with an applied pressure ranging between 10 to 200 kPa. For reference, the light touch of a human finger exerts 5 kPa pressure whereas a fist punch can produce around 500 kPa [67]. Peak sensitivity of  $21.2 \mu\text{V}/\text{kPa}$  is obtained from the sensor. The sensor survived more than 500,000 taps with pressure less than 200 kPa without any fatigue, which underlines the robustness of the ZnO NWs.

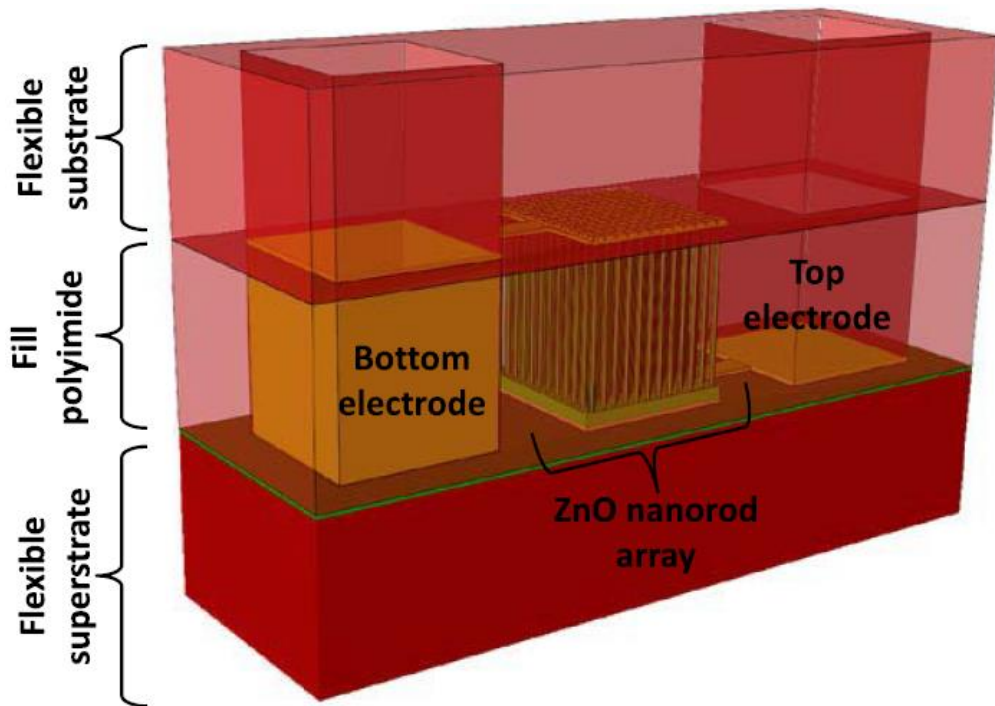


Figure 1.13: Design of a flexible tactile and pressure sensor. ZnO NWs are sandwiched between the flexible substrate and superstrate. The NWs generate output signal when subject to a pressure through the flexible substrate [31] (Reprinted with permission. Copyright © 2015, IEEE)

### 1.3.4. Motivations for Li doping into ZnO nanowires

In spite of several intriguing properties, ZnO is unable to realize its full potential due to its relatively high free electron concentration which screens part of the generated piezoelectric voltage [68], [69]. As a result of oxygen vacancies and zinc interstitials, intrinsic ZnO is n-type. Furthermore, the piezoelectric coefficient of ZnO is inherently low compared to some other well-known piezoelectric materials like PZT or BTO [70]. For these reasons, although ZnO provides a higher output current, the output voltage is still much less which results in a low overall power output [68]. To overcome these problems, different approaches have been reported. The influence of transition metal dopants including Cr, Cu, Ni, Co, and Fe on ZnO has been investigated [71], [72], [73]. However, since the transition metals have a comparable size and the same number of valence electrons as Zn, it is less likely that they will improve the piezoelectric properties of ZnO. A more recent study demonstrated that doping ZnO with Cl could significantly improve the piezoelectric performance by inducing an increased lattice strain along its c-axis [55]. In another study, it was reported that a p-type polymer layer on a film of ZnO nanostructures could greatly reduce the electron screening effect and shift the Fermi level which results in an enhanced power output [68]. The effect of Sb [56], S [74], Ga [75] and Ag [76] doping on ZnO NWs has been also reported. Few of the recent efforts have revealed that doping the ZnO nanostructures with Li is arguably be the most promising technique to enhance the performance of ZnO as an energy harvesting element [69], [70], [77], [78], [79].

Doping ZnO nanostructures with Li can potentially improve its performance for four reasons. First, Li acts as a shallow level acceptor in ZnO. Therefore, it can greatly reduce the piezoelectric potential screening effect from the intrinsically n-type ZnO [68], [70], [56], [78], [80], [81]. Next, due to the small radius of the Li ion ( $0.6 \text{ \AA}$ ), it creates an increased strain while replacing the Zn ion ( $0.74 \text{ \AA}$ ) in the ZnO lattice, thus increasing the piezoelectric coefficient [70], [72], [82], [83], [84]. Third, Li takes an off-centered lattice site, which adds to the already existing anisotropy of the ZnO structure, resulting in further enhanced piezoelectric coefficient [82], [85]. Finally, doping intrinsically n-type ZnO with p-type Li increases its electrical resistivity, leading to reduced charge leakage [86].

### **1.3.5. Challenges associated with Li doping into ZnO nanowires**

Although Li doping into ZnO crystal can potentially have an impressive impact on its piezoelectric effect, there are several challenges which need to be addressed first to effectively couple the Li atoms into the ZnO crystal. First, p-type doping on ZnO is still not well-studied and not much is known about the reproducibility and stability [55], [79]. Next, Li is a light and small element, making it hard to quantize. It cannot be detected through common characterization techniques such as Energy Dispersive Spectroscopy (EDS) [87]. Finally and most importantly, Li incorporates into the ZnO crystal structure in two ways. It can substitute Zn ion (denoted by  $Li_{Zn}$ ) or occupy an interstitial position due to its small size (denoted by  $Li_i$ ) into the ZnO structure. The  $Li_{Zn}$  acts as an electron acceptor in the Zn sites, which is desirable to achieve p-type doping. However, the  $Li_i$  acts as an undesired electron donor for ZnO. As a result,  $Li_i$  compensates a substantial portion of  $Li_{Zn}$  acceptors, which is a major obstacle in achieving p-type doping in ZnO nanostructures [82], [88].

## **1.4. Review of triboelectric energy harvesters**

This section presents a brief literature review of TEHs, their operating principles, and applications. It also discusses the motivations and challenges associated with a microelectromechanical systems (MEMS) scale energy harvester with high operating frequency and wide bandwidth which is another major target for a substantial part of this dissertation.

### **1.4.1. Overview of the triboelectric effect**

#### **1.4.1.1. Origin of the triboelectric effect**

The foundation of the triboelectric energy harvesters is based on the triboelectric effect where contact electrification and charge generation take place if materials with dissimilar electron affinities come into frictional contact. The word ‘tribo’ comes from a Greek root which means rubbing or friction. The



exact origin of the triboelectric effect is still not well established. It is suspected that when two different molecules come close to each other and make friction, there is a formation of an electrochemical bond between them. If they are then moved apart, the net charge is not neutral and a static charge is obtained with one of the materials having a net positive charge and the other one getting an equal amount of net negative charge [89]. In short, if two materials with opposite electron affinities are rubbed with each other, due to the triboelectric effect, static charges are stored on them.

The triboelectric effect is a very common phenomenon in regular human life (Fig. 1.14 [90], [91]). For instance, a comb starts attracting paper pieces just after a hairbrush. This is the result of the stored triboelectric charge on the comb which was generated due to the friction between the comb and hair. Another illustration of the triboelectric effect is the static shock in winter when people touch metals, for example, the car door. The friction between human skin and the polyester clothing they wear in winter leads to the generation of triboelectric static charge on human skin. As a result, whenever they touch any metal, the static charges get a path for discharging and they feel an electric shock.

Traditionally, the triboelectric effect has been known as an undesirable phenomenon as it can lead to electrostatic charge buildup, electrostatic discharge, and spark creation. This can damage electronic circuits, create communication disruptions from aircraft, as well as lead to hazardous situations like wildfires [92], [93] (Fig. 1.15 [94], [95], [96]). Nevertheless, this same effect is now being utilized in triboelectric energy harvesting from various vibration sources.

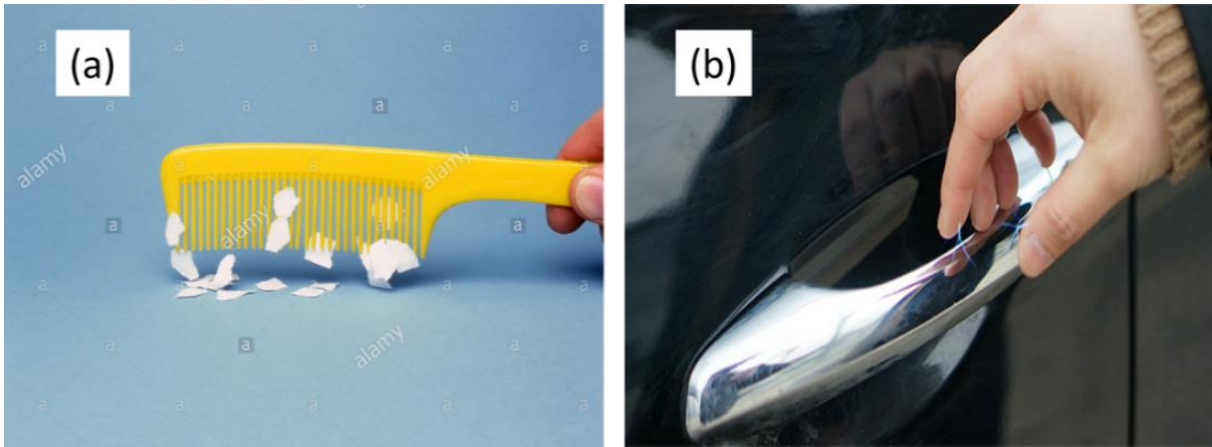


Figure 1.14: Examples of the triboelectric effect in regular life. (a) Comb attracting paper pieces just after a hair brush [90]. (b) Electric shock while grabbing a car door due to the static charge on human skin [91].



Figure 1.15: Undesirable impacts of the triboelectric effect. (a) Wildfire from triboelectric spark [94]. (b) Damage in IC from electrostatic discharge [95]. (c) Communication disturbance from aircraft because of the triboelectric charge accumulation on their body [96].

#### 1.4.1.2. Selection of the triboelectric pair of materials

As mentioned earlier, the triboelectric effect leads to the generation of triboelectric charge when two different materials come into frictional contact with each other. The magnitude of this generated charge depends on the relative electron affinity between the pair of materials involved in the frictional contact. This effect is more clearly visualized from the triboelectric series [97] as depicted in Fig. 1.16 [98]. The materials on the upper half of the table have positive electron affinity whereas the materials on the lower half have negative electron affinity. To achieve a high triboelectric charge density, the pair of materials should be chosen in such a way that the gap between their relative positions in the triboelectric series is

large. For this thesis, the Al – Teflon pair is selected as the triboelectric materials pair based on the high gap between them in the triboelectric series and their fabrication compatibility with MEMS processes.



Figure 1.16: Triboelectric series representing the relative electron affinity between materials [98].

## 1.4.2. Operating modes of triboelectric energy harvesters

Based on the fundamental principle of the charge generation and extraction, TEHs are classified in four basic modes [99], [3], [100]. They are the vertical contact separation mode [101], [102], [103], [104], the in-plane sliding mode [105], [106], [107], [108], the single electrode mode [109], and finally, the freestanding triboelectric layer mode [13], [110]. This section presents a brief overview on these operating modes.

### 1.4.2.1. Vertical contact separation mode

The vertical contact separation mode is the most simple and basic mode of operation for the TEHs. In this mode, the triboelectric materials are separated by a gap in the vertical direction. Electrodes are deposited on the top and the bottom surface of the stacked structure. If the triboelectric materials physically

contact each other, opposite triboelectric charge is generated on them. Afterward, when the triboelectric materials are separated from each other by external excitation, a voltage appears across them. As a result, when the electrodes are connected through external circuitry, the system experiences a charge flow through the load. If the contact and separation cycles keep repeating, a continuous AC power is observed at the load. The vertical contact separation mode is the most popular mode of operation for the TEHs because of its simple and robust structure and better charge pumping efficiency [99], [111]. The schematic for the vertical contact separation mode is depicted in Fig. 1.17(a).

#### **1.4.2.2. In-plane sliding mode**

For the in-plane sliding mode of the TEHs, the relative motion between the triboelectric layers is parallel to their surface. Similar to the vertical contact separation mode, electrodes are deposited on the top and the bottom surface of the stacked structure. However, contrary to the vertical contact separation mode, parts of the triboelectric layers always remain in contact with each other having no gap between them. When exposed to external vibration, the sliding contact between the triboelectric layers creates the triboelectric charges. If the electrodes are connected through external circuitry, these triboelectric charges flow through the load. The surface charge density for the in-plane sliding mode is usually higher and easily reaches saturation because of the better contact between the triboelectric layers compared to the vertical contact separation mode. However, this also leads to more wear and tear problems which reduce the endurance of the device. The schematic for the in-plane sliding mode is depicted in Fig. 1.17(b).

#### **1.4.2.3. Single electrode mode**

The single electrode mode is an application specific variation of the vertical contact separation mode [112] and the in-plane sliding mode [113]. In few applications, connecting both the triboelectric layers through an external circuit becomes a challenge due to the mobile nature of one of the triboelectric plates. The single electrode mode is introduced for those applications where the electrode is deposited only on the

bottom triboelectric layer. No electrical connection is present on the top triboelectric layer. The bottom electrode, in this case, is connected to the ground through a load. As a result, the contact and separation between the triboelectric layers change the local electric field distribution, resulting in a charge flow between the ground and the bottom electrode. Although useful for some applications like energy harvesting from walking on the floor, this mode suffers from electrostatic screening effect which reduces the performance of the TEHs. The schematic for the single electrode mode is presented in Fig. 1.17(c).

#### **1.4.2.4. Freestanding triboelectric layer mode**

In the freestanding triboelectric layer mode operation, the triboelectric layers do not necessarily need to make a contact with each other. The structure consists of a pair of symmetric electrodes beneath a triboelectric layer. The size of the electrodes and the gap between them are usually made of the same order as the size of the moving triboelectric layer. The triboelectric layer is naturally charged up to its charge saturation point due to the friction with air and retains that charge density for hours without a significant loss. As a result of the triboelectric layer movement, an asymmetric charge distribution occurs between the electrodes. If the electrodes are connected through an external load, a periodic movement in the triboelectric layer creates a periodic charge flow through the load. Due to the absence of any friction, this design mode yields more reliable and durable devices. The schematic for the freestanding triboelectric layer mode is depicted in Fig. 1.17(d).

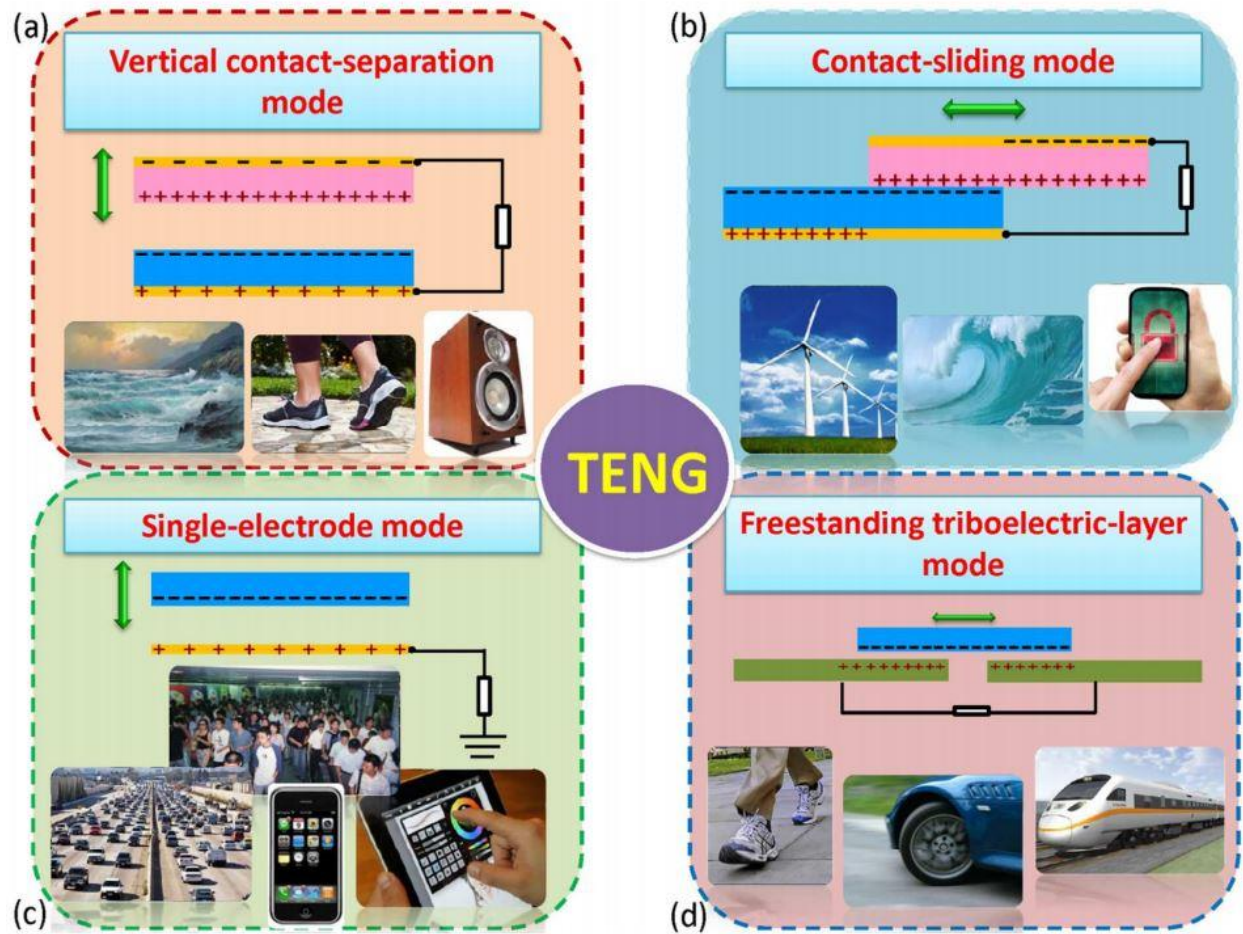


Figure 1.17: Schematic and applications of the four basic operational modes of the triboelectric energy harvesters. (a) Vertical contact separation mode. (b) In-plane sliding mode. (c) Single electrode mode. (d) Freestanding triboelectric layer mode [3] (Reprinted with permission. Copyright © 2014, Royal Society of Chemistry)

### 1.4.3. Motivations for a high operating frequency, wide bandwidth MEMS scale triboelectric energy harvester

Traditional research on TEHs has always focused energy harvesting from low frequency vibration sources (frequency typically less than 100 Hz) as they are more abundant in the ambient conditions [114], [103], [104], [35], [36]. As a result, several high frequency sources like automobile engines and aircraft

bodies are never explored properly as a possible source for triboelectric energy harvesting [8], [115], [116]. Considering this, a novel design of a TEH with a high target operating frequency can open up new potential applications fields. The target frequency for the TEH presented in this dissertation is 800 Hz, which is the primary vibration mode frequency of aircraft skin.

A high target operating frequency is also attractive from the device scaling point of view. For a typical TEH, if the spring constant  $k$  is kept constant, a high target operating frequency  $f$  reduces the mass of the proof-mass  $m$  required to achieve a certain operating condition as  $f = 1/2\pi\sqrt{k/m}$ . As the traditional designs always target low frequency vibration sources, the device dimensions have often ranged in the cm  $\times$  cm scale [114], [104], [9], [117]. A high target operating frequency is, therefore, also beneficial for scaling down the TEH to MEMS scale which is essential for certain applications including automobile and aircraft industry, micro-robotics, prosthetic systems, space exploration programs and sensor nodes in the internet of things (IoT) where device dimensions, as well as mass, are critical design considerations [118].

Triboelectric energy harvesters inherently rely on the contact between a fixed triboelectric plate and a movable triboelectric plate, separated by a gap. This resembles a typical mass spring damper system with a mechanical stopper. The presence of such a stopper is reported to widen the effective bandwidth of the system, especially, if operated at higher frequencies [119], [120]. Therefore, a high frequency MEMS TEH also carries the prospect of having a wide operating bandwidth.

#### **1.4.4. Challenges associated with high operating frequency, wide bandwidth MEMS scale triboelectric energy harvester**

Scaling down a TEH to MEMS scale, however, introduces new fabrication and operational challenges. For instance, lower mass and high squeeze film damping lead to a low contact force between the triboelectric layers [121], [122], [123]. This significantly reduces the triboelectric charge density,

resulting in lower output power from the system [124]. Moreover, to create a wide air gap between the two triboelectric layers, a thick sacrificial layer is required. At the final fabrication step, highly selective etching of this thick sacrificial layer becomes a challenge due to the presence of a polymeric triboelectric layer like Teflon [113], [125] or Polydimethylsiloxane PDMS [126], [114].

## **1.5. Organization of this dissertation**

This dissertation consists of four chapters.

*Chapter 1* presents an overall review of the VEHS with their structure, operating principles, classification, and applications. It also briefly describes the basics, motivations, and challenges associated with the two projects of this dissertation, one on Li-doped ZnO based PEH and the other one on high frequency, wide bandwidth MEMS scale triboelectric energy harvester.

*Chapter 2* illustrates in detail the fabrication, characterization, performance simulation and discussions on the Li-doped ZnO NW based PEH project. Performance comparison of the fabricated Li-doped ZnO NWs with state of the art literature designs is also presented.

*Chapter 3* elucidates the design, optimization, fabrication, and characterization of high frequency, wide bandwidth MEMS scale TEH with detailed comparison to other vibrational energy harvesters.

*Chapter 4* finally rounds up the conclusion of the dissertation with discussions on the performance and applications of the two projects of this Ph.D. thesis.



# Chapter 2 : Piezoelectric Energy Harvester Based on Li-doped ZnO

## Nanowires

### 2.1. Introduction

This chapter elaborates the synthesis and performance analysis of vertically-aligned Li-doped ZnO NWs as a piezoelectric energy harvesting element. Li-doped ZnO NWs with different concentrations of Li doping are synthesized using the hydrothermal growth process. Effects of Li doping on ZnO NW performance have been previously reported [70], [77], [79], [86]. However, the effect of NW shape variation with doping was not accounted for in any of those works. Sohn et al. [69] grew Li-doped ZnO NWs of the same size, but did not elaborate on the impact of Li doping on the NW size, resulting in a performance modification. Here, we have decoupled the individual effects of Li doping on the NW size and on the piezoelectric coefficient which elucidates how much each effect plays a role in the sensitivity. In addition, a discussion is provided on the role of Li diffusion mechanism within the ZnO NW structure and its impact on the piezoelectric sensitivity.

To investigate the effect of doping, a scanning electron microscope (SEM) is used to characterize the physical and structural properties of the NWs. The incorporation of the Li dopants into the ZnO structure is studied using X-Ray Diffraction (XRD), Raman spectroscopy and X-ray Photoluminescence Spectroscopy (XPS), and Energy Dispersive Spectroscopy (EDS). The piezoelectric performance improvement due to the incorporation of the Li dopants is characterized using an Atomic Force Microscopy (AFM) system. This work gives an insight into the role of Li doping on the vertically grown ZnO NWs and quantitative assessment of such doping on piezoelectric ZnO NW nano-energy harvesters and nano-sensors.

Outcomes of this chapter have been reported in the 2017 IEEE Sensors Conference [30], [127] and Nano Energy Journal [128].

## 2.2. Fabrication of the Li-doped ZnO nanowire carpet

### 2.2.1. Fabrication process flow

The complete schematic of the fabrication process flow is presented in Fig. 2.1. The fabrication process started with the sputter deposition of a 400 nm  $\text{Si}_3\text{N}_4$  as an insulation layer over a 3" Si wafer (Fig. 2.1(a)). A 30 nm of Cr and another 100 nm of Au layer were thermally evaporated and then patterned using a standard lift-off process with NR9-1500PY photoresist as shown in Fig. 2.1(b) and Fig. 2.1(c), respectively. The Au layer works as the bottom electrode of the device while the Cr is used as the adhesion layer between the insulation layer and the bottom electrode. Subsequently, a 30 nm Ti layer was thermally evaporated, followed by the deposition of 300 nm ZnO at 400<sup>0</sup> C using pulsed laser deposition (PLD) (Fig. 2.1(d)). The PLD-deposited ZnO layer works as a seed layer for the ZnO NW growth process, while the Ti layer is deposited to create an Ohmic contact between the bottom electrode and the seed layer. The ZnO seed and the Ti layers were then patterned using a wet etch process in HF (Fig. 2.1(e)).

After the bottom electrode and the seed layer formation, the wafer was coated and patterned with SU-8 photoresist. The SU-8 layer creates defined opening areas on the seed layer for ZnO NW growth. The opening areas on SU-8, as shown in Fig. 2.1(f) are slightly smaller than the seed layer patterning to restrict any lateral NW growth. The wafer was then diced into several pieces to introduce process variations. Consequently, the hydrothermal growth process was conducted at a constant temperature of 90<sup>0</sup> C for 3 hours to grow the Li-doped ZnO NWs on top of the ZnO seed layer. After the growth process, the remaining SU-8 was removed to expose the grown NWs (Fig. 2.1(g)).

Each NW patch has an area of 8×8  $\mu\text{m}^2$ . The fabricated NW patches are studied using SEM to observe their morphology. Fig. 2.2 depicts 5 NW patches with the bottom electrode. Each device wafer contained at least 90 of such patches.

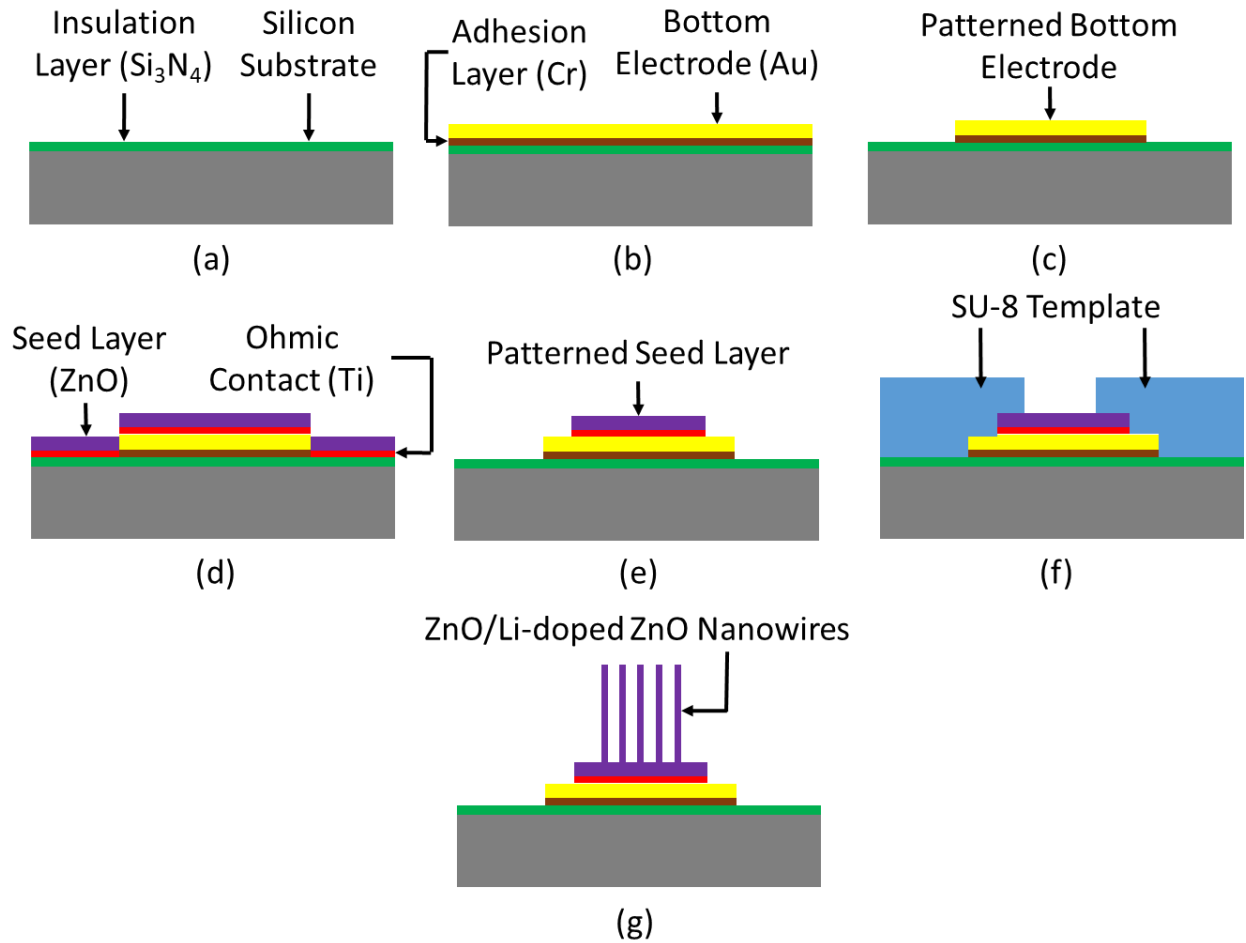


Figure 2.1: Fabrication process flow for the Li-doped ZnO nanowire device. (a) Deposition of the  $\text{Si}_3\text{N}_4$  insulation/passivation layer over a Si wafer. (b) Deposition of 30 nm Cr adhesion and 100 nm Au layers as the bottom electrode. (c) Patterning of the bottom electrode. (d) Deposition of 30 nm Ti Ohmic contact layer and 300 nm ZnO seed layer. (e) Patterning of the Ti/ZnO seed layer. (f) Formation of SU-8 template layer (g) Hydrothermal growth of the undoped or Li-doped ZnO NWs and removal of the SU-8 layer.

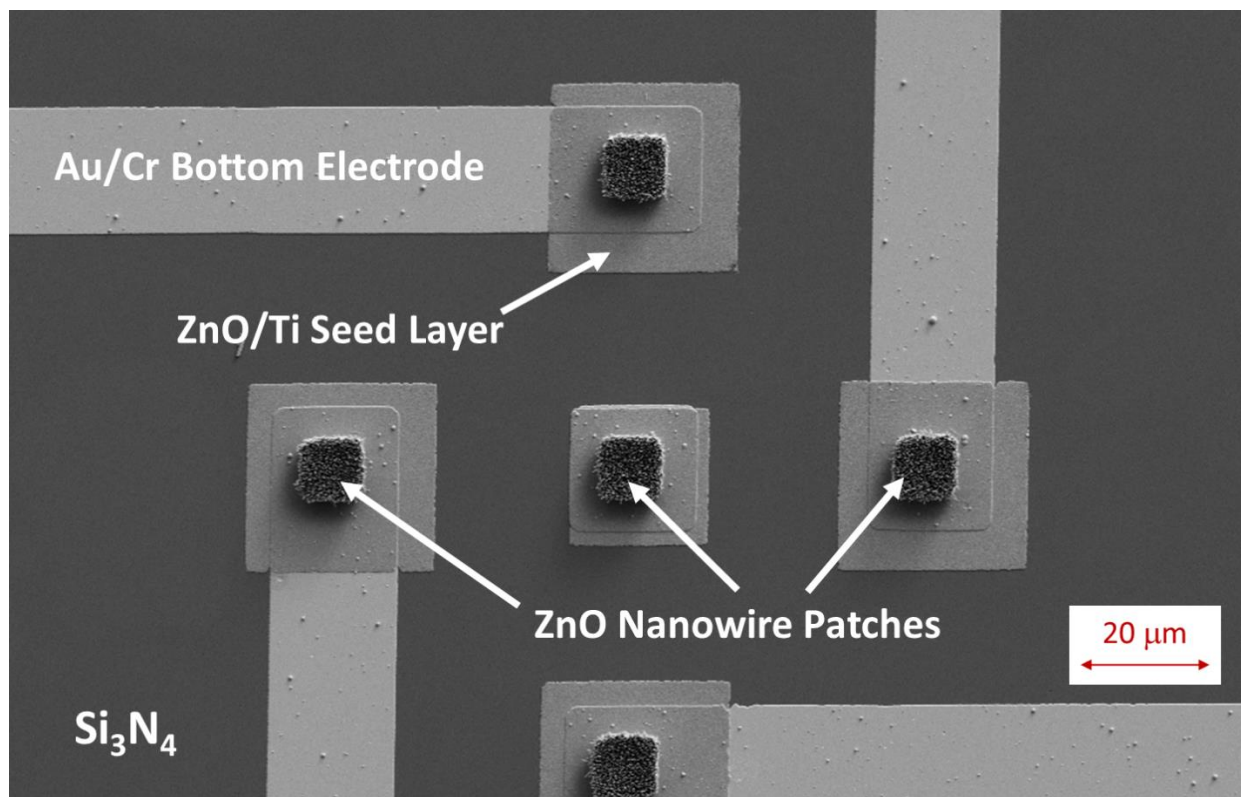


Figure 2.2: SEM image of five NW patches taken after the fabrication of the device. The NW patches are  $8 \times 8 \mu\text{m}^2$  in size. Each of the fabricated devices contains at least 90 of such NW patches.

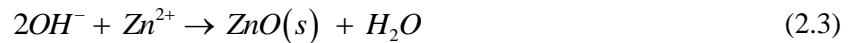
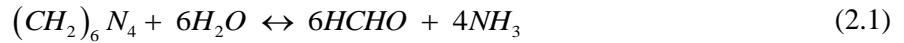
### 2.2.2. Hydrothermal growth process

Li-doped ZnO NWs were synthesized using the hydrothermal growth process. The nutrient solution for this growth process consisted of zinc acetate and hexamethylenetetramine (HMTA). Zinc acetate was chosen as the zinc medium because it has been reported to yield ZnO nanostructures with higher aspect ratios than those by zinc nitrate or zinc chloride [129].

To synthesize the undoped ZnO NW sample, 10 mM of zinc acetate ( $\text{Zn}(\text{CH}_3\text{COO})_2$ ) and 10 mM of HMTA were prepared in 900 mL of DI water. A piece from the diced samples was then placed upside down into the growth solution and the hydrothermal growth process was conducted at a constant temperature of  $90^\circ\text{C}$  for 3 hours. In a similar process, four Li-doped ZnO NW samples with different concentrations of Li were prepared. To do this, lithium acetate ( $\text{LiCH}_3\text{COO}$ ) of different concentrations

were also added in the hydrothermal growth solution in addition to the zinc acetate and HMTA. All the chemicals used in the hydrothermal growth solution were brought from Sigma Aldrich.

The complete hydrothermal growth experimental setup is shown in Fig. 2.3. The nutrient/growth solution was put in a white Teflon beaker. The Teflon beaker was then put inside another glass beaker over a Teflon stage. Silicone oil was poured in that glass beaker to form an oil bath for the growth solution. The glass beaker was then put over a hotplate equipped with a feedback control probe and magnetic stirring system. The temperature and stirring speed of the hotplate was set to 115<sup>0</sup> C and 250 RPM, respectively. This ensures uniform heating of the hydrothermal growth solution through the oil bath. Two different external thermometers were used to monitor the temperature of the oil bath and the growth solution. After around 2 hours of heating, the growth solution temperature stabilized at 90<sup>0</sup> C. Next, a piece from the diced sample was mounted on a wafer holder cover using tape and placed upside down into the growth solution. The Teflon jar was then sealed and the hydrothermal growth process was conducted for 3 hours. The following chemical reactions occur during the hydrothermal process while we grow the undoped ZnO NWs [130]:



The Li dopant concentrations in the hydrothermal growth solution for all of the five devices are listed in Table 1. The devices are named according to the concentration of the ingredients present in the hydrothermal growth solution. For example, the device ZnO-10-10-25 refers to the device that has 10 mM zinc acetate, 10 mM HMTA and 25 mM lithium acetate in the hydrothermal growth solution.

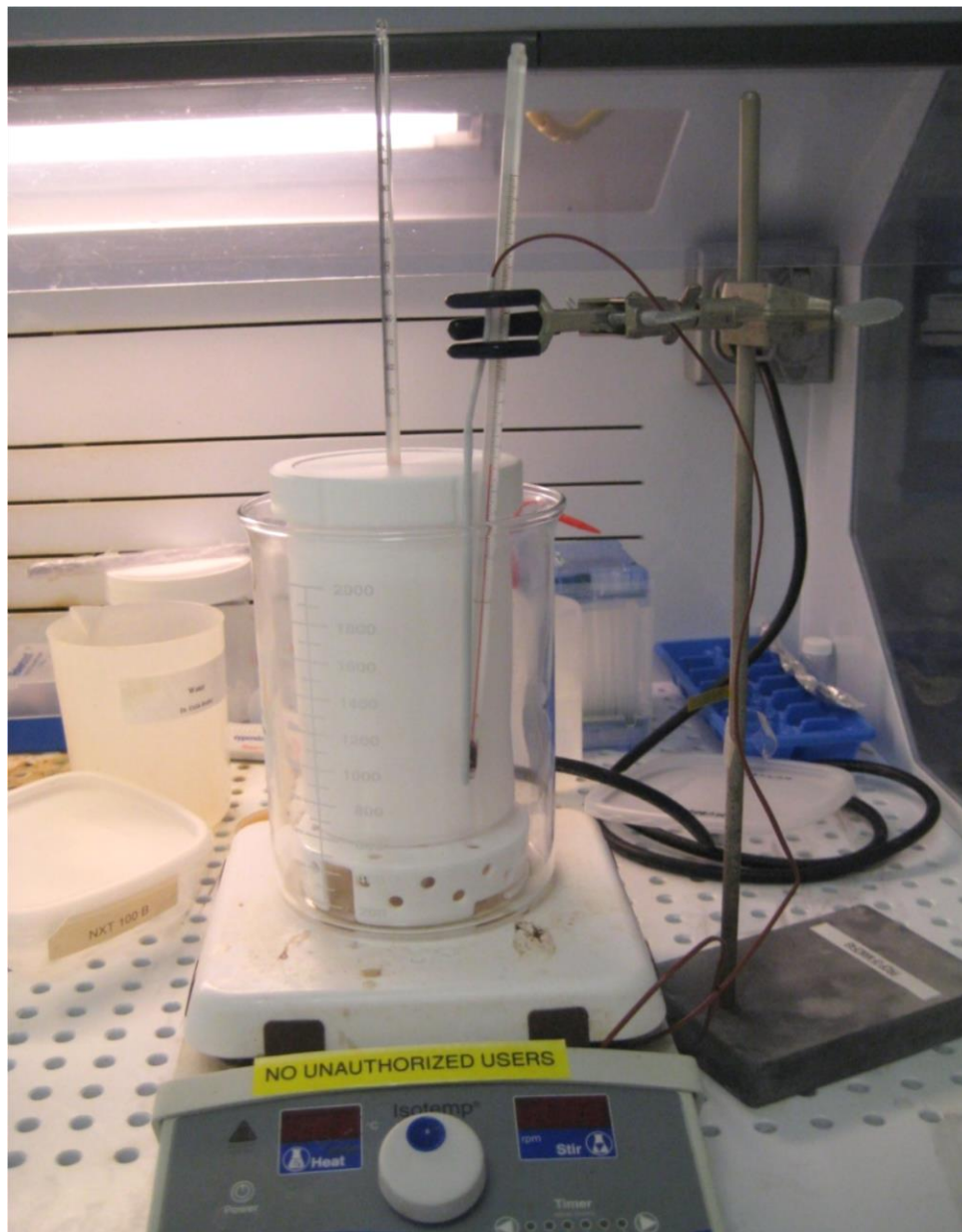


Figure 2.3: Experimental setup for the hydrothermal growth process

Table 2.1: Concentrations of the chemical ingredients in hydrothermal growth solution. Molar weights of  $\text{Zn}(\text{CH}_3\text{COO})_2$ , HMTA and  $\text{LiCH}_3\text{COO}$  are 219.51, 140.19 and 102.02 g/mol, respectively.

Sample	Solution Volume (mL)	$\text{Zn}(\text{CH}_3\text{COO})_2$		HMTA		$\text{LiCH}_3\text{COO}$	
		Conc. (mM)	Amount (g)	Conc. (mM)	Amount (g)	Conc. (mM)	Amount (g)
ZnO-10-10-0	900	10	1.98	10	1.26	0	0
ZnO-10-10-7						7	0.64
ZnO-10-10-10						10	0.92
ZnO-10-10-15						15	1.38
ZnO-10-10-25						25	2.3

### 2.3. Characterization of the nanowires

The fabricated devices were studied for physical and structural property variations using a Field Emission SEM (FE-SEM) system. Figure 2.4 shows 45<sup>o</sup>-tilted pictures of the NW patches from the five different NW devices. Similarly, Fig. 2.5 demonstrates the same devices without tilting the SEM stage. These figures were analyzed to calculate the average length, diameter and density of the NWs in each of the devices using the ImageJ™ software.

#### 2.3.1. Physical property characterization

##### 2.3.1.1. Length variation characterization

SEM images are analyzed to determine the average length of the NWs in each of the fabricated devices. The magnification was kept constant to better compare the length variation among the samples due to the incorporation of Li dopants. Figure 2.4 shows the as recorded SEM images for all of the devices. The calculated average length of the NWs is plotted in Fig. 2.6(a). It is evident from the SEM photos that the introduction of Li doping stunts the NW growth. The explanation for this lies in the reactions that occur during the hydrothermal growth process.

When the Li doping reagent is introduced into the growth solution, a partial replacement of  $Zn^{2+}$  ions by  $Li^+$  ions takes place. This substitution results in a decrease in the effective positive charge on the (0002) surface [131]. Therefore, the NW forming reaction (Eqn. 2.3) slows down, which in turn, decreases the growth of ZnO NWs perpendicular to the (0002) polar surface.

Another interesting observation is that, the NWs toward the middle of each NW patch seem to be shorter than the NWs along the edge. This effect is associated with the depletion of the growth solution towards the middle of the patch during the 3-hour long growth process. Although in the beginning, the growth rate of NWs all over the patch remains the same, as the height of NWs grow long, the availability of growth solution gets lower towards the middle of the patch. As a result, the NWs toward the edges of the patch grow higher than the one toward the middle. In addition, the NW growth rate is slower in the highly-doped devices. Consequently, the height difference is more evident in the low-doped devices than highly-doped devices.

### **2.3.1.2. Diameter and density variation characterization**

The close-up SEM images shown in Fig. 2.5 were analyzed to quantify the density and the cross-sectional size variation within each device and between devices with different Li doping levels. The average diameter of the NWs in each of the devices is plotted in Fig. 2.6(a). Although NWs grow in the shape of a hexagonal prism, for simplicity, a cylindrical shape is assumed. The average diameter of the devices varies from 111 nm to 142 nm with no clear pattern and a high standard deviation. This is because the diameter of the NWs primarily depends on the grain size and the thickness of the seed layer and not on the doping concentration. Pradel et al. [132] obtained a similar result when they doped the ZnO NWs with Sb.

The density (number of NWs per  $\mu m^2$ ) of the NWs is found to increase with the doping concentration as shown in Fig. 2.6(b). This can be associated with the fact that Li, as a metal, might act as a catalyst for the hydrothermal growth of ZnO. Several metals are proven catalysts for ZnO NW growth



such as Al [133], Ag [134], [135], Au [136], Ni and Fe [137]. It is also well reported that the concentration of these catalysts can be exploited to control the density of the NWs [133], [135], [138], [137]. Therefore, we suspect that Li also acts as a metal catalyst in the growth process, providing more nucleation sites for growth. This in turn, increases the density of NWs. The growth rate along the (0002) face, however, still reduces because of the slower reaction rate as discussed earlier in this section.

To obtain a more clear depiction of the topography of the NW patches, an AFM topographic image from the ZnO-10-10-25 sample is provided in Fig. 2.7. The AFM system was operated in tapping mode to capture the profile. Line scanning profile corresponding to the tapping mode topographic image is plotted in Fig. 2.8.

### **2.3.1.3. Summary**

Physical property characterization reveals that Li doping reagent in the hydrothermal growth solution reduces the growth rate of the ZnO NWs. As a result, the length of the ZnO NWs decreases with higher Li doping concentration at the same growth condition. On the other hand, Li doping increases the number of NWs per unit area. However, Li doping does not have much effect on the diameter of the NWs. The average diameter of the NW depends on the seed layer instead. In addition, the diameter is found to vary significantly within a specific NW patch for a specific device.

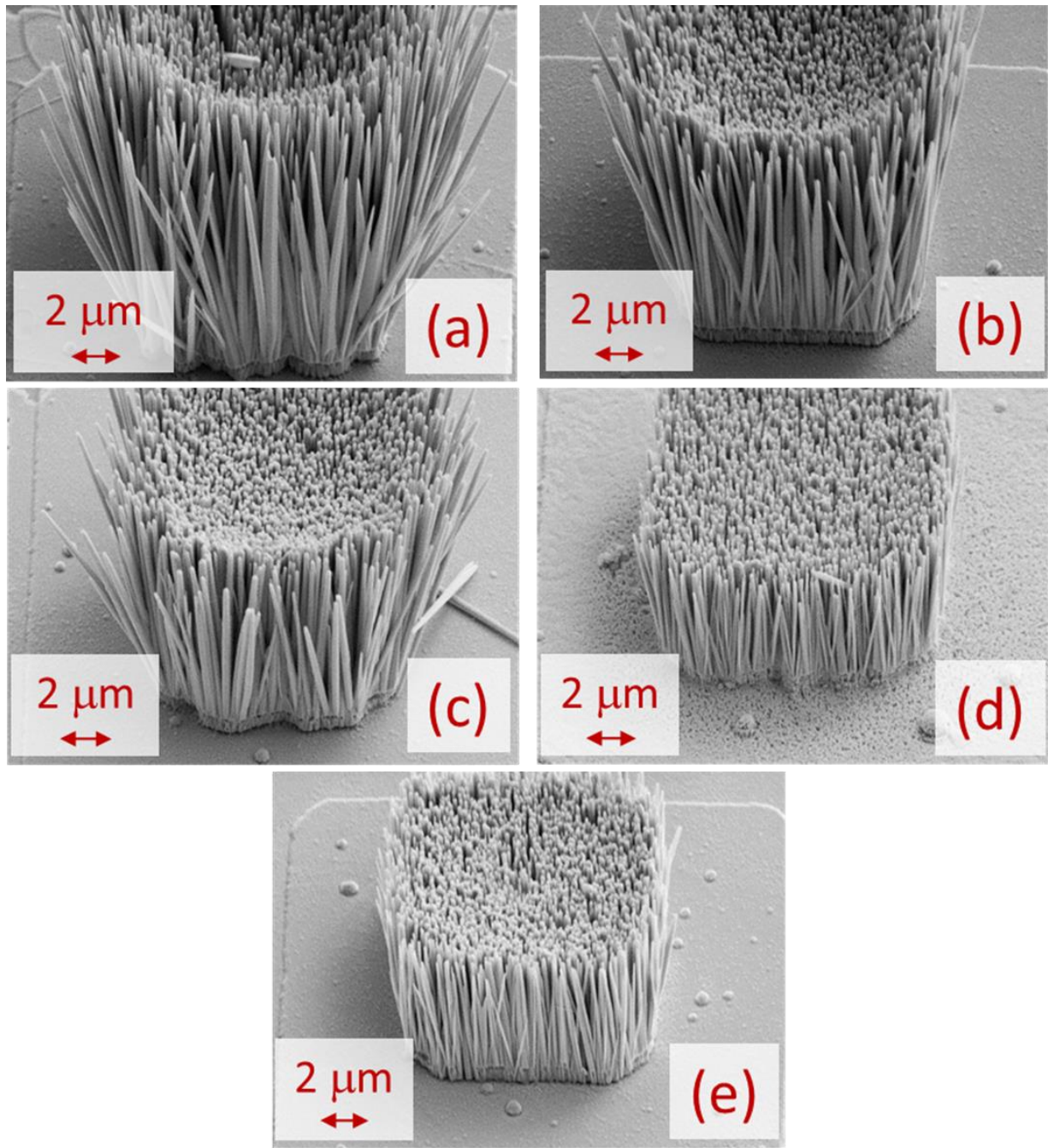


Figure 2.4: (a) – (e) SEM images of the NW patches with the stage tilted at  $45^\circ$ . (a) ZnO-10-10-0 (b) ZnO-10-10-7 (c) ZnO-10-10-10 (d) ZnO-10-10-15 (e) ZnO-10-10-25.

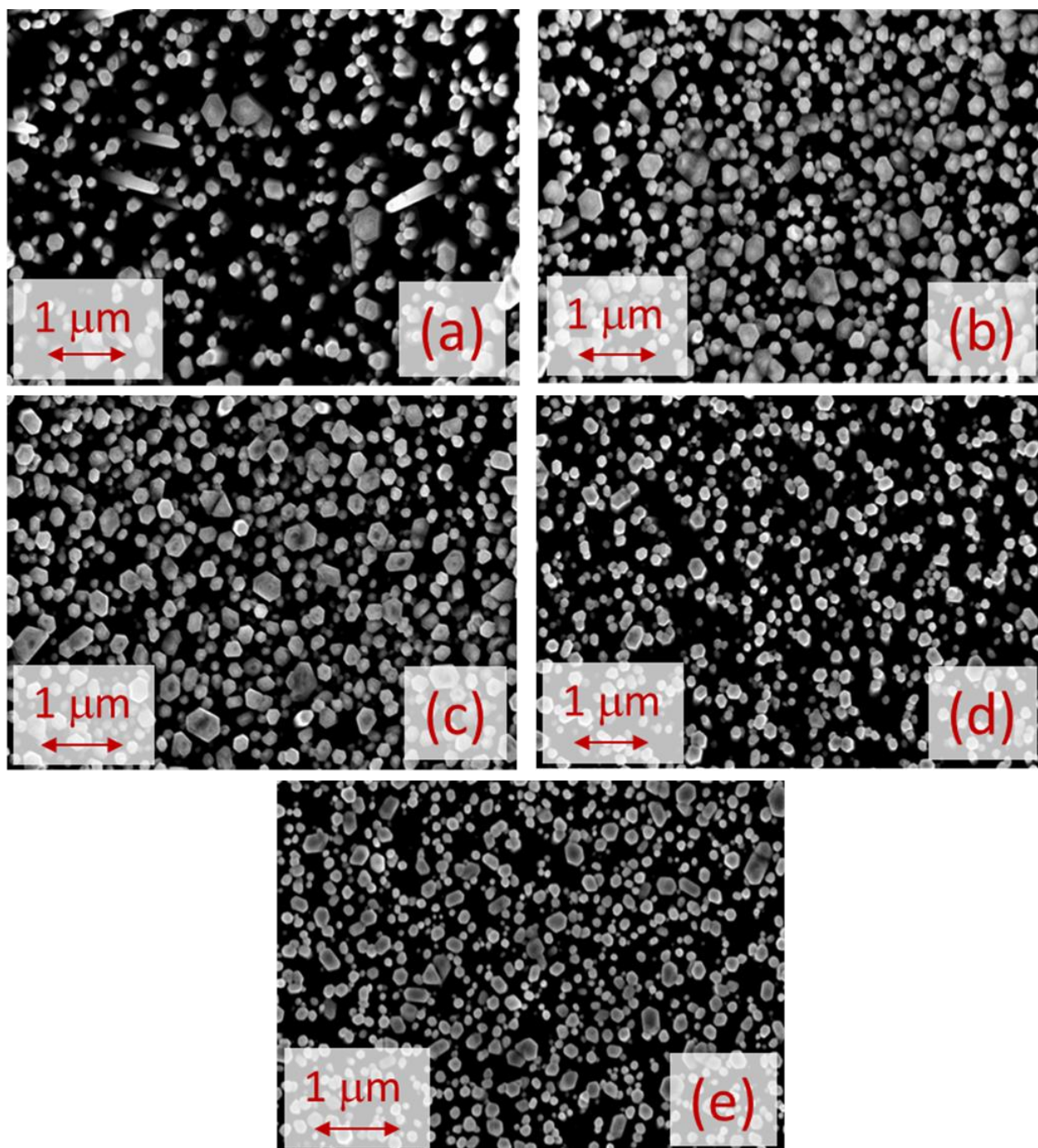


Figure 2.5: (a) – (e) SEM images of the NW patches without tilting the stage. (a) ZnO-10-10-0 (b) ZnO-10-10-7 (c) ZnO-10-10-10 (d) ZnO-10-10-15 (e) ZnO-10-10-25.

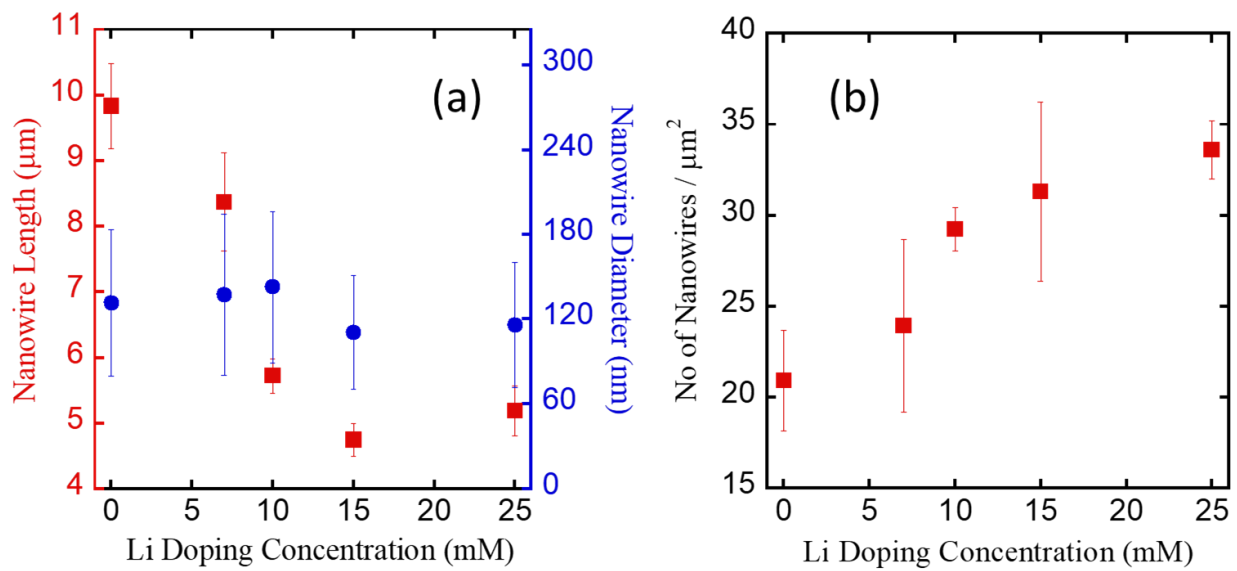


Figure 2.6: (a) Variation of average NW length and diameter with Li doping concentration. Here, ZnO NWs were assumed to have a circular cross-section instead of the hexagonal in reality. (b) Variation in the average density of NWs with Li doping concentration.

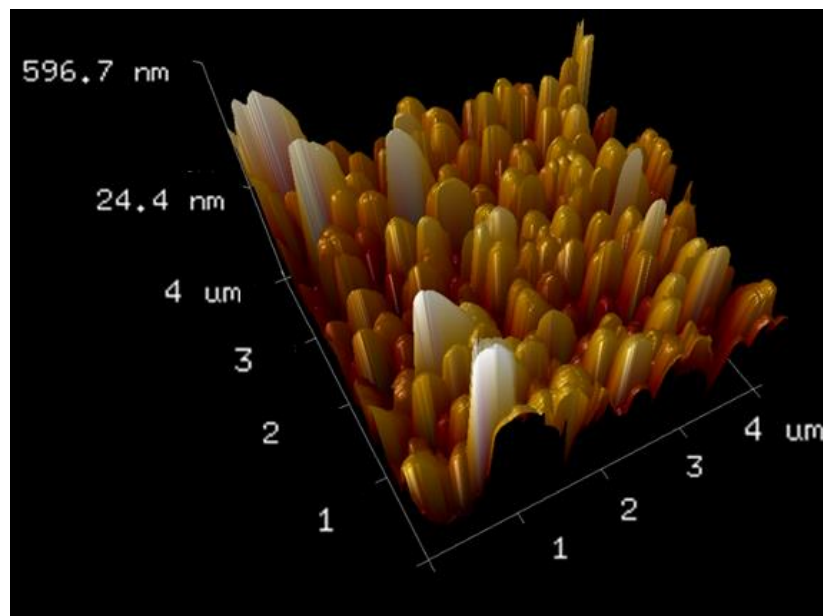


Figure 2.7: NW patch topography from the ZnO-10-10-25 sample created using the tapping mode of an AFM system.

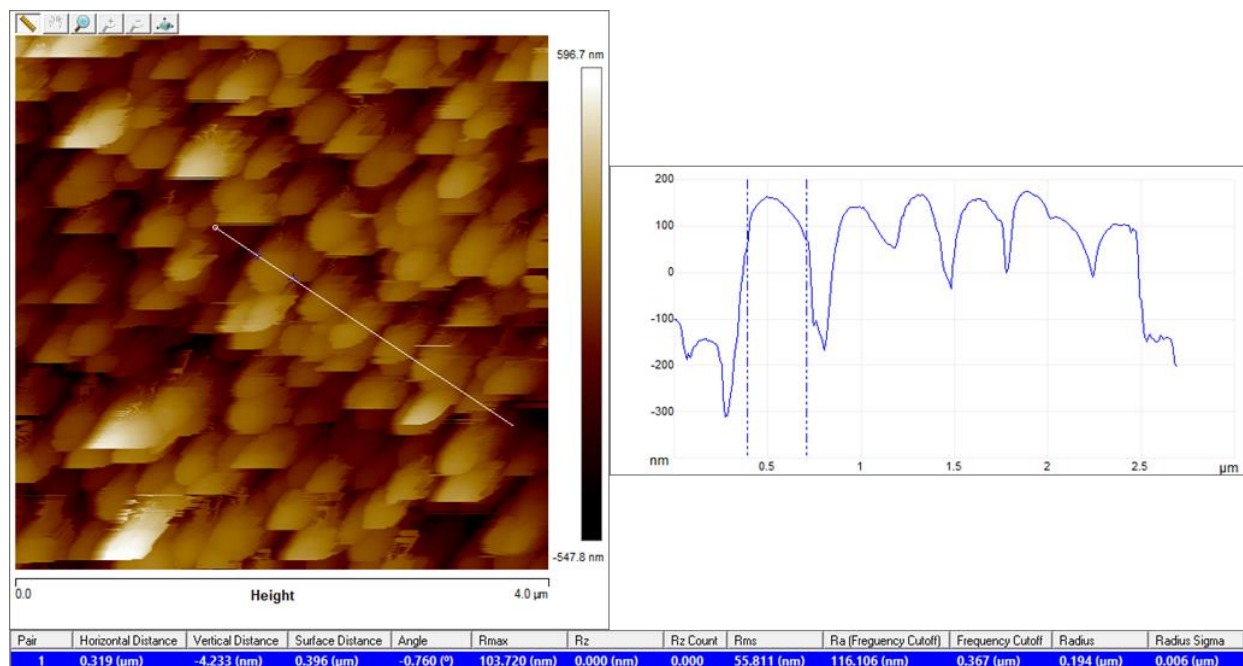


Figure 2.8: A typical line scan profile for the ZnO-10-10-25 sample from the AFM topography using the tapping mode.

## 2.3.2. Material and electromechanical property characterization

Extensive material characterization has been conducted on the as-grown NWs to investigate the effect of Li doping onto the ZnO NWs. The following section discusses the material characterization techniques used in this work and the corresponding results.

### 2.3.2.1. Raman spectroscopic analysis

A DXR™ Raman microscope was utilized to observe the vibrational modes of the NWs. A high resolution grating and 532 nm laser source were used for this analysis.

ZnO lies in the  $C_{6v}^4$  space group. The group theory predicts the optical phonon of  $A_1 + 2B_1 + E_1 + 2E_2$  symmetries. The  $B_1$  vibrational modes associated with it are both Raman and

Infrared inactive. The  $E_2$  modes, however, are Raman active only. On the other hand, the  $E_1$  and  $A_1$  modes are both Raman and Infrared active [139].

The complete Raman spectrum shows the presence of  $E_2$ -low and  $E_2$ -high Raman active modes. In addition to that, one more peak from the vibration of Si atoms in the substrate is observed around  $520\text{ cm}^{-1}$  Raman shift. No additional peak is observed for any of the doped devices. The  $E_2$ -low mode is associated with the vibration of the heavy Zn sub lattice in the ZnO structure. This mode is almost at the same position for all of the devices, around  $99\text{ cm}^{-1}$  Raman shift. The  $E_2$ -high mode, on the other hand, is associated with the vibration of the O atoms in the ZnO structure. This mode is very sensitive to the introduction of any kind of impurities in the ZnO structure and thus, is of particular interest to us. The occupation of the Zn sites by smaller sized Li induces tensile stress in the O sites, which can cause a red shift in the  $E_2$ -high mode [82], [140]. Likewise, we have obtained a red shift in the  $E_2$ -high Raman active mode with increased Li concentration. This observation confirms that most of the Li atoms are substituting Zn atoms in the ZnO structure instead of occupying the interstitial positions. A sample Raman spectrum and the shift in the  $E_2$ -high mode with Li doping concentration are depicted in Figs. 2.9(a) and 2.9(b), respectively.

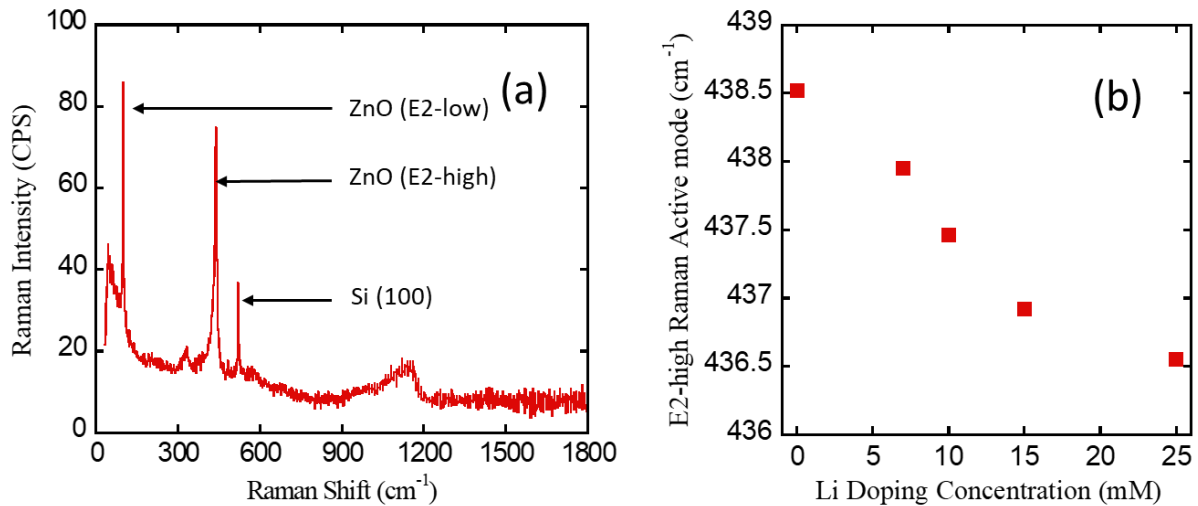


Figure 2.9: (a) A sample Raman spectrum from the ZnO-10-10-0 sample. (b) E2-high Raman active mode position with Li doping concentration. A red shift is observed in this mode due to the incorporation of Li.

### 2.3.2.2. X-Ray Diffractometric (XRD) analysis

To further study the crystal properties of the fabricated NWs, we have performed XRD analysis. The characterization tool used in this step is a Siemens D500 system, which employs a Cu  $K_{\alpha}$  X-ray source. The complete XRD spectrum (Fig. 2.10(a)) shows the presence of a dominant (0002) peak indicating the preferential growth of ZnO NWs in this direction. No additional phase was observed for the doped ZnO NWs. The high resolution (0002) XRD peak (Fig. 2.10(b)) is analyzed to calculate the vertical lattice constant  $c$  of the crystal structure. The lattice constant  $c$  is found to decrease with increasing Li concentration due to the smaller sized  $\text{Li}^+$  (0.6 Å) compared to  $\text{Zn}^{2+}$  (0.74 Å) it substitutes (Fig. 2.10(c)) [83] [72], [141]. In contrast, if most of the Li had incorporated into the lattice as an interstitial dopant, the lattice constant  $c$  should have increased [142].

The crystallite size of the NWs is also calculated from the same (0002) peak using the Debye-Scherrer formula [143]. It is found to increase with increasing doping concentration (Fig. 2.10(d)). This outcome is consistent with the results found by Awan et al. [144] where they observed that substitutional Li doping can increase the crystallite size. However, the crystallite size decreases for highly doped ZnO-10-10-25 sample as a result of various compensation effects including the formation of acceptor complexes, deep levels, and dislocations which lead to lower structural quality [145], [69].

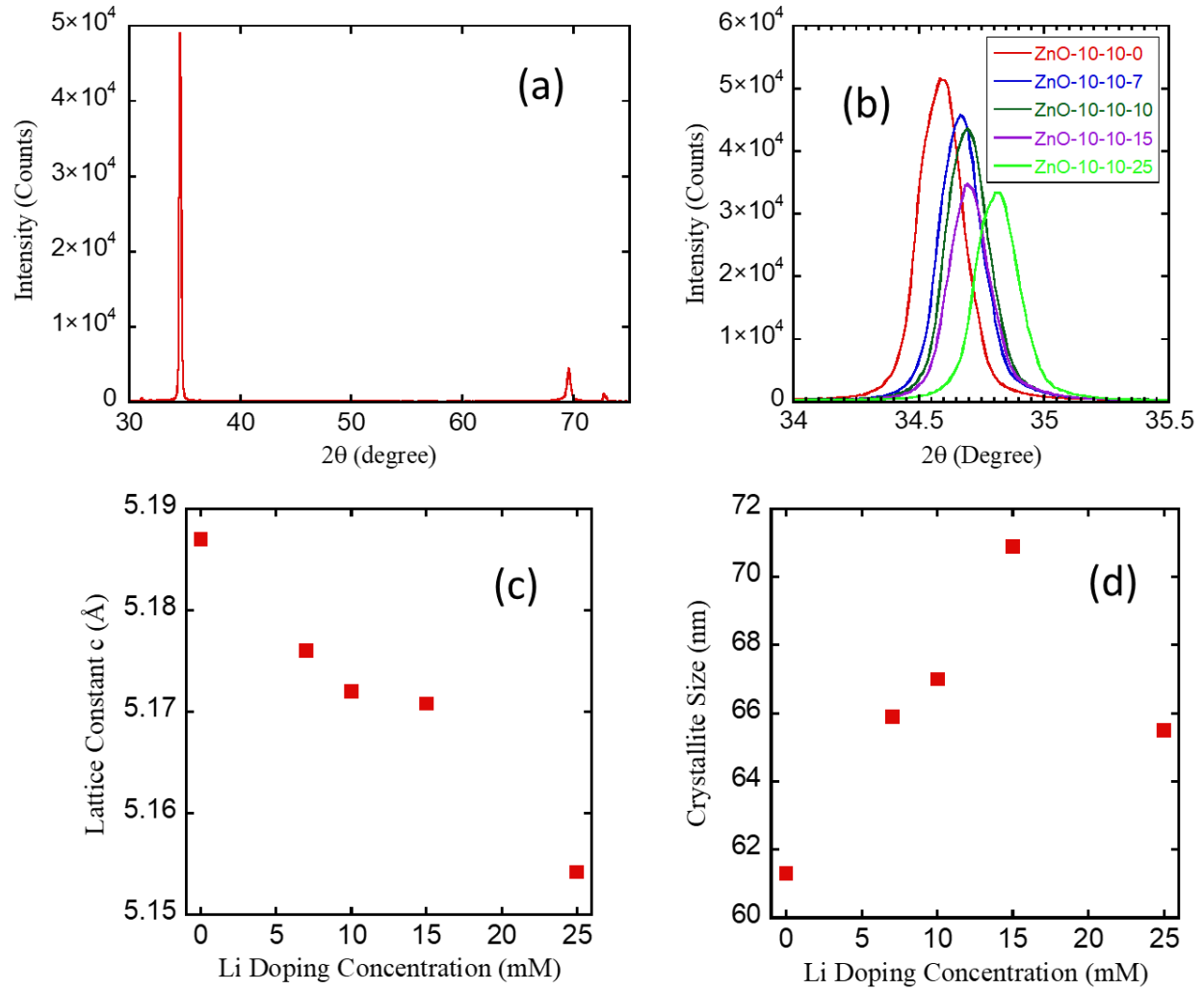


Figure 2.10: XRD analysis results on the fabricated NW devices. (a) A sample XRD spectrum from the ZnO-10-10-0 device. (b) High resolution scan around the (0002) peak position. (c) Vertical lattice constant  $c$  variation with Li doping concentration. (d) Crystallite size variation with Li doping concentration.

### 2.3.2.3. Energy Dispersive Spectroscopic (EDS) analysis

EDS analysis was then performed to quantify the atomic composition of the NWs. The atomic ratio of Zn:O was found to be greater than one (55:45), hence the sample is oxygen-poor. This represents the presence of oxygen vacancies and zinc interstitials, which can result in electron screening effect. Li could not be detected here as it is a light element [87].



#### 2.3.2.4. X-ray Photoelectron Spectroscopic (XPS) analysis

XPS analysis was performed in a Perkin-Elmer™ Phi 560 XPS/Auger system with Mg anode X-ray generation. A high resolution scan from 40 eV to 70 eV in Fig. 2.11 shows the presence of Li 1s core level peak around 53 eV ~ 54 eV for all of the doped devices. This also verifies the presence of Li in the doped devices.

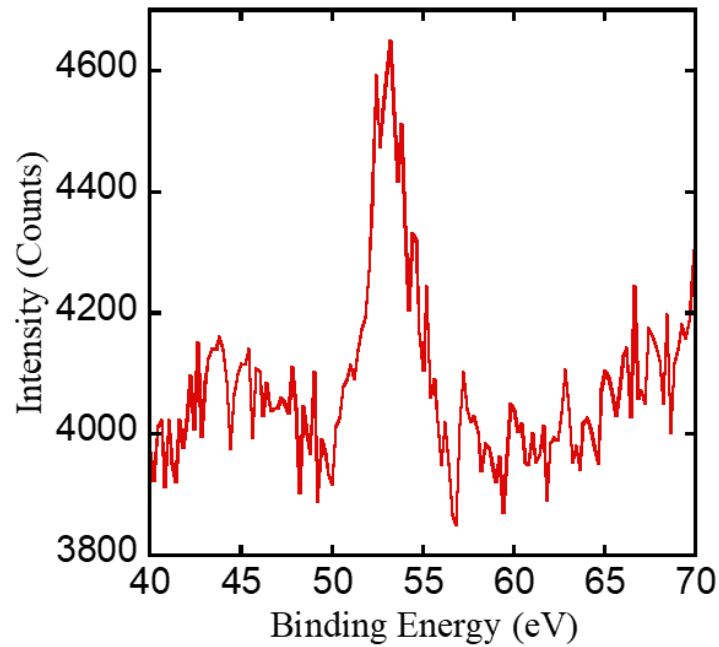


Figure 2.11: XPS scan around the Li 1s peak position for the ZnO-10-10-10 device. Core level Li 1s peak is observed around 53 eV ~ 54 eV binding energy for all of the doped devices.

#### 2.3.2.5. Summary

Material property characterization of the NWs reveals significant physics for the incorporation of Li into the ZnO structure. Raman spectroscopic analysis depicts that the  $E_2$ -high Raman active vibrational mode experiences a red shift with Li doping. This mode is associated with the vibration of the O atoms in the ZnO structure. This result supports the hypothesis of the substitution of Zn atoms by the Li atoms. As  $\text{Li}^+$  is smaller than  $\text{Zn}^{2+}$ , the substitution creates a tensile strain in the structure, which reduces the  $E_2$ -high

mode frequency. Therefore, Raman analysis validates that Li atoms are acting as a substitutional dopant into the ZnO structure.

The XRD analysis shows that the vertical lattice constant  $c$  of the ZnO lattice structure reduces with Li doping concentration. This also verifies that most of the Li atoms are incorporated into the ZnO lattice structure as a substitutional dopant instead of an interstitial dopant. The size of  $\text{Li}^+$  (0.6 Å) is smaller than the size of  $\text{Zn}^{2+}$  (0.74 Å). This is the primary reason for the gradual decrease of the lattice constant with Li doping as substitution of a bigger  $\text{Zn}^{2+}$  by  $\text{Li}^+$  shrinks the lattice structure of the ZnO. In addition, XRD analysis also reveals that the crystallite size of the NWs also increases with the Li doping concentration.

EDS and XPS analyses are also performed on the devices to obtain a quantitative analysis from the NWs. Although Li could not be detected in EDS due to its small size, EDS does estimate the presence of oxygen vacancies and zinc interstitials in the ZnO NW structure. XPS spectrum on the other hand, also verifies the presence of Li atoms in the doped ZnO NW structures.

When Li acts as a substitutional dopant into the ZnO structure, it behaves like a p-type dopant. On the other hand, if it acts as an interstitial dopant, it behaves like a n-type dopant. Therefore, our results conclude that Li is incorporated into the ZnO structure as a p-type dopant. Intrinsic ZnO is n-type because of oxygen vacancies and zinc interstitials [70]. As a result, it suffers from electron screening effect which screens a significant portion of the piezoelectric charge. This highly degrades the ZnO NW performance. P-type doping in ZnO can reduce the excess charge and improve the NW sensitivity. In addition, lattice constant reduction induces an extra amount of anisotropy on the ZnO structure, which can improve the piezoelectric coefficient.

### 2.3.3. Piezoelectric response characterization

Extensive piezoelectric characterization has been conducted on the fabricated NW devices to illustrate their performance as the basic material for piezoelectric energy harvesters and nano-sensors. An AFM system was operated in contact mode to exert a specific amount of force on the NWs and record the corresponding response. The following subsections discuss the piezoelectric characterization setup and results.

#### 2.3.3.1. Piezoelectric characterization setup

A Bruker Dimension 5000 AFM system was operated in contact mode to vertically tap the NWs and exert a controlled amount of force. A TESP tip (Bruker Inc.) coated with Au/Ti was used as the AFM tip which creates an Ohmic contact with the NWs due to the comparable value of the electron affinity of ZnO and the work function of Au/Ti layer [146]. Fig. 2.12 depicts the SEM image of the AFM tip [147].

When NWs are compressed along the principal axis, the longitudinal piezoelectric coefficient,  $d_{33}$  can be measured, while lateral bending induces the  $d_{31}$  mode. Due to the small dimension of the AFM tip and diameter of the NWs, it is challenging to land the AFM tip exactly on top of a single NW. Therefore, in this research, the primary focus was the study of the  $d_{31}$  mode. A positive voltage is generated on the tip in  $d_{31}$  mode with respect to the ground electrode, whereas in  $d_{33}$  mode, the compressive stress induced by the AFM in vertical direction generates a negative voltage. Fig. 2.13 shows the AFM tip – NW interaction schematic for our experimental setup.

This setup differs from what has been previously reported on energy harvesting from ZnO NWs using an AFM system. In [132] and [148], the researchers have formed a Schottky barrier between their Pt-coated Si AFM tip and the NW while scanning the tip across the NWs. This allowed them to contact both the tensile and the compressively stressed sides of the NW. During the scanning process, in the first phase, the AFM tip remained in contact with the tensile stressed side. In the second phase, the AFM tip ran across

the top of the NW and contacted the compressively stressed side. In contrast, in our set-up, the AFM tip always contacts the tensile stressed side of the NWs as shown in Fig. 2.13. Due to the vertical tapping in  $d_{31}$  mode and the existence of an Ohmic contact between the tip and the NW, we will only observe positive voltages at the output, whereas, Pradel et al. [132] and Lu et al. [148] reported positive and negative polarity voltages generated by the Schottky contact between the tip and the p-type and n-type NWs, respectively.

In order to extract the electrical signal from the NWs, a conductive AFM probe holder (model DSCMSCH, Bruker Inc.) is used. The AFM tip was made to contact the NW patches at a frequency of 0.33 Hz. The generated piezoelectric voltage ( $V_g$ ) is fed to a nano voltmeter (Keithley 2182A) and read by Labview™ across a 6.7 MΩ load resistance ( $R_L$ ). The total experimental setup was placed inside a grounded enclosure to protect it from any kind of noise and interference. The schematic for the setup is depicted in Fig. 2.14.

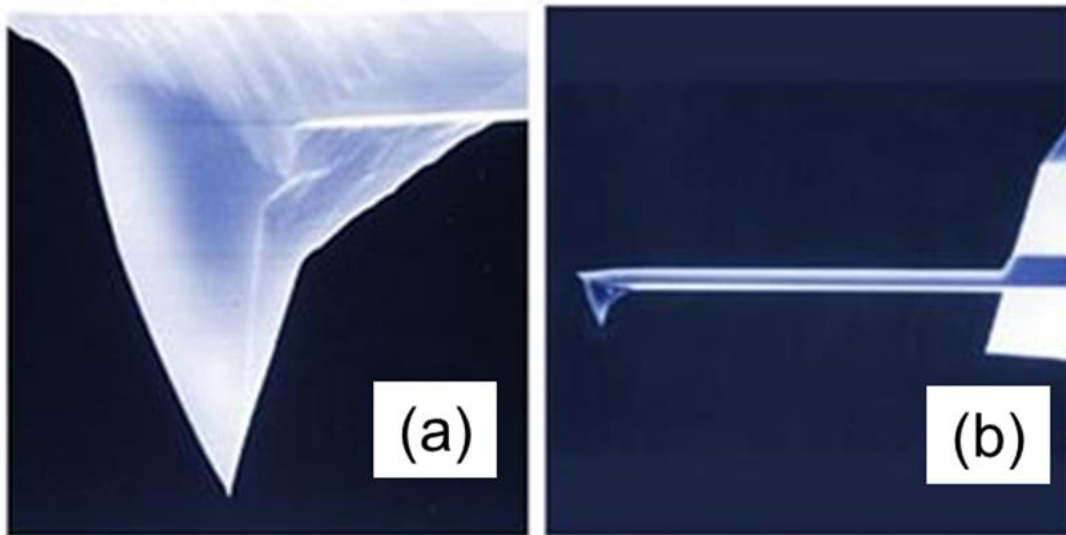


Figure 2.12: SEM image of the Au coated AFM cantilever tip. In addition to applying mechanical excitation to the NWs, the tip also acted as the top electrode for the nanowire devices. (a) AFM tip. (b) AFM tip with cantilever [147].

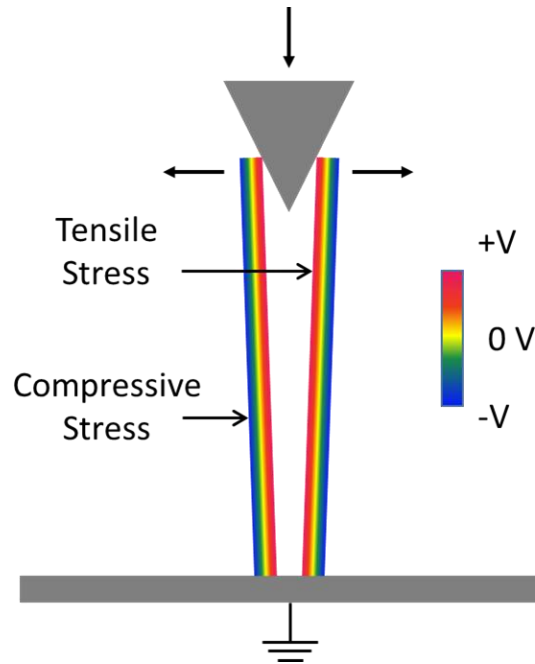


Figure 2.13: Schematic illustration of an AFM tip - NW interaction for the  $d_{31}$  mode. When the NWs are bent, a positive voltage is generated in the side that experiences a tensile stress. On the other hand, negative voltage is generated on the compressively stressed side.

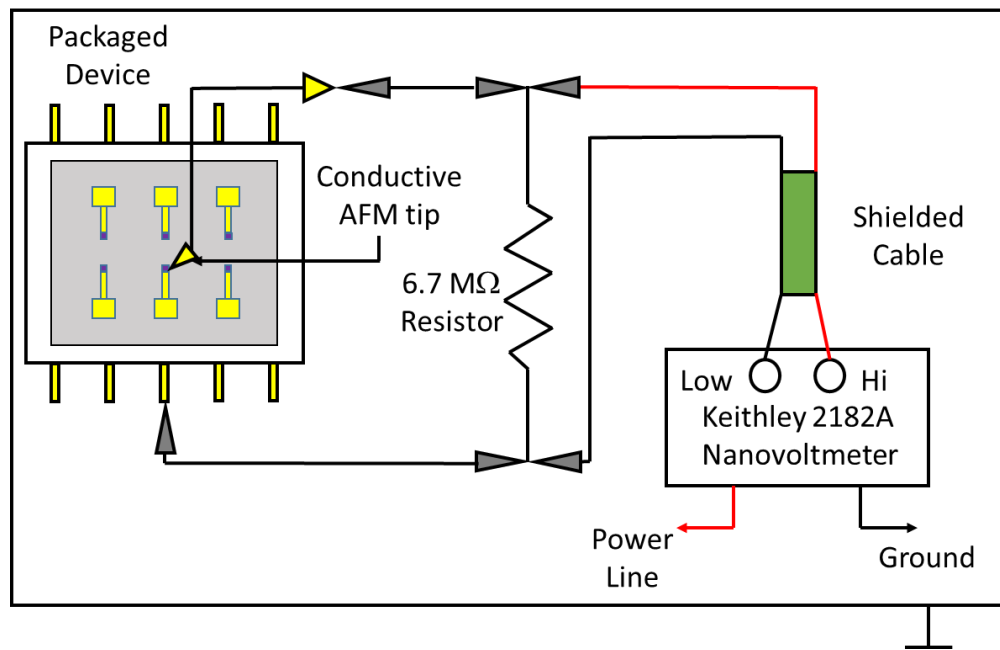


Figure 2.14: Piezoelectric response measurement setup.

The Keithley 2182A nano voltmeter can detect voltages in nV range with excellent signal to noise ratio (SNR). The voltage detected by the nano voltmeter is recorded by a LABVIEW™ code. To apply force on the NWs, the advanced force mode of the contact AFM system is utilized. This mode gives the flexibility of controlling the motion of the AFM tip in z direction. The tip can extend and retract in the NW array vertically and in the process of doing so, it can apply a defined amount of force on the NWs and bend them laterally.

While extending and retracting in the NW array, due to the contact with the NWs, the AFM cantilever experiences a deflection. The AFM can detect and measure this deflection using a laser-split photodiode system as a voltage signal. The measured deflection can be used to calculate the amount of force exerted by the AFM tip on the NW array. Conversely, a set point for the deflection of the cantilever can be also set, which will in turn, ensure the exertion of a defined amount of force. The schematic for the AFM cantilever deflection measurement system is depicted in Fig. 2.15 [58].

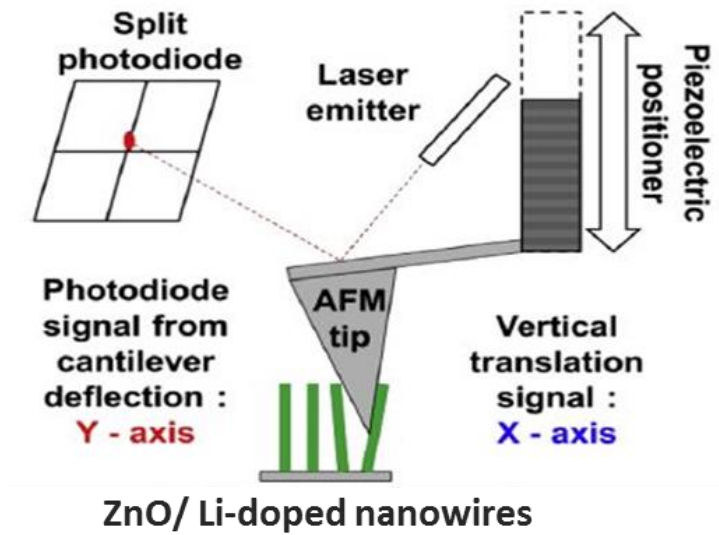


Figure 2.15: Schematic of the AFM cantilever deflection measurement system [58] (Reprinted with permission. Copyright © 2013, Elsevier).

To calculate the force applied by the cantilever tip corresponding to a specific deflection set point, Hooke's formula is used [149].

$$F = k_{cant} \times d_{cant} \quad (2.4)$$

$$\text{Or, } F = k_{cant} \times S_v \times V_t \quad (2.5)$$

Here,  $F$  is the applied force (N),  $d_{cant}$  is the deflection of the cantilever (m),  $k_{cant}$  is the spring constant of the cantilever (N/m). The nominal value of spring constant for the TESP cantilever used in this experiment is 42 N/m. Finally,  $V_t$  is the threshold voltage or trigger voltage or set point voltage (V). When the tip extends into the nanowire array, the cantilever bends until the set point voltage is registered by the split photodiode.

The force plot gives us important information about the AFM tip-NW interaction. This is a graphical interpretation of the movement and deflection of the AFM tip. In this plot, the X axis represents the vertical movement of the AFM tip whereas the Y axis represents the deflection of the tip recorded by the split photodiode. The sensitivity  $S_v$  can be determined from the slope of the steep area of this force plot. In addition, the force plot also provides us information about the nature of the AFM tip-nanowire interaction. A sample force plot for a 6V trigger voltage is shown in Fig. 2.16.

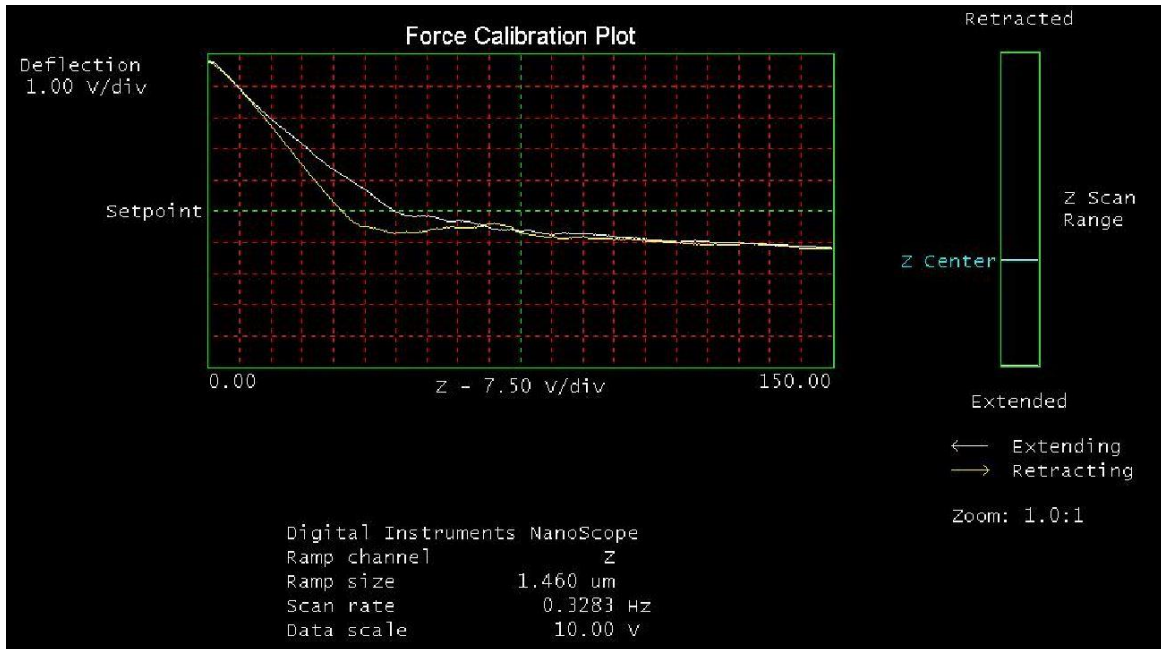


Figure 2.16: A sample force plot for the AFM tip-nanowire interaction. X axis represents the vertical movement of the AFM tip and the Y axis represents the deflection of the AFM cantilever. For this particular curve, trigger voltage or set point was set to 6V.

### 2.3.3.2. Piezoelectric characterization results

The NWs were found to survive more than 35000 vertical taps over a period of 18 months by the AFM tip with no significant degradation in performance. This represents the stable and robust structure of the ZnO NWs.

Sample piezoelectric responses from the devices are presented in Fig. 2.17. Although the trigger voltage of the AFM was set to the same value, each time the tip engages the NWs, the interaction is slightly different. Therefore, a variation in the generated voltage  $V_g$  is observed. This would not pose a problem since the generated energy is typically integrated and stored over a time in typical applications. In order to mimic this, statistical analysis is performed on the distribution of  $V_g$  to find the average  $\langle V_g \rangle$ . However, the distribution was highly skewed to the right, which would lead to the overestimation of the average.



Following the statistical methods in [150], [151], a log transformation was performed. The data distribution was found to be log-normal [152]. Then, the average generated voltage was computed from the transformed data as:

$$\langle V_g \rangle' = 10^{\langle \log V_g \rangle} \quad (2.6)$$

Sample transformed generated voltage distribution data are shown in Fig. 2.18. The log transformed average generated voltages  $\langle V_g \rangle'$  are plotted as a function of Li doping concentration in Fig. 2.19.

Due to the different NW dimensions in differently-doped devices, the average force exerted by the AFM tip is different for each device. Therefore, for meaningful comparison of the generated voltage between differently doped NWs, it needs to be normalized by the exerted force. The average applied force  $\langle F_{AFM} \rangle$  is calculated using the Hooke's formula from the force curves of the AFM system [58], [149]. Then the force-normalized average generated voltage  $\langle V_g \rangle'_{FN}$ , representing the sensitivity of the NWs is:

$$\langle V_g \rangle'_{FN} = \langle V_g \rangle' / \langle F_{AFM} \rangle \quad (2.7)$$

It is evident from Fig. 2.19 that the sensitivity of the NWs increases with Li doping concentration. In fact, ZnO-10-10-25 exhibits ~22x higher sensitivity than the undoped sample. The sensitivity improvement, however, is a combination of physical, material, electromechanical and piezoelectric property modifications. Li doping changes the growth pattern and therefore the length and density of the NWs. It also reduces the lattice constant and increases the crystallite size. In addition, Li, as a p-type dopant, decreases the free electron concentration and therefore the resultant electron screening effect. To differentiate the impact of pure physical changes (size and density) from that stemming from material properties, we performed the Finite Element Method (FEM) analysis and simulations.

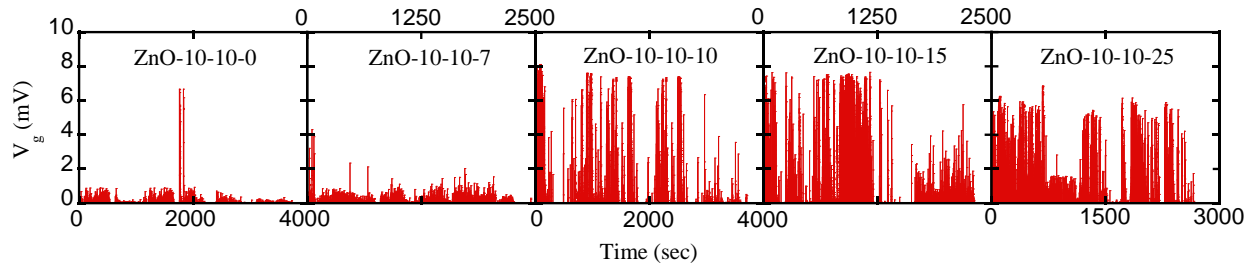


Figure 2.17: Sample piezoelectric output response from the NW devices. An AFM tip was used to apply force on the NWs. Only the  $d_{31}$  mode or the positive voltages are analyzed which are associated with the bending of the NWs. The labels for the x-axis are staggered for clarity.

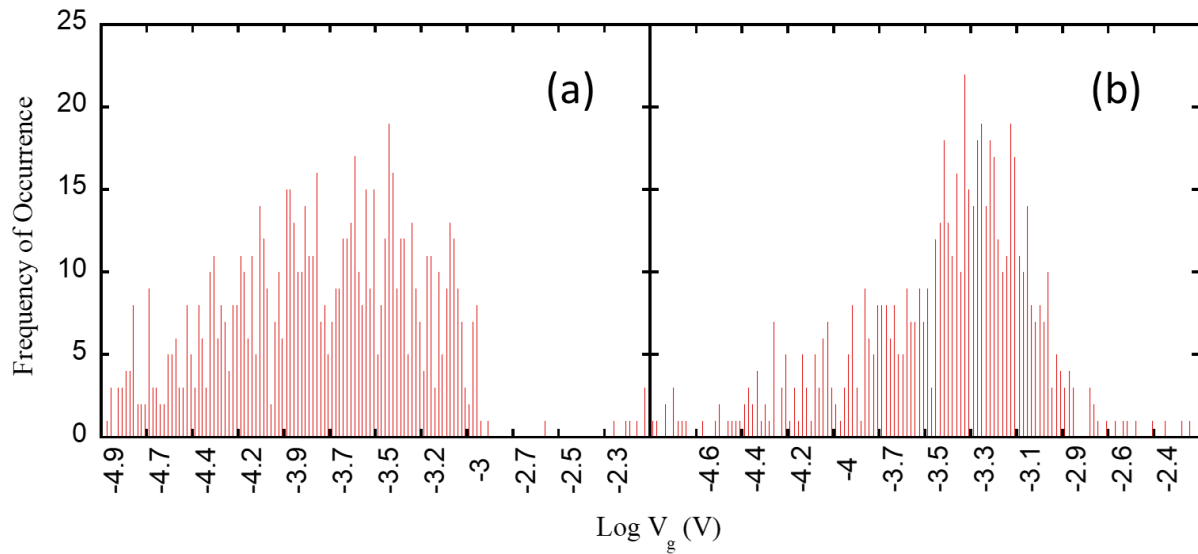


Figure 2.18: Sample log-transformed distribution curves for the piezoelectric output voltage measured on (a) ZnO-10-10-0 and (b) ZnO-10-10-7 samples. Log transformation is implemented to remove the effect of skewness and perform a more accurate statistical analysis.

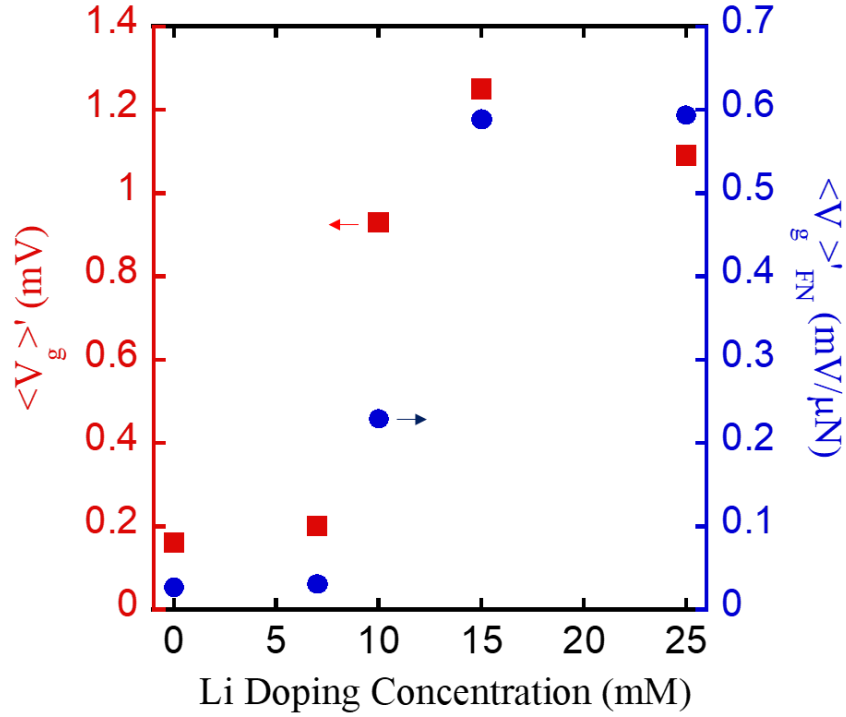


Figure 2.19: Average measured generated voltage  $\langle V_g \rangle'$  and force-normalized average measured generated voltage  $\langle V_g \rangle'_{FN}$  from NWs with respect to doping concentration.  $\langle V_g \rangle'_{FN}$  also represents the sensitivity of the NWs. More than 22-fold improvement in the sensitivity is observed due to the incorporation of Li dopants into the ZnO NWs.

### 2.3.3.3. Summary

The piezoelectric response analysis reveals that the sensitivity of the ZnO NWs gets a significant boost with the incorporation of Li. In fact, ~22-fold improvement in the sensitivity is achieved through substitutional Li doping on the ZnO NWs. The improvement is associated with the reduction in the electron screening effect and the lattice constant. In addition, Li doping also reduces the charge leakage from the ZnO structure, resulting in improved sensitivity. This sensitivity improvement, however, is a combination of both physical and material property modifications, which will be decoupled in the next section.

## 2.4. Piezoelectric performance simulation

### 2.4.1. Average nanowire displacement simulation in Coventorware™

A model of the AFM tip and NW system was created in Coventorware™ software. To construct the NWs, measured parameters from the physical characterization (Table 2.2) are used. The AFM probe on the other hand, was created with the dimensions provided by Bruker Corporation [153]. The length, width, and thickness of the cantilever are 125  $\mu\text{m}$ , 40  $\mu\text{m}$  and 4  $\mu\text{m}$  respectively. The pyramidal AFM tip was constructed from the AFM cantilever with a 15  $\mu\text{m}$  height and  $25^\circ$  surface inclination. A force patch is also placed on the cantilever (on the top surface of the tip) to apply the desired force on the AFM - NW system.

Since it is not known how Li doping affects the electromechanical properties of ZnO, pure ZnO bulk material and piezoelectric properties were fed into simulations. For bulk ZnO, the isotropic value of Young's modulus is 129 GPa whereas the Poisson's ratio is 0.349. The piezoelectric coefficients  $e_{kp}$  and the dielectric constant matrix elements  $\kappa_{ik}$  used are  $e_{15} = -0.45$ ,  $e_{31} = -0.51$ ,  $e_{33} = 1.22$  and  $\kappa_{11} = 7.77$ ,  $\kappa_{33} = 8.91$ , respectively [59], [52].

As boundary conditions, motion was restricted in all directions at the bottom of the NW surface and at the base of the cantilever holding the AFM tip (Fig. 2.20(a)), while contact boundary conditions were applied to the contacting surface of the NW and the AFM tip. Although in a real AFM system, the base of the cantilever moves downwards to apply force on the NWs, in simulations the force was applied on top of the AFM tip through the cantilever. In addition, ZnO NWs grow as a hexagonal prism, which was taken as a cylinder for simplicity. We have assumed that the NWs are arranged regularly within a device, although in reality, their arrangement is random.

The model was then solved to find the displacement of each NW using FEM in the MemMech solver of Coventorware™. Fig. 2.20(b) depicts a sample simulation result. For the applied force, the tip displaces four of the adjacent NWs.

Table 2.2: Parameters used for the construction of the NW model in Coventorware™ simulations and the resultant NW displacement values

Device	Circular Diameter D (nm)	Spacing S (nm)	Length L (μm)	Aspect Ratio L/D	Applied Force F (μN)	Average Nanowire Displacement d (nm)
ZnO-10-10-0	132	202	9.84	74.55	6.13	17.72
ZnO-10-10-7	138	179	8.37	60.65	6.45	22.15
ZnO-10-10-10	142	141	5.73	40.35	4.03	11.15
ZnO-10-10-15	111	162	4.75	42.79	2.13	3.69
ZnO-10-10-25	116	148	5.19	44.74	1.84	5.10

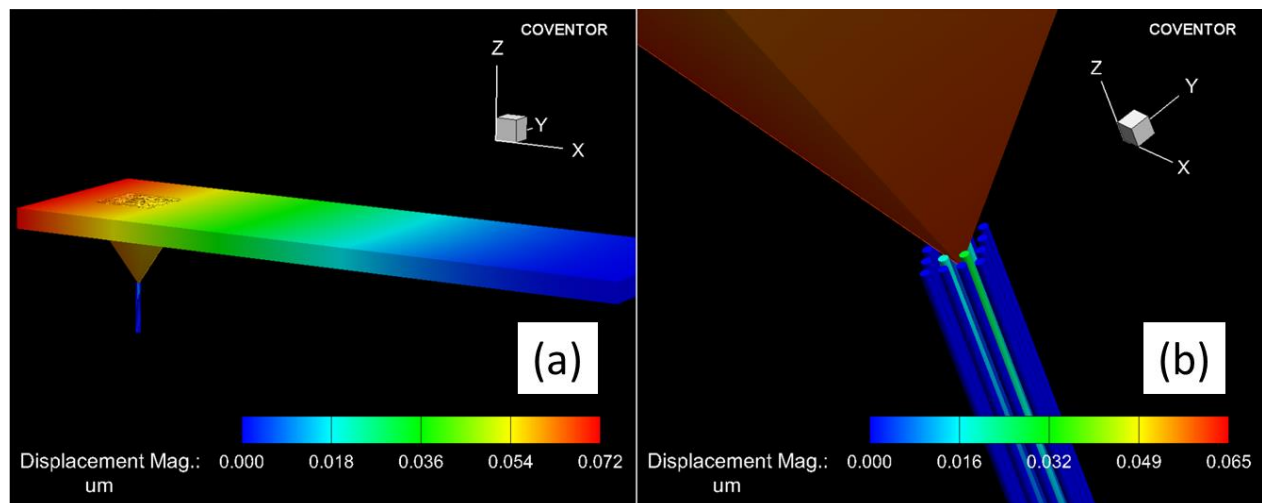


Figure 2.20: (a) – (b) A sample Coventorware™ simulation result for the displacement of the NWs due to the applied force by the AFM tip. (a) Displacement in the entire model. (b) Displacement of the AFM tip and NWs only (zoomed image of (a)).

#### 2.4.2. Piezoelectric response simulation in Ansys™

Each of the NWs in the NW patch that experiences bending acts as a voltage source ( $V_i$ ,  $i=1, 2, \dots, n$ ) in series with a contact resistance between the NW and the AFM tip ( $R_i$ ) (Fig. 2.21). Since  $R_i \ll R_L = 6.7M\Omega$ , the simulated voltage  $V_s$  induced across  $R_L$  will be the average of the voltages

generated by each of the NWs. As the piezoelectric effect is a linear interaction between displacement and generated voltage, the displacement of each NW in the patch can be replaced in the simulation with an average displacement by a single representative NW. This average displacement obtained from Coventorware™ was then applied to a single NW model in Ansys™ to determine its piezoelectric response  $\langle V_s \rangle$ . The process was repeated for each differently-doped device. The applied force and the corresponding simulated average displacement of NWs from Coventorware™ are presented in Table 2.2. A sample piezoelectric simulation result from Ansys™ is shown in Fig. 2.22.

The piezoelectric output voltage  $\langle V_s \rangle$ , thus simulated, is again normalized with respect to the applied force as  $\langle V_s \rangle_{FN} = \langle V_s \rangle / \langle F_{AFM} \rangle$  to remove the effect of force variation.  $\langle V_s \rangle_{FN}$  is then plotted as a function of average NW length and diameter as shown in Fig. 2.23. As noted earlier, for all devices, the same material properties were used in the simulations regardless of the doping concentration. Therefore, the variation in  $\langle V_s \rangle_{FN}$  represented in Fig. 2.23 should be only due to the variation in the dimensions of NWs for each device, not Li doping concentration.

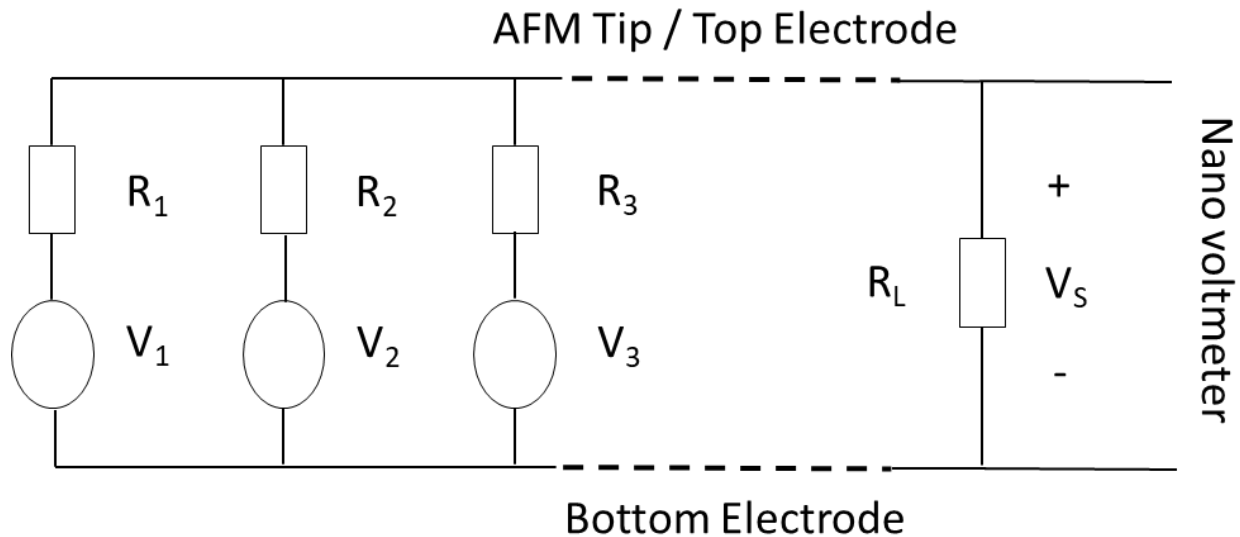


Figure 2.21: Equivalent circuit model for the AFM tip-NW interaction system.

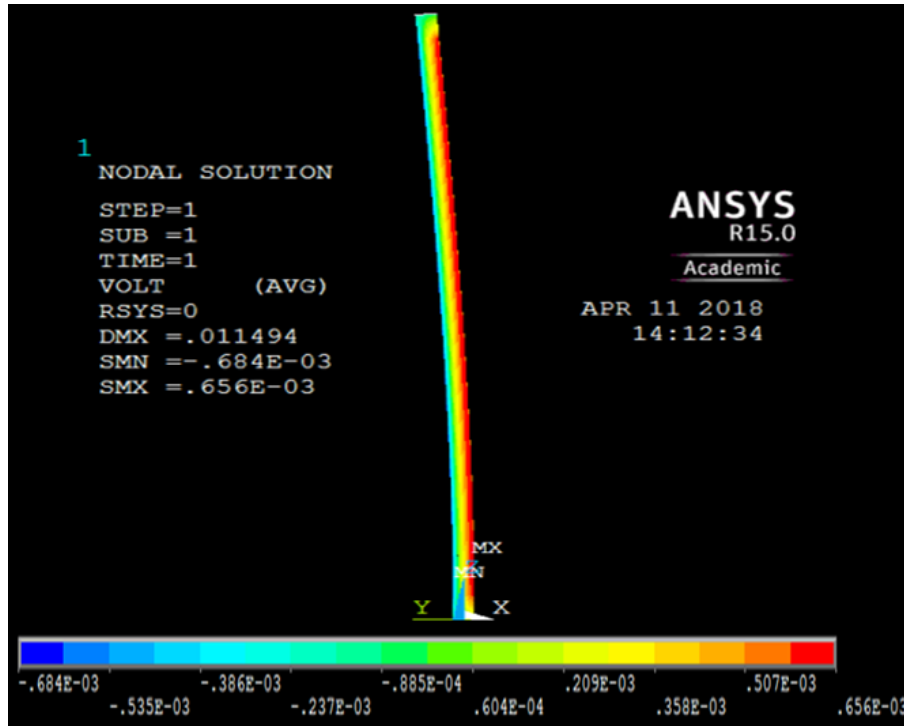


Figure 2.22: Sample simulation result in Ansys™ showing the piezoelectric output response of a single NW due to the average displacement calculated from Coventorware™ simulations.

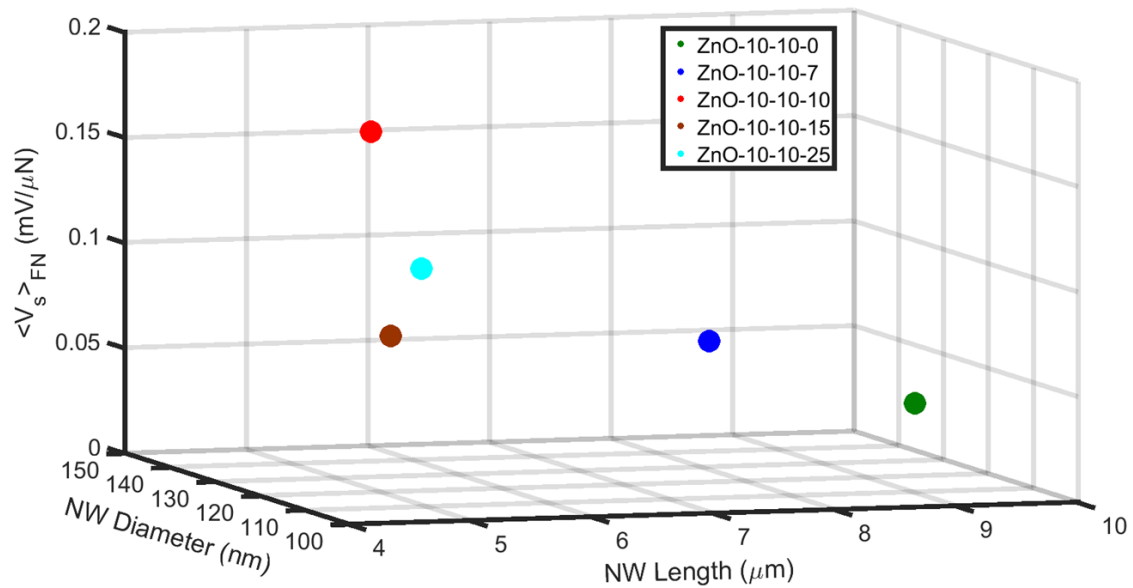


Figure 2.23: Force-normalized simulated piezoelectric output voltage  $\langle V_s \rangle_{FN}$ . Bulk ZnO material properties are used for all of the simulations regardless of the doping concentration.

### 2.4.3. Comparison between the experimental measurement and simulation

In order to determine the role of Li doping alone on the sensitivity improvement, decoupled from any geometry effects, the ratio of the normalized measured voltage to simulated voltage  $\langle V_g \rangle'_{FN} / \langle V_S \rangle_{FN}$  is plotted in Fig. 2.24. For the ZnO-10-10-0 device,  $\langle V_g \rangle'_{FN} / \langle V_S \rangle_{FN} = 1.04$ , close to the expected value of one, indicating agreement between the experimental and simulated values of our experiment. The slight mismatch might be due to the assumptions made in the simulations such as the periodic placement of NWs and the negligence of the distribution in NW size within a single patch. More importantly, in the absence of nano dimensional values, we have used bulk values for the Young's modulus, Poisson's ratio, piezoelectric coefficients, and the dielectric constant matrix elements. Young's modulus for ZnO NWs is known to depend on NW size [154]. It is reasonable to expect that the others would also.

As we have used bulk ZnO material properties for the simulation of the doped samples as well, the value of  $\langle V_g \rangle'_{FN} / \langle V_S \rangle_{FN}$  for the doped samples can provide us an estimation of how much piezoelectric sensitivity improvement has been achieved due to the modifications in the ZnO lattice and material properties alone, decoupled from the geometrical shape variation. The values higher than one are due to the improvement in the piezoelectric response. It is evident from Fig. 2.24 that incorporation of Li dopants improves the piezoelectric effect up to 7-fold in ZnO NWs.

### 2.4.4. Summary

The piezoelectric performance simulation reveals that besides material and electromechanical properties, physical property modifications also play a vital role behind the improved sensitivity of the ZnO NWs with Li doping. More than twenty two-fold improvement is observed in sensitivity due to the combined effect of modifications in the NW geometry, material and piezoelectric properties with the addition of Li. Finite element method simulations were performed to decouple the individual effect of Li



doping on the NW size and the piezoelectric coefficient and to see how much each effect plays a role in the sensitivity improvement. It is estimated that the changes in the material and piezoelectric properties alone are responsible for more than seven-fold improvement in the sensitivity.

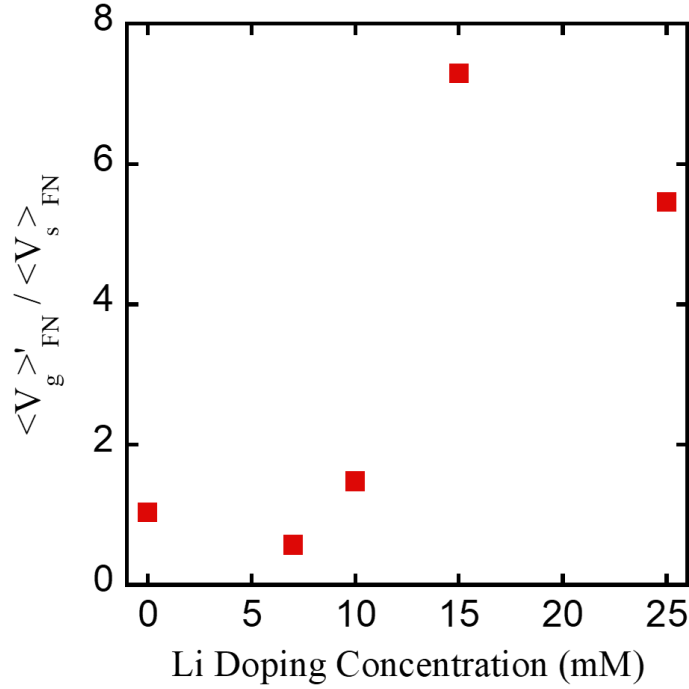


Figure 2.24: Comparison of the measured and simulated piezoelectric voltage generated in response to force applied by the AFM tip. For the ZnO-10-10-0 sample, the value of  $\langle V_g \rangle'_{FN} / \langle V_s \rangle_{FN}$  is very close to 1, indicating the close match for our experimental and simulated values. As for all the simulations, the bulk ZnO material properties are used regardless of the doping concentration. Therefore, the values of

$\langle V_g \rangle'_{FN} / \langle V_s \rangle_{FN}$  higher than one are due to the improvement in the piezoelectric response.

## 2.5. Analyses and discussions

The experimental values provide few interesting observations, crucial to the understanding of the physics of Li incorporation into the NWs and the corresponding modifications in their piezoelectric properties. In Fig. 2.17 and Fig. 2.19, it can be noted that there is not much improvement in  $\langle V_g \rangle'_{FN}$  for the

low doped sample ZnO-10-10-7 compared to the undoped sample. However, a sharp jump in  $\langle V_g \rangle'_{FN}$  is observed for ZnO-10-10-10 and higher doped samples, which can be explained with the change in its structural properties. As seen in Fig. 2.23,  $\langle V_S \rangle_{FN}$  for this sample is much larger compared to the other samples. As the material properties used in the simulations are the same for all of the samples irrespective of their doping concentration, the improvement in the output voltage for this sample is associated mainly with the physical shape of its NWs, not on the material properties. This conclusion can be more clearly observed in Fig. 2.24. The  $\langle V_g \rangle'_{FN} / \langle V_S \rangle_{FN}$  ratio, which is a measure of sensitivity improvement due to material properties only, does not exhibit a sharp jump for this sample. It is also evident from the same Fig. 2.24 that this ratio in fact decreases slightly for the ZnO-10-10-7 sample compared to the undoped sample. This slight decrease is within experimental error.

However, from the same Fig. 2.24, it can be clearly observed that there is indeed a very sharp jump in the  $\langle V_g \rangle'_{FN} / \langle V_S \rangle_{FN}$  ratio for ZnO-10-10-15 and ZnO-10-10-25 samples. To understand the physics behind this, we need to consider the Li diffusion mechanisms in ZnO. As discussed previously, Li can either occupy interstitial positions ( $Li_i$ ) or it can substitute a Zn atom and occupy its position ( $Li_{Zn}$ ). In general, Li acts as an amphoteric impurity in ZnO since  $Li_i^+$  acts as a shallow donor whereas  $Li_{Zn}^-$  acts as an acceptor and they coexist in the ZnO structure [155], [85]. In addition,  $Li_i^+$  is a highly mobile species whereas  $Li_{Zn}^-$  is significantly less mobile [156]. The mobile  $Li_i^+$  species can convert into less mobile  $Li_{Zn}^-$  by kicking out one Zn atom from the ZnO structure ( $Zn_{Zn}$ ) via kick-out mechanism producing another highly mobile Zn interstitial ( $Zn_i^{2+}$ ) species [157], [158].



$$E_f(Li_i^+) + E_f(Zn_{Zn}) < E_f(Zn_i^{2+}) + E_f(Li_{Zn}^-) \quad (2.9)$$

Such a kick-out mechanism has an energy barrier or activation energy ( $E_A$ ) of at least 1.56 eV [159], [158].

The isolated substitutional  $Li_{Zn}^-$  defect can also convert back into  $Li_i^+$  defect leaving a vacant position in the ZnO structure ( $V_{Zn}^{2-}$ ).



However, this mechanism requires a high activation energy of 3.4 eV, which makes  $Li_{Zn}^-$  defects rather stable [159].

The sharp improvement in the sensitivity of the ZnO-10-10-15 sample in Fig. 2.24 might be associated with this kick-out phenomenon. Knutsen et al. [157] observed a similar sharp change in the Li diffusion profile in a ZnO thin film. When the Li dopant concentration reaches a characteristic level, the activation energy is reached and a large fraction of  $Li_i^+$  ions convert into  $Li_{Zn}^-$  almost instantly following Eqn. 2.8. Moreover, this activation energy is a direct function of the active  $Li_i^+$  donor concentration,  $N_D$ . The activation energy decreases with the increase in the donor concentration [160], [161], [162].

$$E_A = E_I - \alpha(N_D)^{1/3} \quad (2.11)$$

Here,  $E_I$  is the ionization energy of a single isolated donor and  $\alpha$  is a constant.

Therefore, we suspect that the activation energy to convert the mobile donor  $Li_i^+$  to less mobile acceptor  $Li_{Zn}^-$  is reached when we increased the doping concentration from sample ZnO-10-10-10 to ZnO-10-10-15. As a result, a lot of interstitial Li is converted into substitutional Li via kick-out diffusion mechanism while trapping free electrons and producing  $Zn_i^{2+}$  ions. The  $Zn_i^{2+}$  ions on the other hand, are even more mobile than the  $Li_i^+$  ions and most of them are rapidly removed from the system [157]. Therefore, due to the large substitutional to interstitial Li ratio in the NWs, there will be a dramatic reduction in the electron screening effect and a large amount of anisotropy in the ZnO structure because of the smaller

sized substitutional Li. This anisotropy can again, improve the piezoelectric coefficient of ZnO NWs as discussed previously [82].

While we observe the sharp jump in Fig. 2.24 due to the kick-out mechanism, this sharp jump is not visible in the E2-high Raman active mode position and lattice constant  $c$  (Figs. 2.9(b) and 2.10(c), respectively). They are in fact quite linear. The reason behind this is the byproduct of the kick-out process,  $Zn_i^{2+}$ . Although this species is highly mobile and is removed rapidly from the system, few of them still remain in the ZnO structure as interstitials, opposing the sharp change in both E2-high Raman active mode and the lattice constant  $c$ .

The kick-out mechanism to convert  $Li_i^+$  into  $Li_{Zn}^-$  can lead to one more interesting phenomenon. The carrier concentration, and therefore the conduction type of the NWs will be determined by the ratio of the interstitial to substitutional impurities. As  $Li_{Zn}^-$  works as an electron trap center, the release of free electrons by  $Li_i$  enhances the stability of  $Li_{Zn}^-$ . On the other hand, as the concentration of  $Li_{Zn}^-$  increases, the Fermi energy ( $E_f$ ) moves toward the valance band ( $E_v$ ). This leads to an increase in the formation energy of  $Li_{Zn}^-$  while at the same time, the formation energy of  $Li_i^+$  goes down. This results in self-compensation and Fermi level pinning at the midgap, which is the reason behind the complication in obtaining p-type ZnO [155]. We suspect the existence of this phenomenon for the highly doped ZnO-10-10-25 sample. Furthermore, there might also be the formation of acceptor complexes, deep levels and dislocations in this sample as evident from Fig. 2.10(d). These two effects are responsible for the decrease in the  $\langle V_g \rangle'_{FN} / \langle V_s \rangle_{FN}$  ratio for the ZnO-10-10-25 sample compared to the ZnO-10-10-15 sample although it is still quite high compared to the undoped and low doped samples.

Fig. 2.24 gives us a valuable conclusion about the Li doping in ZnO NWs to improve its piezoelectric performance. As evident from this figure, there is an optimum level of Li doping concentration

which can give the best performance output from the ZnO NWs. For our specific experiment, we observed that optimum doping concentration for the ZnO-10-10-15 sample. Sohn et al. [69] also observed a similar outcome although they did not clearly explain the proper mechanism behind achieving this optimum output. Therefore, this dissertation can provide a guideline for the optimization of future high-performance nano-sensors and nano-energy harvester based on ZnO NWs.

## **2.6. Performance comparison table**

Table 2.3 demonstrates a relative comparison of the state of the art designs of ZnO NWs doped with different dopants with the presented Li-doped ZnO NWs. It is clearly evident from the Table that Li is the most effective dopant for improving the piezoelectric performance of ZnO NWs. This work obtained a 22.49 fold improvement on the piezoelectric performance of ZnO NWs with the incorporation of substitutional Li dopants. Only Sohn et al. achieved a better improvement in the performance where they also doped the ZnO NWs with Li. The presented work can therefore pave the way for high performance energy harvester and sensors based on ZnO NWs.

Table 2.3: Summary of recently reported undoped and doped ZnO nanowire piezoelectric performance

Reference	Doping Element	Force Application Area	Characterization Technique	Applied Input Signal	Output Voltage (V)		Output Voltage Improvement (×times)	Input Normalized Voltage		Input Normalized Output Voltage Improvement (×times)
					Undoped	Doped		Undoped	Doped	
This work	Li	Few nanowires (132 ~ 116 nm average diameter)	Vertical AFM tapping	6.13 ~ 2.13 μN	$1.6 \times 10^{-4}$	$1.25 \times 10^{-3}$	7.81	$2.61 \times 10^1$ (V/N)	$5.87 \times 10^2$ (V/N)	22.49
[163]	Cl	1 cm <sup>2</sup>	Stress along c-axis	1 MPa	2.4 (p.p.)	4.9 (p.p.)	2.04 (c)	$2.4 \times 10^{-2}$ (p.p.) (c) (V/N)	$4.9 \times 10^{-2}$ (p.p.) (c) (V/N)	2.04 (c)
[164]	Sb	Few nanowires (200-300 nm average diameter)	Lateral AFM scanning	5 nN	$-3.62 \times 10^{-2}$	$1.29 \times 10^{-2}$	0.36 (c)	$7.24 \times 10^6$ (c) (V/N)	$2.58 \times 10^6$ (c) (V/N)	0.36 (c)
[74]	S	--	Environmental vibration	500 gcm <sup>-2</sup>	$5.86 \times 10^{-1}$	$6.46 \times 10^{-1}$	1.1 (c)	$1.17 \times 10^{-3}$ (c) (V/gcm <sup>-2</sup> )	$1.29 \times 10^{-3}$ (c) (V/gcm <sup>-2</sup> )	1.1 (c)
[86]	Li	1.44 cm <sup>2</sup>	Acceleration from shaker	2 ms <sup>-2</sup> at 5 Hz	$1.4 \times 10^{-1}$	$6.3 \times 10^{-1}$	4.5	$7 \times 10^{-2}$ (c) (V/ms <sup>-2</sup> )	$3.15 \times 10^{-1}$ (c) (V/ms <sup>-2</sup> )	4.5 (c)
[75]	Ga	<7.07 cm <sup>2</sup> (c)	Hammer – stepper motor system	34 N at 1.4 Hz	1.8 (p.p.)	1.55 (p.p.)	0.86 (c)	$5.3 \times 10^{-2}$ (p.p.) (c) (V/N)	$4.6 \times 10^{-2}$ (p.p.) (c) (V/N)	0.87 (c)
[73]	Fe	<7.07 cm <sup>2</sup> (c)	Hammer – stepper motor system	34 N at 1.5 Hz	$5.97 \times 10^{-1}$	$6.96 \times 10^{-1}$	1.17 (c)	$1.76 \times 10^{-2}$ (c) (V/N)	$2.05 \times 10^{-2}$ (c) (V/N)	1.16 (c)
[76]	Ag	10 cm <sup>2</sup>	Sound wave – dB meter system	80 dB at 100 Hz	1.2 (p.p.) (c)	4 (p.p.)	3.3	$1.5 \times 10^{-2}$ (p.p.) (c) (V/dB)	$5 \times 10^{-2}$ (p.p.) (c) (V/dB)	3.3 (c)
[69]	Li	--	Sound wave	100 dB at 100 Hz	$9.67 \times 10^{-2}$ (p.p.) (c)	2.9 (p.p.)	30	$9.67 \times 10^{-4}$ (p.p.) (c) (V/dB)	$2.9 \times 10^{-2}$ (p.p.) (c) (V/dB)	30 (c)

Here, (p.p.) refers to peak to peak and (c) refers to the values calculated from the data provided in the relevant manuscript.

## 2.7. Conclusion

The ultimate goal of this project was to observe the effect of incorporating Li doping on the ZnO nanowires and to study the performance of these doped nanowires as a nano-energy harvester and a nano-sensor material. Towards this purpose, one undoped and four Li-doped nanowire devices were fabricated with different concentrations of Li using hydrothermal growth technique. Extensive physical, material and piezoelectric characterizations as well as simulations were performed on the fabricated devices.

Increased Li concentration resulted in shorter NWs on the average for the same growth conditions and time, whereas the lateral size, the thickness of the NWs, did not show a clear pattern with doping concentration. The number of NWs per unit area increased with Li doping again, for the same growth conditions.

The vertical lattice constant of the nanowires decreased with higher Li doping concentration, which is a clear indication that most of the Li atoms are substituting Zn atoms in the ZnO crystal structure since  $\text{Li}^+$  is smaller than  $\text{Zn}^{2+}$ . Moreover, the red shift in the E2-high Raman active vibrational mode, associated with the O atoms, also verified that most of the Li atoms are occupying substitutional sites.

We found that the force-normalized measured voltage, i.e. sensitivity, generated by the ZnO NWs when bent with an AFM tip improved 22-fold with Li doping, as a combination of both improvement in the piezoelectric effect and the aforementioned size changes. Simulation results disclosed that when the size changes are removed, the effective improvement in the sensitivity is reduced to 7-fold. We suspect that the kick-out diffusion mechanism of Li in ZnO plays a major factor behind this piezoelectric sensitivity improvement. This kick-out mechanism can lead to a reduced electron screening effect in the intrinsically n-type ZnO nanowires. In addition, due to the reduction of the lattice constant with doping, the ZnO nanowire structure gains more anisotropy, thus improving the piezoelectric response. There is, however, an optimum point of Li doping concentration that can provide the maximum piezoelectric response. This dissertation can, therefore, serve as a guideline for the optimization of the future nano-sensors and nano-energy harvesters based on ZnO nanowires.

# **Chapter 3 : MEMS Scale Triboelectric Energy Harvester with High Operating Frequency and Wide Bandwidth**

## **3.1. Introduction**

This chapter presents the design, optimization, fabrication, and characterization of a MEMS scale TEH with a high target operating frequency (1150 Hz) and wide frequency bandwidth (920 Hz). Even though high target operating frequency is prevalent for electrostatic and piezoelectric energy harvesters, rarely any triboelectric energy harvester is designed for such high-frequency operations. Al and Teflon have been used as the triboelectric pair based on the large difference between their tendency to lose or gain electrons in the triboelectric series and their compatibility with common MEMS fabrication processes [97]. Detailed modeling and optimization for a coupled electromechanical system have been discussed. The effective volume of the presented TEH is much smaller compared to the traditional triboelectric energy harvester designs available in the literature. Novel fabrication approaches such as the use of spin-coated Teflon AF and selective ashing of a thick sacrificial polyimide layer in high pressure O<sub>2</sub> plasma have been adopted. UV-LIGA (Ultra-Violet Lithographie, Galvanoformung, Abformung) has been modified to achieve a relatively thick MEMS proof-mass. Although such scaling and fabrication approaches are previously reported for electrostatic and piezoelectric energy harvesters, they have not been implemented on triboelectric energy harvesters due to their inherent requirement of a frictional contact between the triboelectric materials.

Outcomes of this chapter have been reported in the 2019 IEEE Sensors Application Symposium [165] and Sensors and Actuators A: Physical Journal [166].



## 3.2. Design and modeling of the triboelectric energy harvester

### 3.2.1. Modeling of the triboelectric energy harvester

Motivated by the high charge pumping efficiency and structural robustness, the TEH is designed and modeled using the vertical contact separation mode [99], [111]. The structural assembly schematic is presented in Fig. 3.1. The TEH consists of a bottom triboelectric layer (Teflon) and a top triboelectric layer (Al). An air gap  $h(t)$  separates these two triboelectric layers. A bottom electrode is stacked underneath the Teflon layer to complete the assembly. The bottom electrode and the top triboelectric Al layers are electrically connected through a load. The thickness of the bottom and top triboelectric layers are denoted as  $d_2$  and  $H_{ml}$ , respectively. The lateral dimensions for both of the triboelectric layers are the same and denoted as  $l_{pm}$  and  $w_{pm}$ , respectively.

A spring with a spring constant  $k_z$  is used to suspend the top triboelectric layer. As a result, when the total system is exposed to a perpendicular external vibration, the top triboelectric Al layer changes its location with respect to its initial position. This results in the change of the air gap between the triboelectric layers. The initial air gap is defined as  $x_0$ . At any time  $t$ , if the displacement of the top triboelectric layer is  $z(t)$  from its initial position, the air gap  $h(t)$  at that time is  $h(t) = x_0 + z(t)$  (Fig. 3.1). For modeling purposes, the upward direction is considered as positive and the downward direction is considered as the negative direction. At a sufficiently high magnitude of external vibration,  $z(t)$  in the downward direction becomes equal to  $x_0$ , resulting in a zero air gap where the triboelectric layers contact each other. As a result, the triboelectric charge is generated between them due to the friction. At the next vibration cycle, the triboelectric layers start to separate. If the external vibration is periodic, this contact and separation cycle is also periodic. Because the top metal triboelectric layer is connected with the bottom electrode through a load resistance  $R$ , the periodic contact and separation cycle results in a periodic charge flow

through the load, leading to an AC output. The frequency of the vibration and the triboelectric charge density are denoted as  $f$  and  $\sigma$ , respectively.

The equivalent circuit model for the TEH system is depicted in the inset of Fig. 3.1. Two types of capacitances are present in the system. The first one is a fixed capacitance  $C_{device}$  between the bottom electrode and the bottom triboelectric layer. The second one is a variable capacitance  $C_{air}$  between the two triboelectric layers. In addition, there is also a parasitic capacitance  $C_{par}$  which is not considered in the model.

If we apply a periodic excitation into the system, the voltage  $V$  across the load at any time  $t$  is defined as [167]:

$$V = R \frac{dQ}{dt} = -\frac{Q}{S_{eff} \epsilon_0} \left( \frac{d_2}{\epsilon_{r2}} + h(t) \right) + \frac{\sigma h(t)}{\epsilon_0} = -\frac{Q}{S_{eff} \epsilon_0} \left( \frac{d_2}{\epsilon_{r2}} + x_0 + z(t) \right) + \frac{\sigma (x_0 + z(t))}{\epsilon_0} \quad (3.1)$$

where  $Q$  denotes the transferred charge,  $S_{eff}$  the effective triboelectric contact area,  $\epsilon_0$  the vacuum permittivity and  $\epsilon_{r2}$  is the relative permittivity of the bottom triboelectric Teflon layer.

From Eq. 3.1, the open circuit voltage  $V_{oc}$  and the short circuit current  $I_{sc}$  of the TEH is calculated as

$$V_{oc} = \frac{\sigma h(t)}{\epsilon_0} \quad (3.2)$$

$$I_{sc} = \frac{S_{eff} \sigma d_2 v(t) \epsilon_{r2}}{(d_2 + \epsilon_{r2} h(t))^2} \quad (3.3)$$

where,  $v(t)$  is the velocity of the top triboelectric layer due to the external vibration.

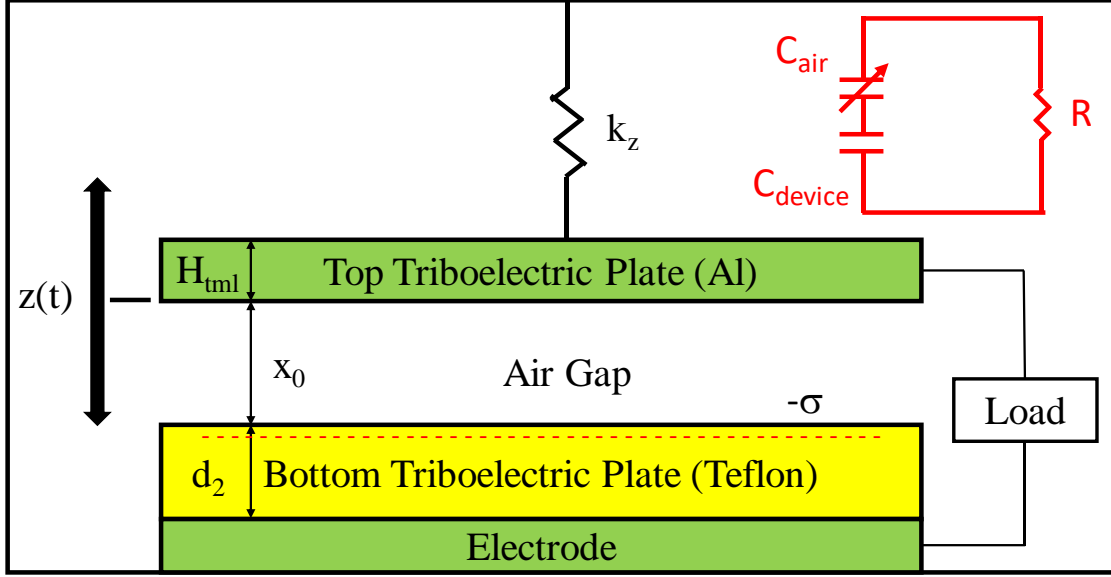


Figure 3.1: Schematic of the TEH for vertical contact separation mode operation. The equivalent circuit of the system is depicted in the inset.

To increase the mass of the movable part, a proof-mass with thickness  $H_{pm}$  is included on top of the triboelectric layer. Ni is chosen as the proof-mass metal considering its high density and fabrication ease. The thickness of the suspended assembly is  $H = H_{pm} + H_{tml}$  and the mass is  $m$ . Therefore, when the system in Fig. 3.1 is exposed to a periodic acceleration  $a(t)$ , the mechanical model of the system is similar to a mass-spring-damper system [168]. Hence, the dynamic expression for the mechanical system is

$$m \frac{d^2 z(t)}{dt^2} = ma(t) - mg + F_s + F_d + F_e \quad (3.4)$$

Here,  $g$  denotes gravitational acceleration ( $9.81 \text{ ms}^{-2}$ ),  $F_s$  is the force applied by the spring on the suspended structure,  $F_e$  is the electrostatic force between the triboelectric layers and  $F_d$  is the squeeze film damping force. The spring force is determined from the spring constant whereas the electrostatic force is calculated from the electrostatic energy  $U$  of the system.

$$F_s = -k_z z(t) \quad (3.5)$$

$$U = \frac{1}{2} QV = \frac{Q}{2} \left[ -\frac{Q}{S_{eff} \epsilon_0} \left( \frac{d_2}{\epsilon_{r2}} + h(t) \right) + \frac{\sigma h(t)}{\epsilon_0} \right] \quad (3.6)$$

$$F_e = -\frac{dU}{dh} = \frac{Q^2}{2S_{eff} \epsilon_0} - \frac{Q\sigma}{2\epsilon_0} \quad (3.7)$$

Reducing the squeeze film damping force is one of the fundamental issues to ensure the highest displacement of the suspended structure and a good contact force between the triboelectric layers. For this reason, perforations have been introduced at the suspended structure. Perforations also make it easier to etch the sacrificial layer underneath the suspended structure. The radius of a single perforation and a unit cell are defined as  $r_0$  and  $r_c$ , respectively. The squeeze film damping force  $F_d$  is then modeled considering the rarefaction effect [121].

$$F_d = \Re l^2 w_{pm} l_{pm} \frac{\gamma}{3\alpha^2} \quad (3.8)$$

where,  $\alpha$ ,  $\gamma$ ,  $\Re$  and  $l$  are defined as

$$\alpha = \frac{2}{w_{pm}} \sqrt{\frac{2(x_0 + z(t))^3 H_{eff} \eta(\beta)}{3\beta^2 r_0^2}} \quad (3.9)$$

$$\gamma = \gamma(\alpha, \kappa) = 3\alpha^2 - 6\alpha^3 \frac{\sinh^2 \frac{1}{\alpha}}{\sinh \frac{2}{\alpha}} - \frac{24\alpha^3 \kappa}{\pi^2} \sum_{n=1,3,5,\dots}^{\infty} \frac{\tanh \sqrt{1 + \left(\frac{n\pi\alpha}{2}\right)^2}}{n^2 \left(1 + \left(\frac{n\pi\alpha}{2}\right)^2\right)^{\frac{3}{2}}} \quad (3.10)$$

$$\Re = -\frac{12\mu_{eff}}{(x_0 + z(t))^3} \frac{dz(t)}{dt} \quad (3.11)$$

$$l = \sqrt{\frac{2h^3 H_{eff} \eta(\beta)}{3\beta^2 r_0^2}} \quad (3.12)$$

In addition,

$$\kappa = \frac{w_{pm}}{l_{pm}} \quad (3.13)$$

$$\beta = \frac{r_0}{r_c} \quad (3.14)$$

$$\eta(\beta) = \left( 1 + \frac{3r_0^4 k(\beta)}{16H_{eff} (x_0 + z(t))^3} \right) \quad (3.15)$$

$$k(\beta) = 4\beta^2 - \beta^4 - 4\ln(\beta) - 3 \quad (3.16)$$

$$H_{eff} = H + \frac{3\pi r_0}{8} \quad (3.17)$$

$$\mu_{eff} = \frac{\mu}{1 + 9.658K_n^{1.159}} \quad (3.18)$$

$$K_n = \frac{\lambda}{x_0} = \frac{p_0 \lambda_0}{p_a x_0} \quad (3.19)$$

Here,  $\mu_{eff}$  and  $\mu$  are the coefficient of viscosity for air with and without considering the rarefaction effect, respectively.  $K_n$  is the Knudsen number,  $\lambda$  is the mean free path of gas molecules ( $\lambda_0 = 0.064 \mu\text{m}$ ),  $p_0$  is the atmospheric pressure and  $p_a$  is the ambient pressure.

Finally, if the total number of perforations on the suspended plate is defined as  $N$ , then the effective triboelectric contact area  $S_{eff}$  is defined as:

$$S_{eff} = (l_{pm} \times w_{pm}) - (N \times \pi \times r_0^2) \quad (3.20)$$

Based on the expressions discussed, the overall electromechanical system is summarized by the subsequent coupled dynamic expressions:

$$R \frac{dQ}{dt} = -\frac{Q}{S_{eff} \epsilon_0} \left( \frac{d_2}{\epsilon_{r2}} + x_0 + z(t) \right) + \frac{\sigma(x_0 + z(t))}{\epsilon_0} \quad (3.21)$$

$$m \frac{d^2 z(t)}{dt^2} = ma(t) - mg - k_z z(t) + F_d + \frac{Q^2}{2S_{eff} \epsilon_0} - \frac{\sigma Q}{2\epsilon_0} \quad (3.22)$$

### 3.2.2. Optimization of the triboelectric energy harvester

The TEH structural parameters are optimized to achieve maximum volumetric average power density. The coupled dynamic equations of the system (Eqs. 3.21 and 3.22) are solved numerically using the Matlab™ software. At the very beginning, the realistically achievable fabrication ranges for each of the independent variables present in Eqs. 3.21 and 3.22 are defined (Table 3.1) and a design of experiments (DOE) procedure is created. For instance, the proof-mass thickness  $H_{pm}$  range was selected from 1  $\mu\text{m}$  to 18  $\mu\text{m}$ . 18  $\mu\text{m}$  is set as the maximum because of the processing limit of the NR2-8000P mold layer. Subsequently, a Matlab™ code is developed to numerically solve the coupled dynamic equations. For each set of values for the independent variables in Table 3.1, the equations have only two unknown variables: the transferred charge  $Q$  and the suspended assembly displacement from its initial position  $z(t)$ . The Matlab™ code then solves the equations for those two variables using its ode15s solver [169]. Once the values of  $Q$  and  $z(t)$  are known, the output voltage  $V$  across the load at any time  $t$  is calculated using Eq. 3.1. Instantaneous power  $P_I = V^2/R$  is then computed. Finally, the average power  $P_{avg}$  is calculated using the following expression:

$$P_{avg} = \frac{1}{t_2 - t_1} \int_{t_1}^{t_2} P_I dt \quad (3.22)$$

The corresponding volumetric average power density is also determined. The values for all the variables are saved.

In the same procedure, the Matlab™ code sweeps all the independent variables and saves the  $P_{avg}$  and volumetric average power density corresponding to that set of variables. Finally, after all sets of combinations are solved, the code determines the maximum value of the volumetric average power density. This way, the system was optimized for maximum volumetric average power density. The values for the optimized parameters and corresponding remarks are presented in the last two columns of Table 3.1.

The TEH is designed to have its resonance frequency at 800 Hz based on the primary vibration mode of an aircraft skin [8]. The triboelectric charge density between the Teflon - Al pair is taken as  $10 \mu\text{Cm}^{-2}$  [113], [125]. The optimized parameter list for the system is presented in Table 3.1. For 1g input acceleration, the optimum operating condition is found at 800 Hz frequency and 10 MΩ load resistance (Fig. 3.2)). At this condition, the TEH can generate 66.02 nW average power and 278 nW peak power. The response of the system at the optimum condition is depicted in Fig. 3.3.

Table 3.1: Summary of the structurally optimized parameters for the triboelectric energy harvester

Parameter	Range for Optimization	Design	Remarks
Proof-mass and top triboelectric layer length ( $l_{pm}$ )	50 $\mu\text{m}$ to 5000 $\mu\text{m}$	5000 $\mu\text{m}$	Optimized based on proof-mass length preset limit
Proof-mass and top triboelectric layer width ( $w_{pm}$ )	50 $\mu\text{m}$ to 5000 $\mu\text{m}$	3000 $\mu\text{m}$	Optimized
Proof-mass thickness ( $H_{pm}$ )	1 $\mu\text{m}$ to 18 $\mu\text{m}$	10 $\mu\text{m}$	Optimized
Top triboelectric Al layer thickness ( $H_{ml}$ )		150 nm	Value was preset
Initial gap between the triboelectric layers ( $x_0$ )	1 $\mu\text{m}$ to 14 $\mu\text{m}$	14 $\mu\text{m}$	Optimized based on cured HD4110 processing condition limit
Bottom triboelectric Teflon layer thickness ( $d_2$ )	1 $\mu\text{m}$ to 5 $\mu\text{m}$	5 $\mu\text{m}$	Optimized based on Teflon AF 1601 (6%) processing limit with 4 layers of coating
Perforation radius of the top triboelectric layer and proof-mass ( $r_0$ )	1 $\mu\text{m}$ to 100 $\mu\text{m}$	18 $\mu\text{m}$	Optimized
Unit cell radius of the top triboelectric layer and proof-mass ( $r_c$ )	1.1 $r_0$ to 5 $r_0$	27 $\mu\text{m}$	Optimized
Spring constant ( $k_z$ )		22.37 $\text{Nm}^{-1}$	Optimized (dependent variable on vibration frequency $f$ and mass of the proof-mass $m$ )
Load resistance ( $R$ )	100 $\Omega$ to 1 $\text{G}\Omega$	10 $\text{M}\Omega$	Optimized



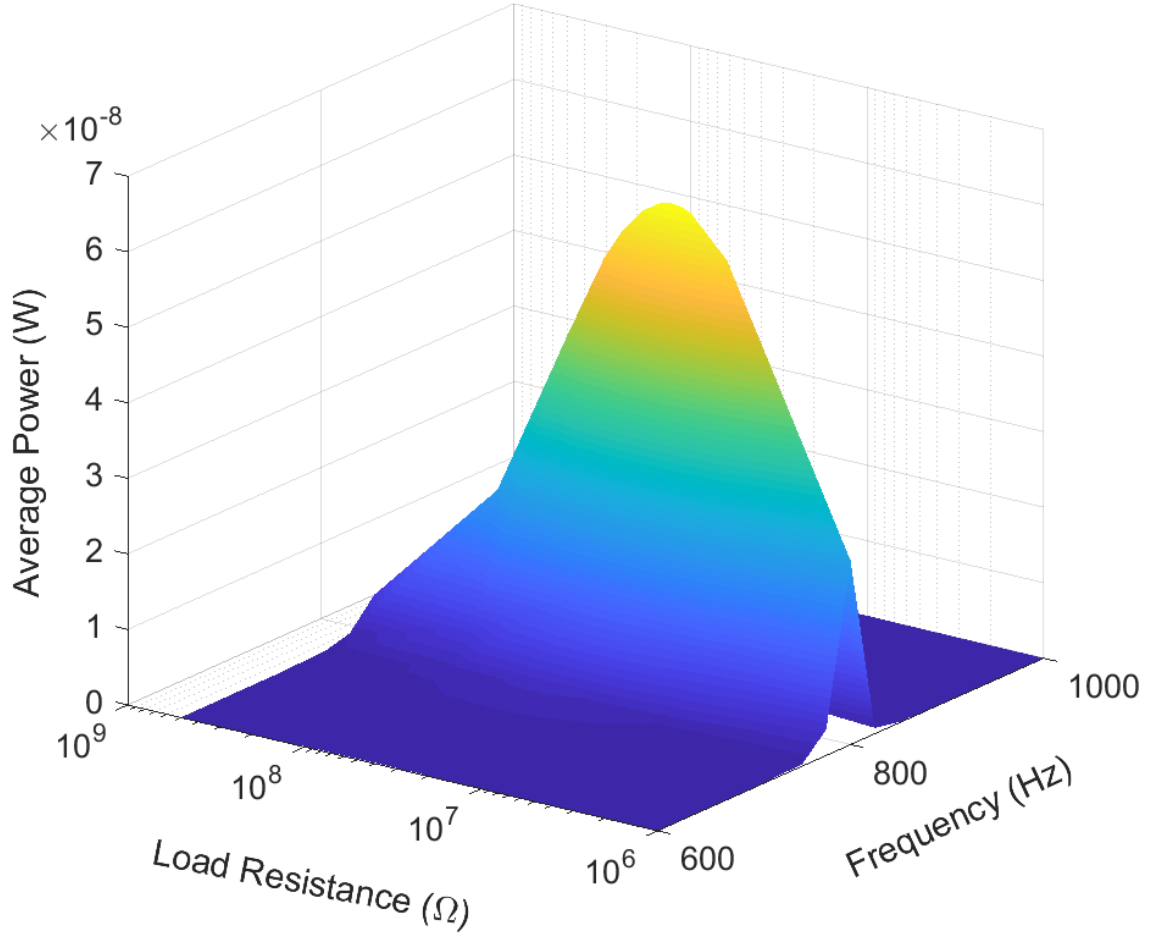


Figure 3.2: Frequency and load resistance sweep to determine the optimum operating condition in terms of average power. The optimum condition is found to be at 800 Hz frequency and 10 M $\Omega$  load resistance.

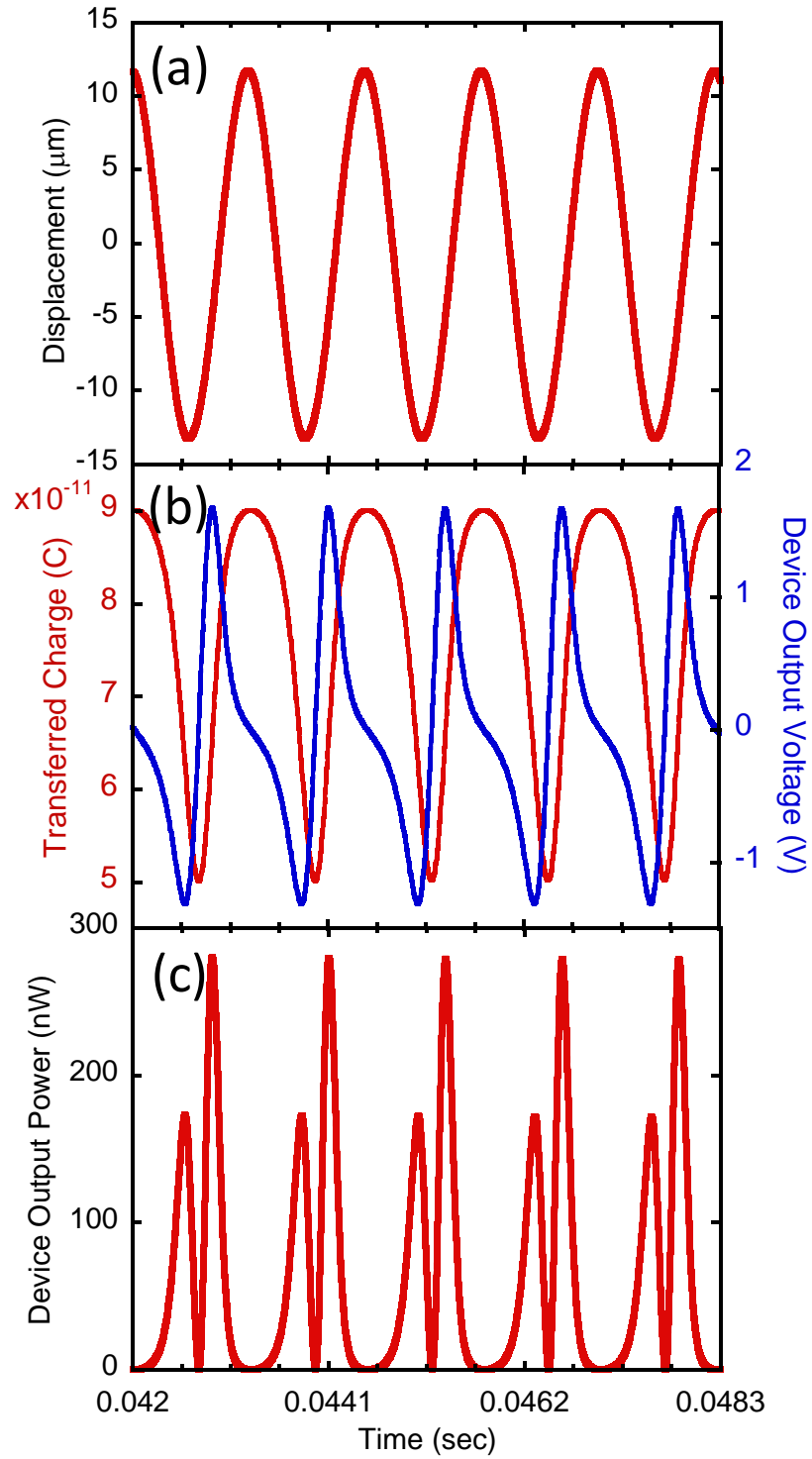


Figure 3.3: TEH system response at the optimum simulated operating condition of 800 Hz frequency and 10 M $\Omega$  load resistance. (a) Displacement of the suspended structure. (b) Transferred charge and device output voltage profile. (c) Device output power profile.

### 3.2.3. Triboelectric energy harvester structure and spring design

Based on the optimized parameters discussed in Table 3.1, a Coventorware™ model has been created for MemMech simulation to predict the physical behavior of the TEH. The TEH structure is presented in Fig. 3.4. The perforations on the suspended structure are approximated as a square rather than a circle for simplicity. To achieve the optimized spring constant value as specified in Table 3.1, eight serpentine springs, connected in parallel, have been incorporated into the system. The spring dimensions are described in Table 3.2. The modal harmonic analysis was performed on a quarter of the full structure to observe the vibration modes of the system. The primary vibration mode, which is the vertical movement of the proof-mass, is found to be at 796 Hz as depicted in Fig. 3.5(a). At the operating frequency range, all the other vibration modes are more than 3 orders of magnitude smaller than the primary vibration mode. Generalized displacement at the primary vibration mode from the design is presented in Fig. 3.5(b). Spring designs with fixed beam, u-shape, crab leg and folded beam structures were also tried [170]. However, the serpentine design provided the best result in terms of mode separation.

Table 3.2: Serpentine spring parameters

Spring Parameters	Design
Total springs connected in parallel	8
Spring width ( $\mu\text{m}$ )	20
Spring thickness ( $\mu\text{m}$ )	10
Primary length of the serpentine spring ( $\mu\text{m}$ )	750
Secondary length of the serpentine spring ( $\mu\text{m}$ )	100
Primary vibration mode frequency of the modal harmonic analysis (Hz)	796

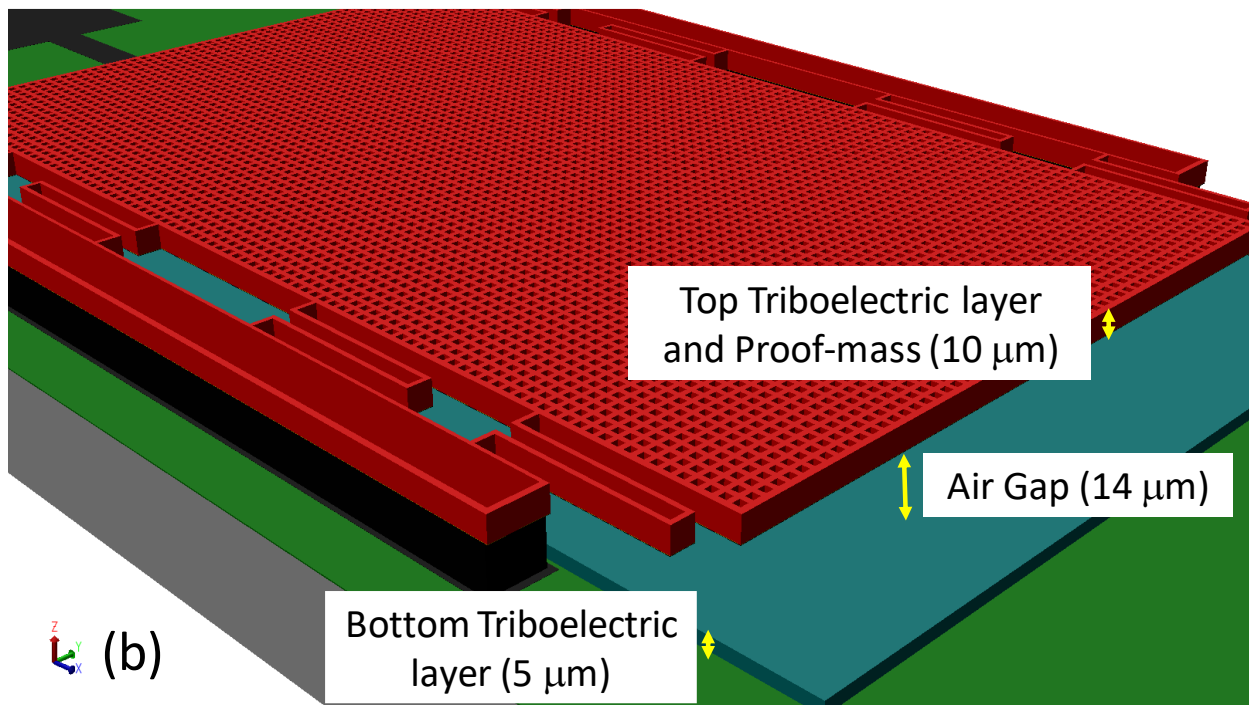
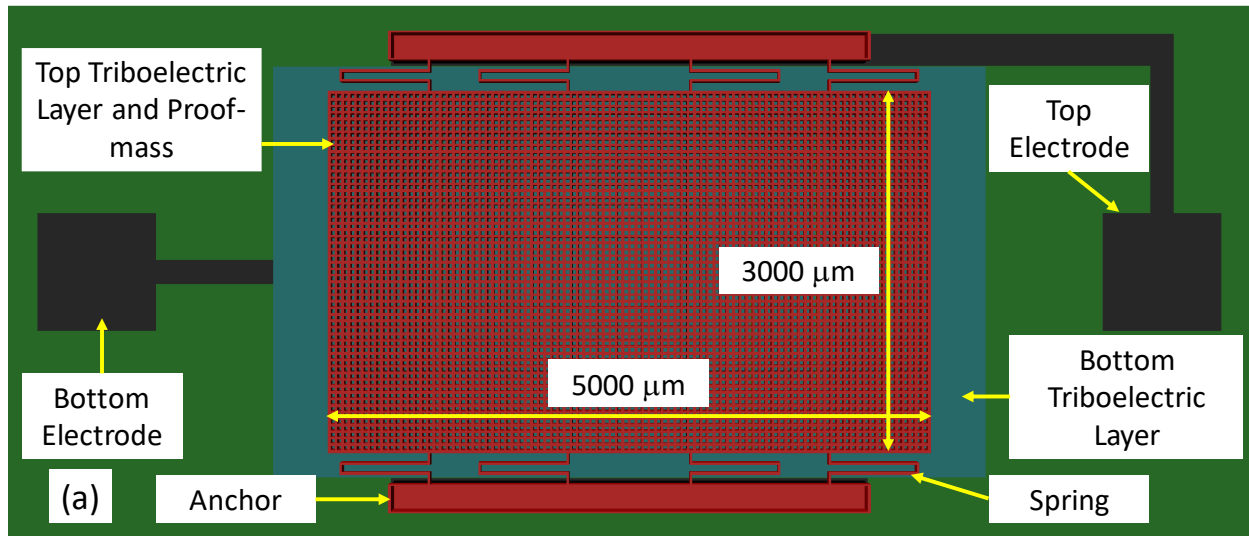


Figure 3.4: Structural model of the optimized triboelectric energy harvester. (a) Top view. (b) Tilted view.

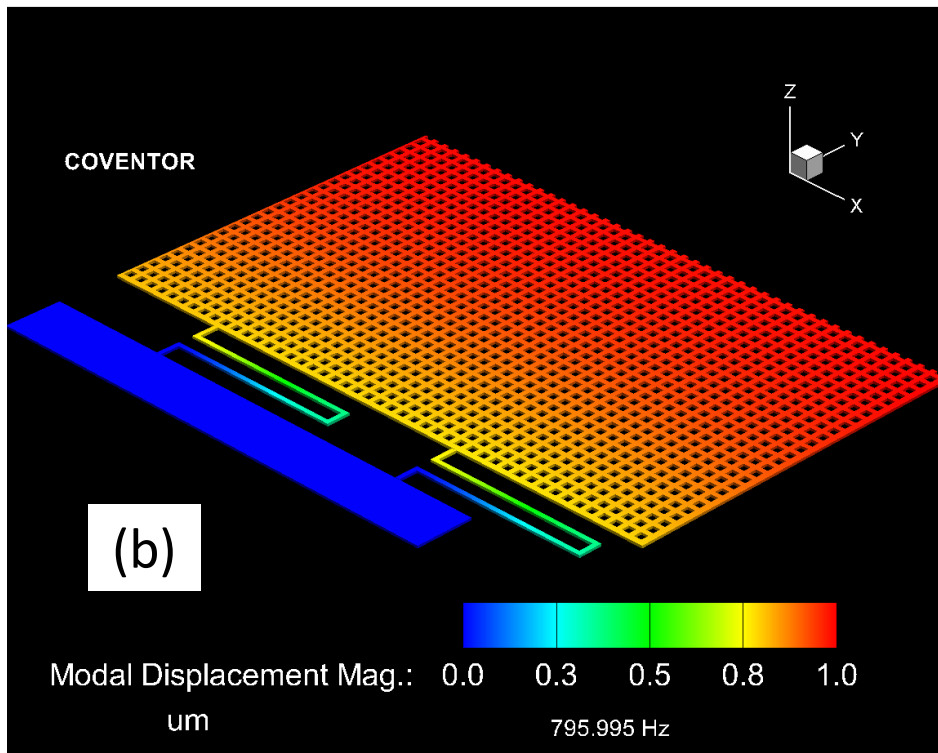
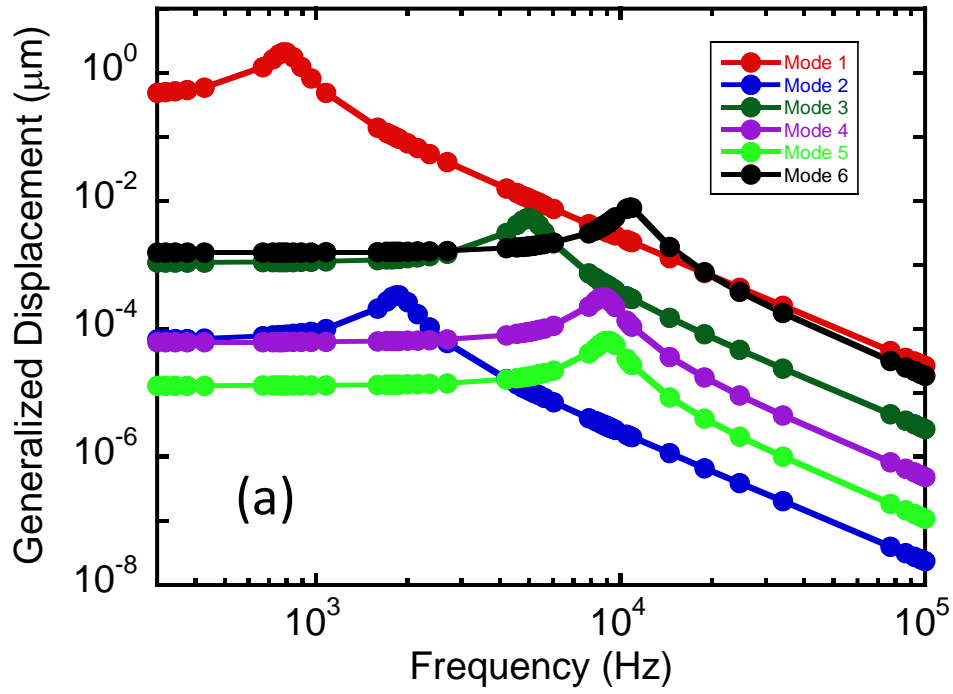


Figure 3.5: (a) Generalized displacement for the vibration modes of the triboelectric energy harvesting system obtained from the modal harmonic analysis. (b) Primary vibration mode (mode 1) of the system is a vertical motion.

### 3.2.4. Stress analysis

Stress analysis simulation is performed using MemMech solver of Coventorware™ to confirm the structural robustness of the design before fabrication. Although we planned the experimental input excitation to be less than 10g acceleration, the stress analysis is performed at 50g input acceleration for the worst possible case. At this high excitation, a maximum of 211 MPa von Mises stress is observed near the corners of the springs as depicted in Fig. 3.6. This analysis reveals that the edges of the springs are the most vulnerable area of the device if it is to suffer from fatigue or break down. As the simulation illustrates, even at 50g acceleration, the maximum von Mises stress on the springs (211 MPa) is still well under the yield strength of the spring constituent materials Au (~400 MPa), Al (~280 MPa) and Ni (~450 MPa) [171], [172], [173], [174].

Overall, the simulation of stress demonstrates the robustness of the structure before the start of the fabrication process.

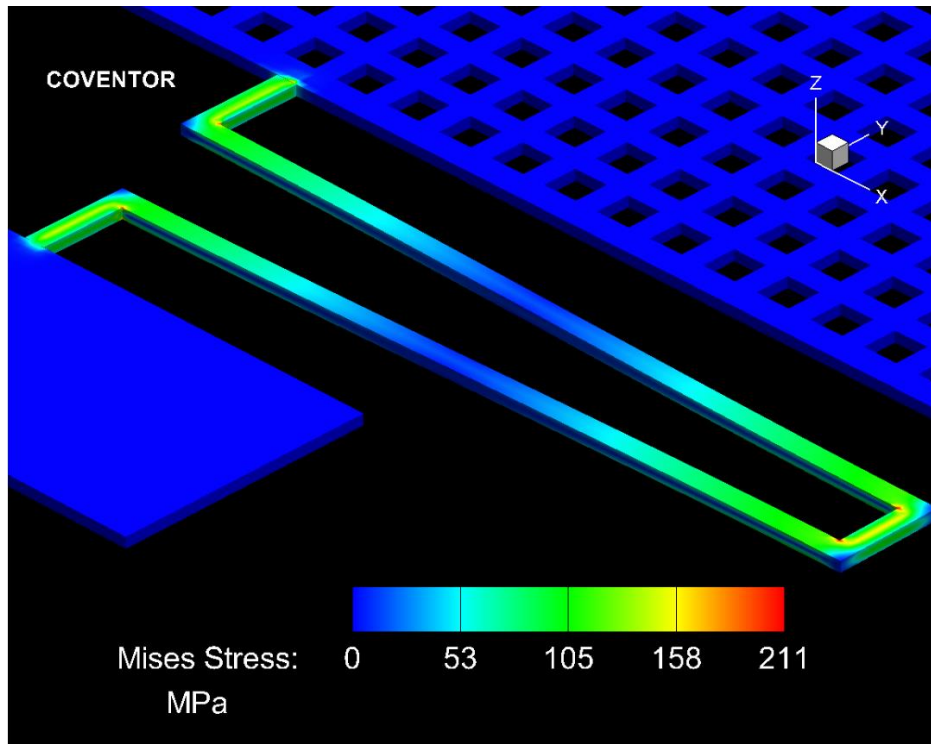


Figure 3.6: Stress analysis on the device model with 50g input acceleration. The maximum von Mises stress shown here at a close-up view is less than the yield strength of all materials, Au, Al and Ni.

### 3.2.5. Summary

Detailed device modeling, optimization, structure, and stress analysis is presented in this section. The dynamic model of the device is constructed considering the coupled electrical and mechanical systems. That model is then numerically solved to obtain optimum structural parameters for the device. With the optimized parameters, the device model is then recreated, and FEM analysis is performed to analyze the vibration modes as well as the stress analysis on the system.

### 3.3. Fabrication of the triboelectric energy harvester

The complete fabrication process flow is presented in Fig. 3.7. The fabrication started with the sputter deposition of 500 nm  $\text{Si}_3\text{N}_4$  insulation layer on top of a Si wafer (Fig. 3.7(a)). A 500 nm Al layer was then sputtered and patterned as the bottom electrode using the standard liftoff process with NR9-1500PY photoresist (Fig. 3.7(b)). Subsequently, Teflon AF 1601 (6%) was spin-coated to serve as the bottom triboelectric material. Teflon is hydrophobic and exhibits poor adhesion to underlying layers. Therefore, the wafer was spin-coated with 1H, 1H, 2H, 2H-perfluoro-decyltriethoxy silane as the adhesion promoter before the spin coating of Teflon AF. The spin coating was done at 3000 RPM for 20 seconds. The wafer was thoroughly rinsed with DI water after the spin coating and baked at  $110^\circ\text{C}$  for 12 minutes. Afterward, Teflon AF 1601 (6%) was spin-coated at 1000 RPM for 20 seconds. A two-step baking procedure was performed thereafter, the first step for 5 minutes at  $112^\circ\text{C}$  and the second step for 15 minutes at  $180^\circ\text{C}$ . The above procedure was repeated three more times to achieve the target thickness of 5  $\mu\text{m}$ . A final baking step for 30 minutes at  $330^\circ\text{C}$  ensured the uniformity of the Teflon layer and improved the adhesion with the layer underneath [175], [176].

The Teflon layer was patterned using reactive ion etching (RIE) in Ar plasma with PR1-1000A1 photoresist as the etch mask (Fig. 3.7(c)). Teflon surface was treated in Ar plasma for 5 seconds at 750 W power to increase its water wettability before the photoresist patterning. The selective etching of Teflon

was then conducted at 300 W power in RIE. To reduce the stress and heat sustained by the photoresist during the RIE process, the etch was conducted in 2 minute intervals with a one minute cool down in between. The etching took a total of 40 minutes to complete. The completion of the etching was verified with EDS analysis. The photoresist mask was then removed in Microposit 1165 resist remover.

In the subsequent step, the Teflon surface was again treated in Ar plasma for 5 seconds at 750 W power to improve its water wettability before the spin coating of HD4110, a photo definable polyimide, which acted as a sacrificial layer for the TEH. The polyimide was then patterned to create anchor openings for the suspended top triboelectric layer and proof-mass. The polyimide was cured at two steps in a programmable oven, first step at 200<sup>0</sup> C for 30 minutes and the second step at 365<sup>0</sup> C for 1 hour to achieve a target thickness of 14  $\mu\text{m}$ . (Fig. 3.7(d)). Next, a 150 nm Al layer was sputter-deposited as the top triboelectric layer (Fig. 3.7(e)).

A UV-LIGA process described elsewhere [177] was followed to form the proof-mass, springs, and the anchors. After e-beam evaporation of a 2 nm-thick Cr adhesion layer and a 100 nm-thick Au seed layer (Fig. 3.7(f)), a NR2-8000P photoresist mold was spin-coated and patterned to create openings for the subsequent Ni layer. (Fig. 3.7(g)). The thickness of the NR2-8000P mold layer was around 18  $\mu\text{m}$ . Cooldown steps of 15 minutes were added after the pre-bake and post-exposure bake to avoid any cracking on the thick NR2-8000P photoresist mold layer. Ni was then electroplated on the openings to a nominal thickness of 10  $\mu\text{m}$  to create the proof-mass, springs, and the anchors. The Ni electroplating was conducted in a nickel sulphamate ( $\text{Ni}(\text{SO}_3\text{NH}_2)_2$ ) solution at 45<sup>0</sup> C and 15 mA/cm<sup>2</sup> current density for 100 minutes. The mold layer was removed (Fig. 3.7 (h)) in Microposit 1165 resist remover, followed by the Ar plasma etching of the exposed top triboelectric Al and the Au seed layers in RIE (Fig. 3.7 (i)). The removal of the Al and Au layers were again verified using EDS analysis.

Finally, the proof-mass and the top triboelectric layer were suspended by oxygen plasma ashing of the sacrificial HD4110 (Fig. 3.7 (j)). The ashing was conducted at a relatively high pressure of 1.3 mbar to ensure the selectivity of polyimide to Teflon etching. Teflon is resistant to chemical etching. In contrast, it



is susceptible to physical ion bombardment. Increasing the plasma pressure reduces the mean free path of the ions. This ensures the low ion bombardment energy of the O<sub>2</sub> plasma for a selective HD4110 polyimide ashing. However, the high pressure in O<sub>2</sub> plasma also reduced the ashing rate of the polyimide. It took about 800 hours to completely ash the polyimide. For industrial manufacturing, unlike a single chamber asher we used here, a downstream plasma asher can be implemented for this polyimide ashing step where the wafer is placed downstream of the plasma in a separate chamber. In this way, the detrimental effects of direct plasma exposure are avoided such as the charging damage and the energetic ion bombardment damage [178]. The low-pressure plasma in those systems can dramatically increase the etch rate of the HD4110 polyimide without sacrificing its selectivity over Teflon etching.

Complete removal of the polyimide was ensured by EDS analysis (Fig. 3.8). A close-up SEM photo of one of the fabricated TEH structures is shown in Fig. 3.9. There are two major deviations from the design in the final fabricated TEH. The first one is the notching pattern on the bottom triboelectric layer coming from the ashing step. Because of the long ashing period, charging caused by plasma results in notching around the proof-mass side-walls. The second deviation is the bowing on the proof-mass due to the residual stress. This caused the center portion of the proof-mass to have a relatively higher air gap compared to the edge. The bowing effect is more clearly visualized in the Fig. 3.10.

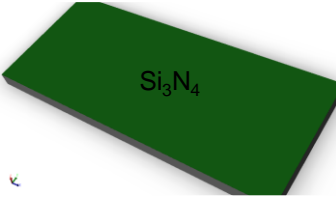
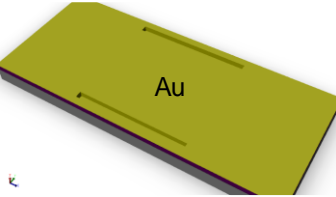
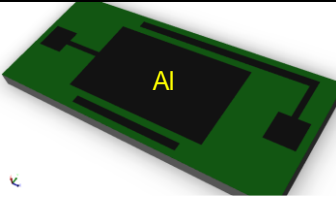
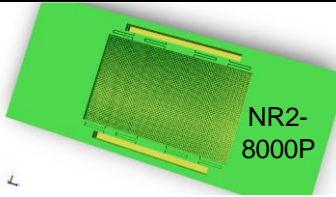
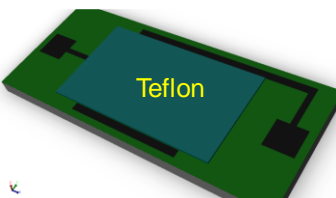
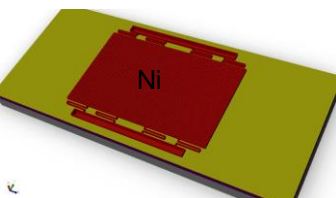

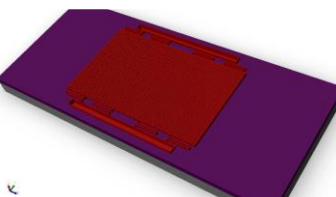
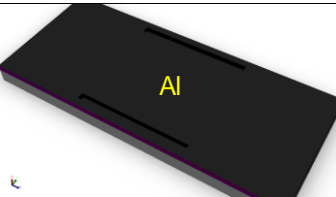
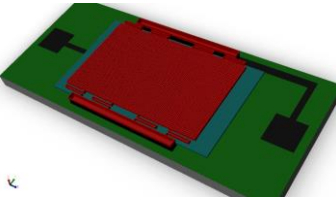
	<p>(a) Sputter deposition of 500 nm <math>\text{Si}_3\text{N}_4</math> on top of the Si wafer as the insulation layer.</p>		<p>(f) E-beam evaporation of 2 nm Cr as the adhesion layer and 100 nm Au as the seed layer for Ni electroplating.</p>
	<p>(b) Sputter deposition of 500 nm Al as the bottom electrode and patterning.</p>		<p>(g) NR2-8000P mold resist patterning for selective electroplating of Ni.</p>
	<p>(c) Spin coating of 5 <math>\mu\text{m}</math> Teflon AF as the bottom triboelectric layer and patterning in Ar plasma.</p>		<p>(h) Electroplating of 10 <math>\mu\text{m}</math> Ni and NR2-8000P mold resist removal.</p>
	<p>(d) Spin coating, patterning and curing of 14 <math>\mu\text{m}</math> HD4110 photo definable polyimide as the sacrificial layer.</p>		<p>(i) Dry etching of the electroplating seed layer and the top triboelectric layer in Ar plasma.</p>
	<p>(e) Sputter deposition of 150 nm Al as the top triboelectric layer</p>		<p>(j) Ashing of the HD4110 sacrificial polyimide in high pressure <math>\text{O}_2</math> plasma.</p>

Figure 3.7: Complete fabrication process flow of the triboelectric energy harvester

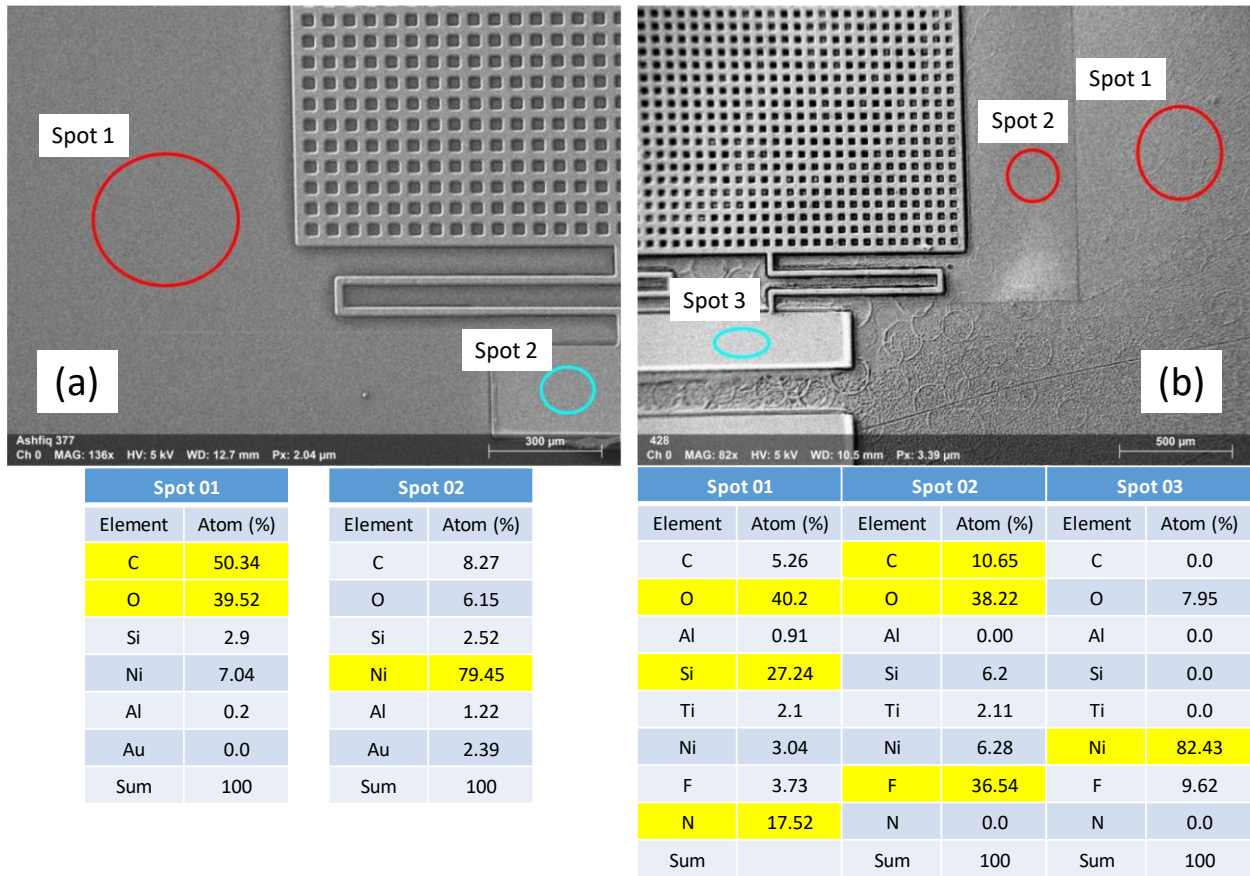


Figure 3.8: EDS analysis of the ashing of the HD4110 sacrificial polyimide. (a) Before the ashing of the HD4110 polyimide. Spot 1 shows the dominant presence of the C and O atoms which are the constituent atoms of the HD4110 polyimide. Spot 2 demonstrates the dominant presence of Ni which constitutes the anchor for the proof-mass. (b) After the completion of the HD4110 polyimide ashing. Spot 1 shows the dominant presence of the Si and N atoms which constitute the  $\text{Si}_3\text{N}_4$  passivation layer. The presence of O is also seen at spot 1 which possibly comes from the native oxidation. On the other hand, spot 2 demonstrates the dominant presence of C, O, and F atoms which constitute Teflon. The detection of  $\text{Si}_3\text{N}_4$  and Teflon verifies that the HD4110 polyimide ashing is complete. Finally, spot 3 demonstrates the presence of Ni anchor for the proof-mass.

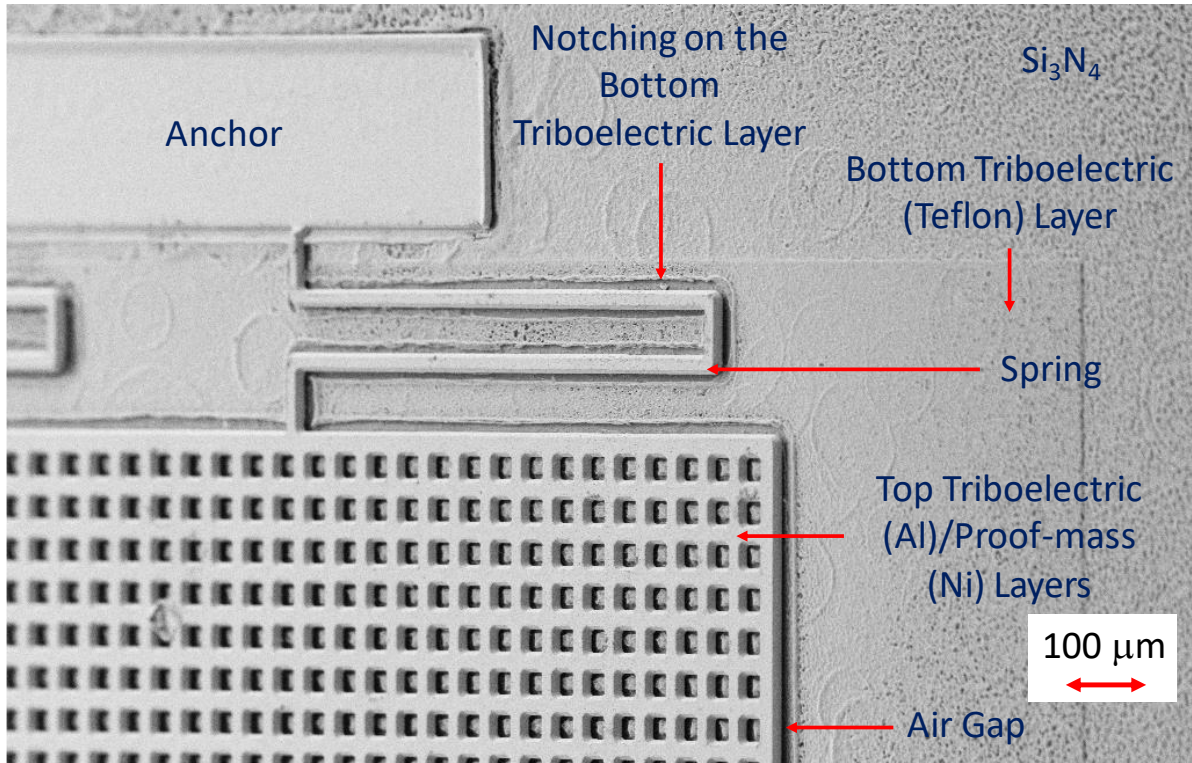


Figure 3.9: SEM image of a part of the triboelectric energy harvester. The stage was tilted at  $45^\circ$ .

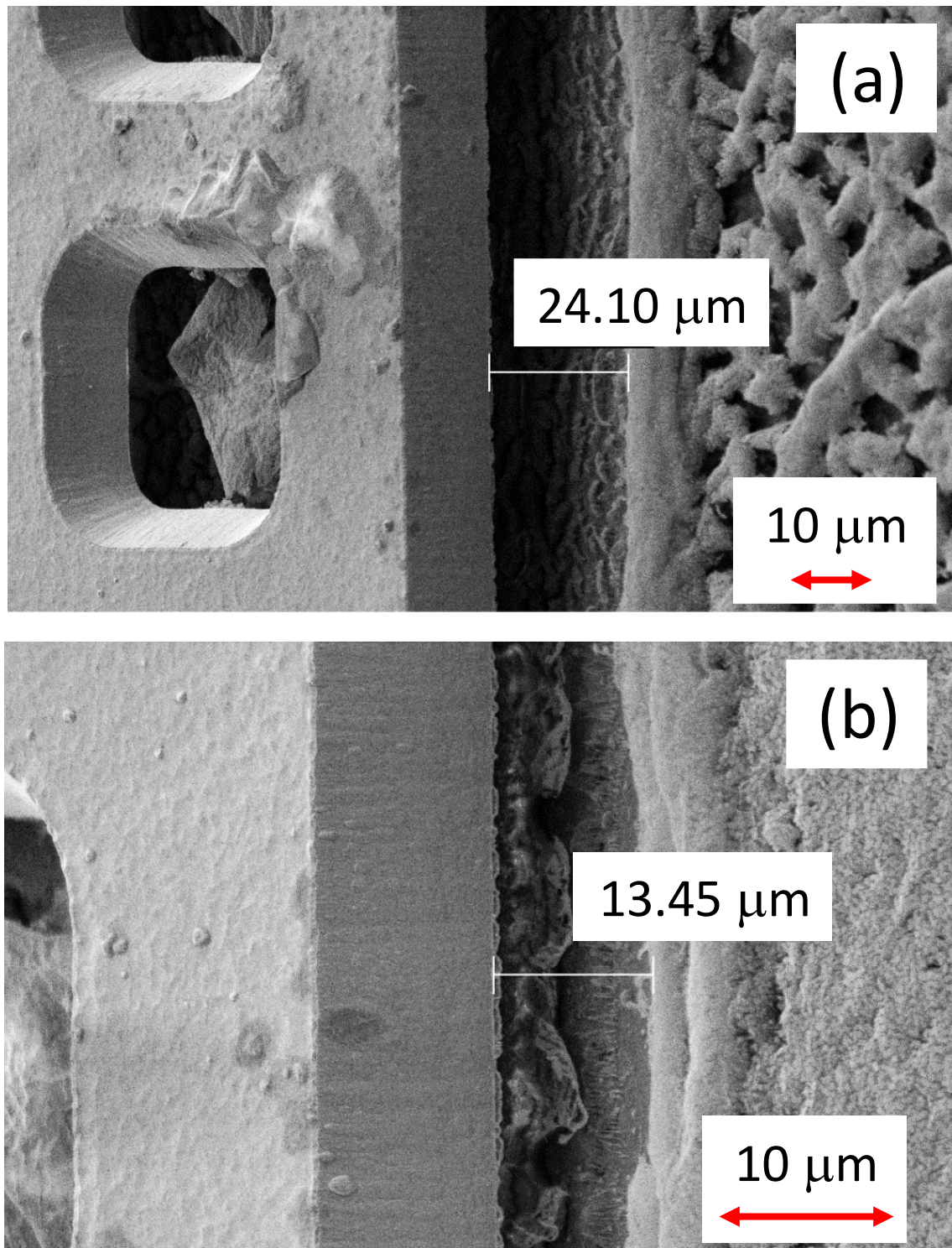


Figure 3.10: SEM images to observe the bowing of the proof-mass due to residual stress. The stage is tilted at  $45^\circ$ . (a) Near the center of the proof-mass. (b) Near the edge of the proof-mass

## **3.4. Characterization of the triboelectric energy harvester**

### **3.4.1. Characterization setup**

The packaged and wire-bonded TEH was attached to an ED-10 shaker as well as a calibrated SDI 2260-100 reference accelerometer with a sensitivity of  $20 \text{ mVg}^{-1}$ , frequency range of 2.5 kHz and acceleration range of  $\pm 100\text{g}$ . The shaker was then connected to LFG 1330S function generator through a Crown DSi 1000 power amplifier. A sinusoidal signal with a 6 V (p-p) amplitude was generated by the function generator. The power amplifier knob was turned by 4 turns to amplify the function generator signal before feeding it to the shaker. The TEH output was connected to SR 560 low noise preamplifier through a parallel load from a load resistance box. The SR 560 was used as a bandpass filter with cutoffs set at 300 Hz and 3 kHz to remove the line frequency and other unwanted disturbances. The output from the SR 560 was then fed into an oscilloscope to observe and record the output data. In addition, the reference accelerometer output was also connected to the oscilloscope for simultaneous measurement and recording of the external vibration acceleration and the corresponding output from the TEH. The block diagram of the characterization setup is depicted in Fig. 3.11.

### **3.4.2. Frequency response and load resistance optimization**

The TEH was shaken at different excitation frequencies varying from 400 Hz to 2000 Hz, with varying load resistance values for each frequency. The resulting 3D plot of average power per acceleration vs frequency and load resistance is shown in Fig. 3.12. The optimum operating condition is found at 1150 Hz frequency and 256 K $\Omega$  load resistance. Several other discrete peaks are also observed in the response. The contact between the triboelectric layers is most likely responsible for this as they introduce different vibration modes in the operating range. The input acceleration and the corresponding output voltage and power from the TEH at optimum operating condition are plotted in Figs. 3.13(a) – 3.13(b). The instantaneous acceleration varied from -9.33g to 9.33g. The system produces an average power of 179 nW

with peak power reaching up to 600 nW. Slight variation on the placement of the TEH device as well as the reference accelerometer on the ED-10 shaker causes a minor variation on the experimental output voltage (Fig. 13(a)). It is estimated that the percentage variation of the experimental output voltage because of this uncertainty is less than 5%. From Fig. 3.13(a), it is evident that there is an  $180^\circ$  phase shift between the input acceleration and the TEH output.

To calculate the sensitivity of the system, the phase shift was corrected as depicted in the Fig. 3.14. The phase-corrected TEH output voltage is plotted against the input acceleration in Fig. 3.15. Although the voltage response with respect to the acceleration is almost linear as expected [36], [179], the slope varies between 39 mV/g and 51 mV/g with an end to end nominal value of about 43 mV/g. Therefore, the TEH can be operated as an accelerometer with a nominal sensitivity of 43 mV/g.

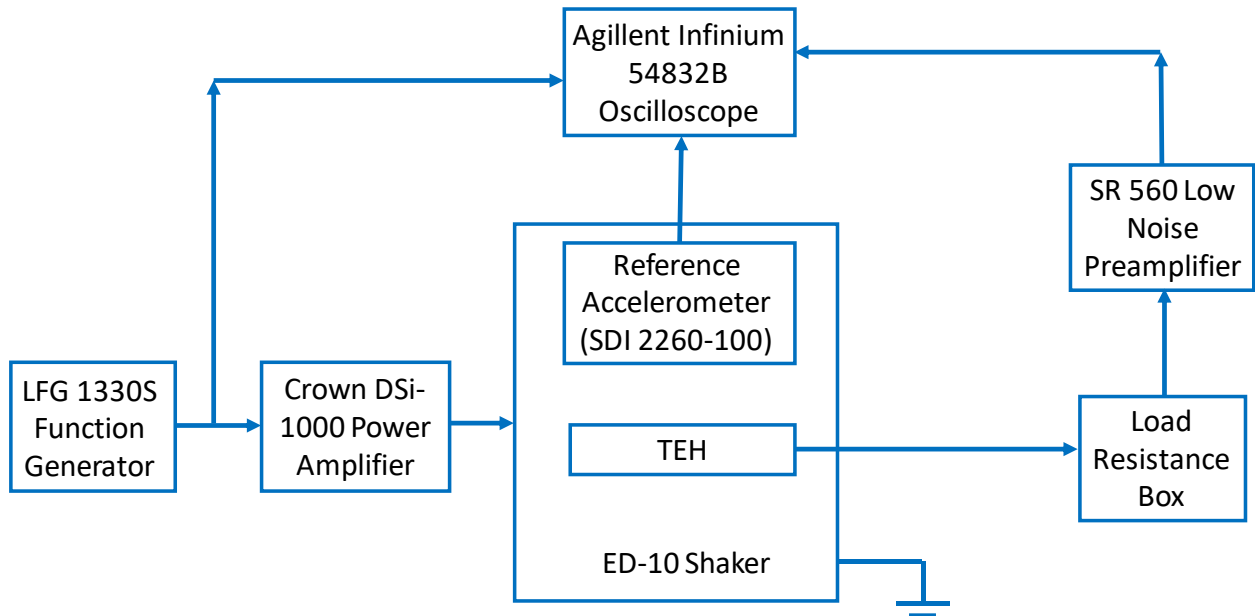


Figure 3.11: Block diagram of the characterization setup for the triboelectric energy harvesting system

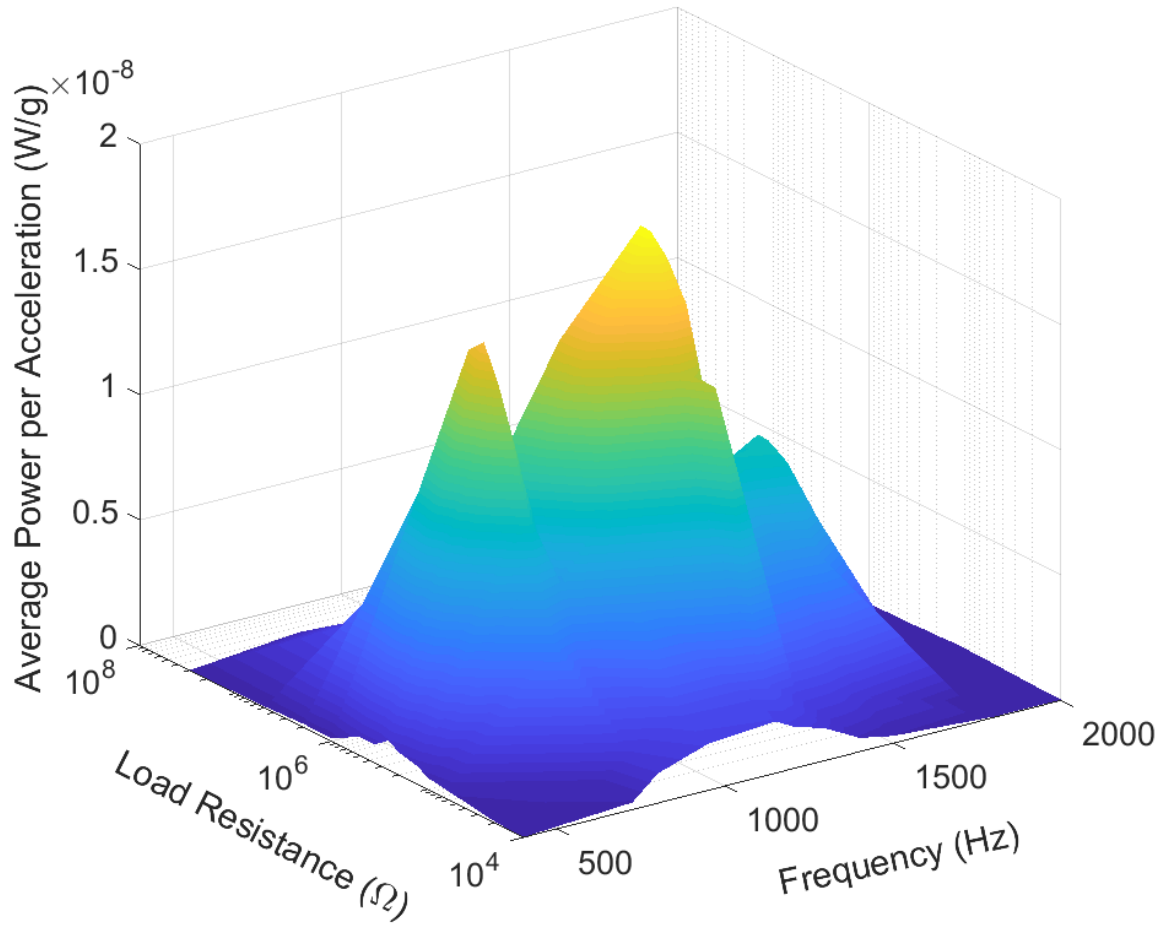


Figure 3.12: Load resistance and frequency sweep to determine the experimental optimum operating condition in terms of average power per acceleration. The experimental optimum condition is found at 1150 Hz frequency and 256 K $\Omega$  load resistance.



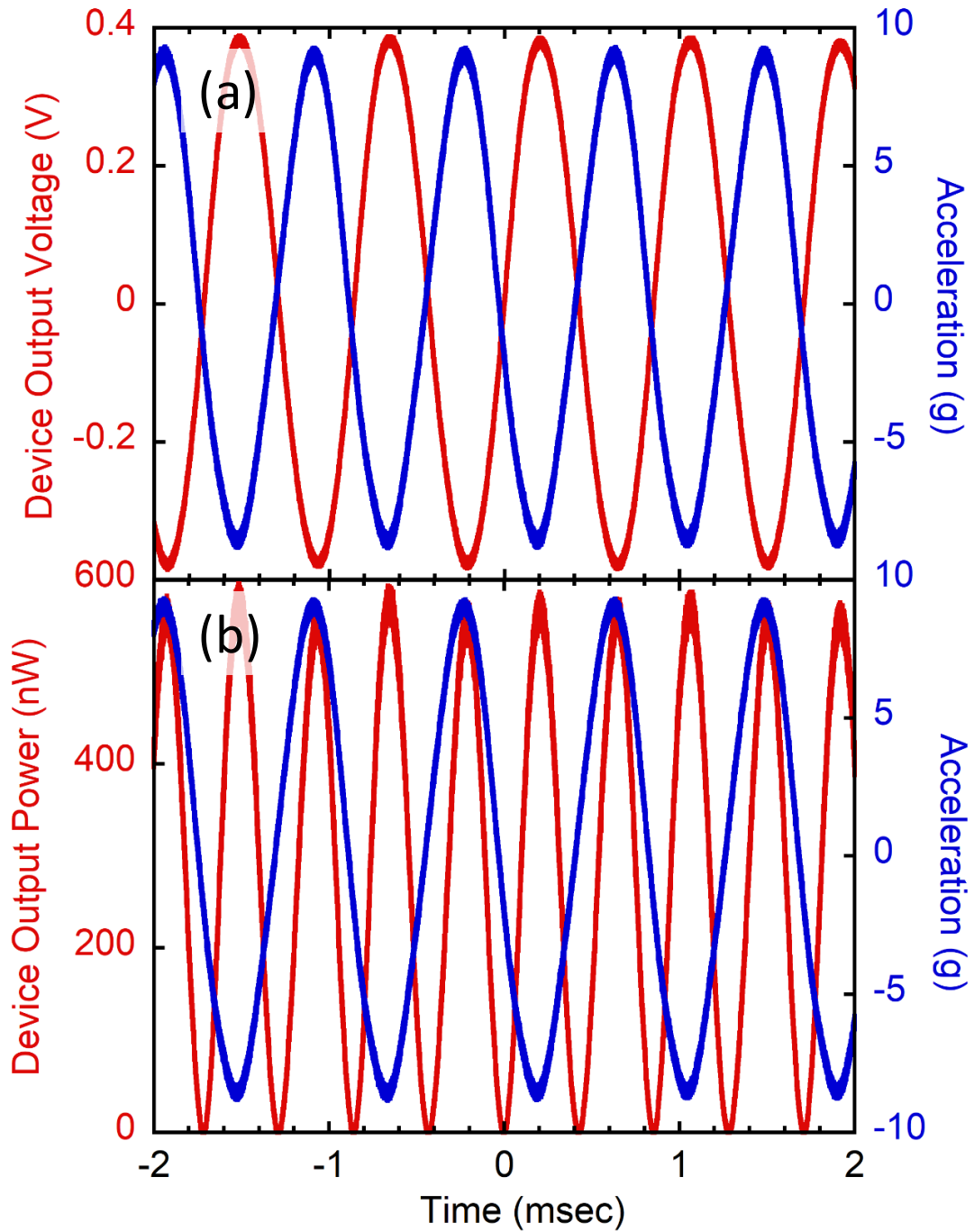


Figure 3.13: Response from the system at the experimental optimum operating condition. (a) Output voltage from the TEH corresponding to the input acceleration. (b) Output power from the TEH corresponding to the input acceleration.

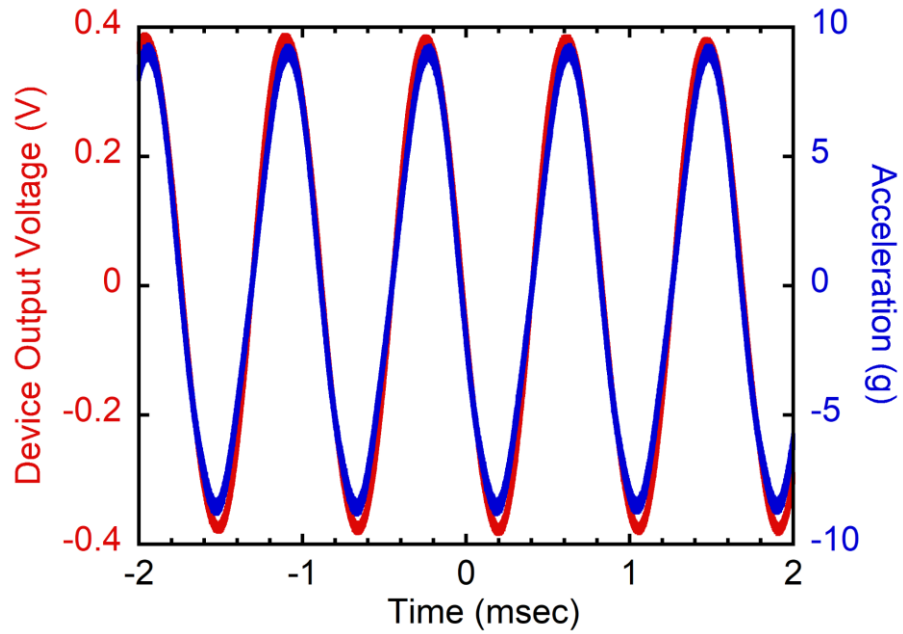


Figure 3.14: The phase-corrected output response from the characterization of the triboelectric energy harvester.

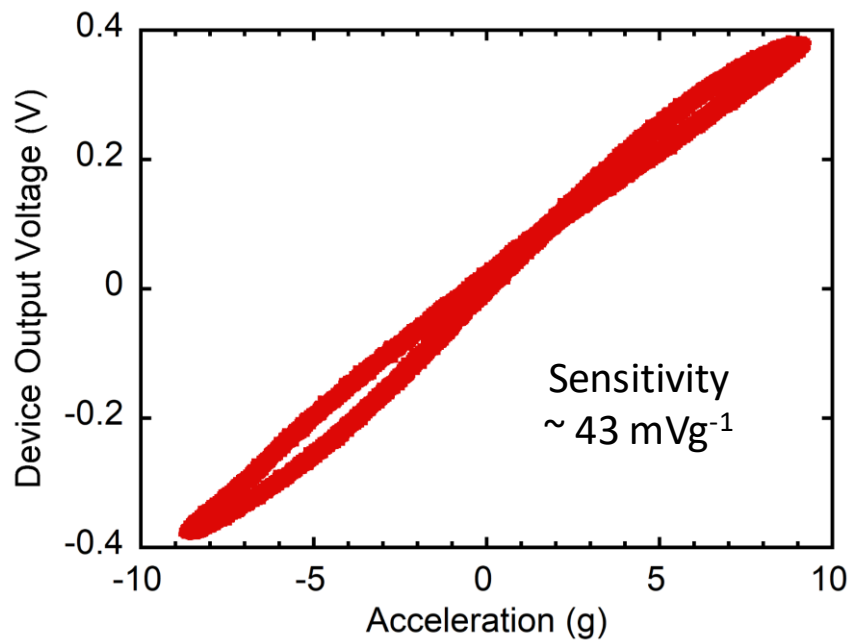


Figure 3.15: Phase-corrected output voltage vs acceleration plot. The response is linear with a sensitivity of  $43 \text{ mVg}^{-1}$ .

### **3.4.3. Bandwidth widening**

The full width at half maximum (FWHM) bandwidth from the system response is calculated from Fig. 3.12 as 920 Hz. The bottom triboelectric layer acts similarly to a mechanical stopper for the suspended structure which leads to the widening of the bandwidth [119], [120]. The wide bandwidth is an instrumental feature for this TEH system as achieving a wide bandwidth is a fundamental target for any practical energy harvesting system.

The first two primary harmonic resonant peaks of the vibration of an aircraft skin lie at 800 Hz and 1500 Hz [8]. As the experimental optimum operating frequency of the fabricated TEH is 1150 Hz and the frequency bandwidth is 920 Hz, the presented TEH can cover both of the 800 Hz and 1500 Hz harmonic peaks from the aircraft skin vibration to harvest energy. Therefore, this presented TEH can have specific applications in different sensor and actuator systems in the aircraft industry. Moreover, this TEH can also have potential applications in automobile industry [180], micro-robotics systems [181], prosthetics systems [182], and sensor nodes in internet of things (IoT) [183] where the primary frequency of concern is around 1 kHz.

### **3.4.4. Summary**

Characterization results for the triboelectric energy harvester are presented in this section. The TEH was packaged and wire bonded to start the characterization process. The characterization setup is discussed in detail. The frequency response of the TEH is obtained and the load resistance of the system is optimized. Finally, the FWHM frequency bandwidth of the system is calculated.

## 3.5. Analyses and discussions

### 3.5.1. Back simulation with measured structural parameters

Since fabrication aspects included several novel steps with regards to adaptation of triboelectric materials into MEMS UV-LIGA process, it was expected that the dimensions achieved would be different than the nominal ones. For comparison, detailed measurements were done. The bottom triboelectric Teflon thickness was found to be 6  $\mu\text{m}$  after the dry etching step (Fig. 3.16). However, after the polyimide layer ashing, notching on the bottom triboelectric layer was observed which reduces the effective thickness of this layer (Fig. 3.9). An accurate measurement of the effective thickness was not possible. The perforation and unit cell radii of the suspended structure are 14.75  $\mu\text{m}$  and 27.6  $\mu\text{m}$ , respectively (Fig. 3.17(a) – 3.17(b)). The combined thickness of the suspended structure, on the other hand, is 15.1  $\mu\text{m}$  (Fig. 3.18). Finally, the accurate measurement of the air gap was also not possible due to the proof-mass bowing. Around the edge of the suspended structure, the air gap is 14  $\mu\text{m}$  whereas around the center, it is about 24  $\mu\text{m}$ .

Although the ashing was conducted at a high pressure for selective etching of the sacrificial polyimide with respect to the Teflon layer, the latter still displayed some damages, which turned out to be advantageous after all, increasing the triboelectric charge density. This is because the damages roughen the Teflon surface, which leads to a better contact between the triboelectric layers [184], [185], [186], [187]. Higher triboelectric charge density results in higher output power. Contrary to that, reduction in the effective Teflon layer thickness reduces the power output from the TEH. A back simulation was performed using the measured structural dimensions of the TEH. The input acceleration and the frequency were 9.33g and 1150 Hz, respectively. The optimum average power from the back simulation was found to be 206 nW whereas the experimental optimum average power is 179 nW.

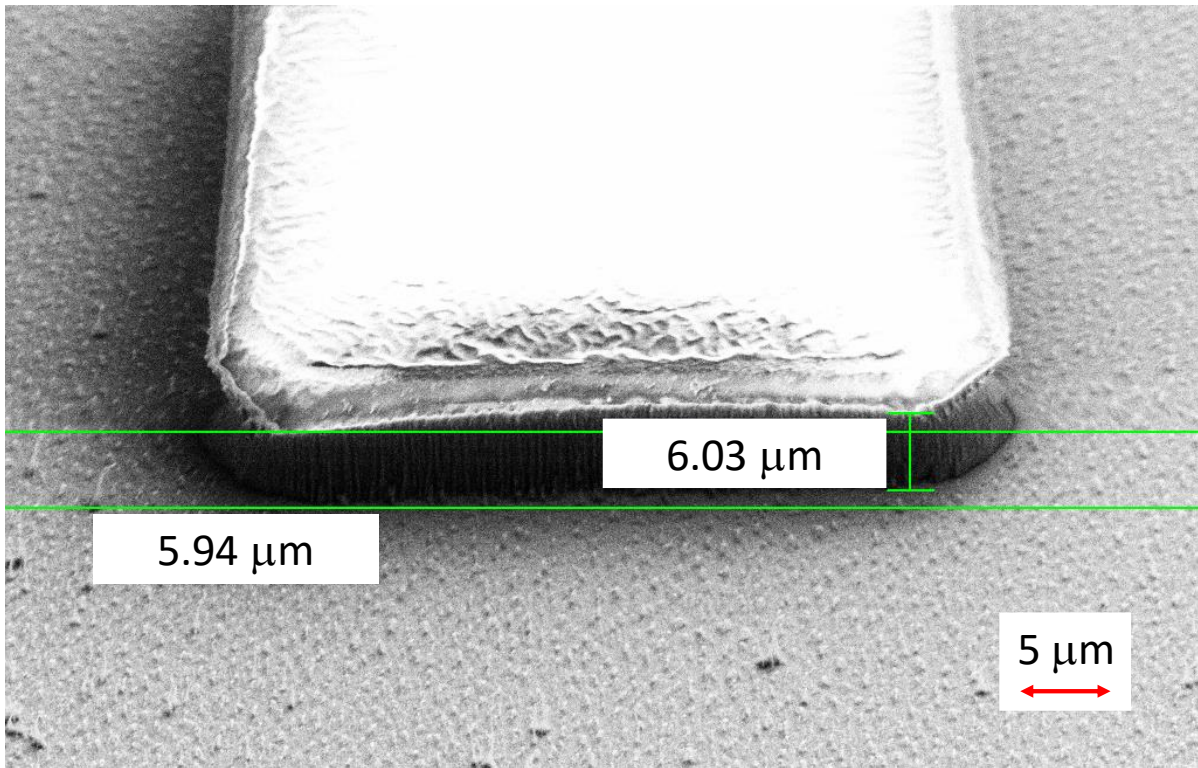


Figure 3.16: SEM image of the bottom triboelectric layer (Teflon) thickness after the Ar plasma etching.

The SEM stage was tilted at 45° angle.

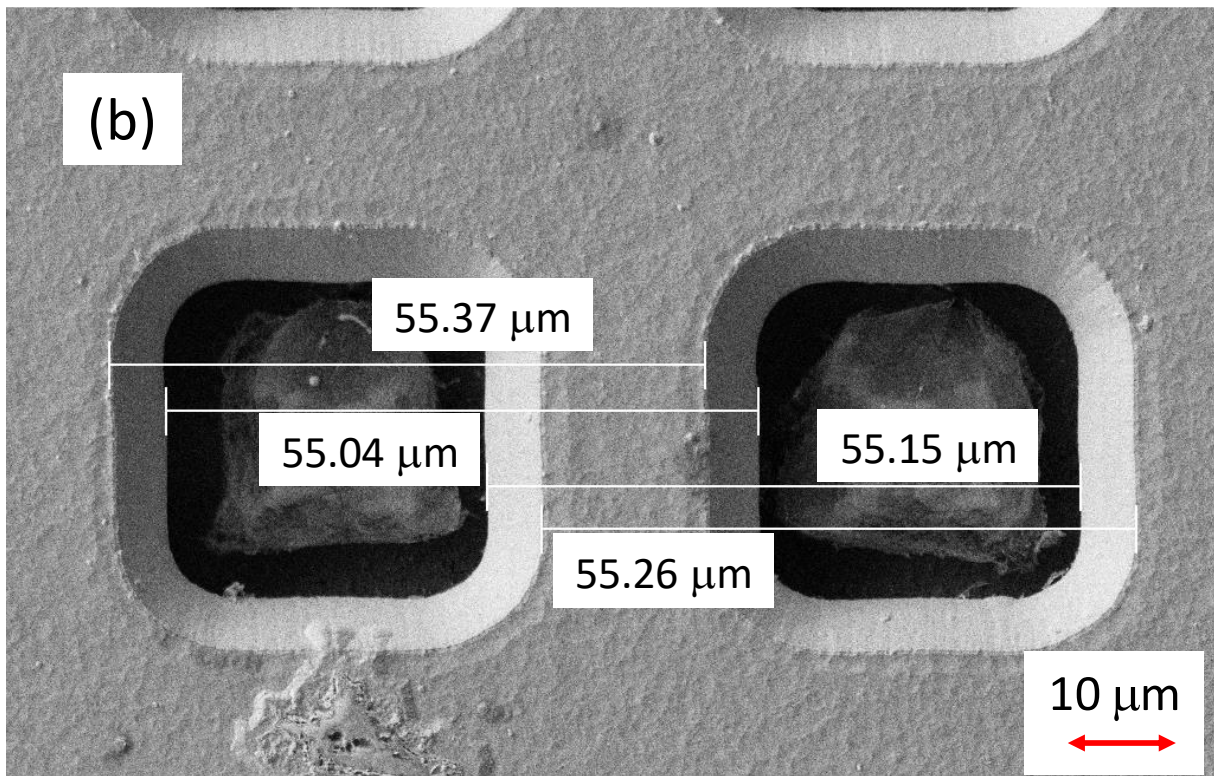
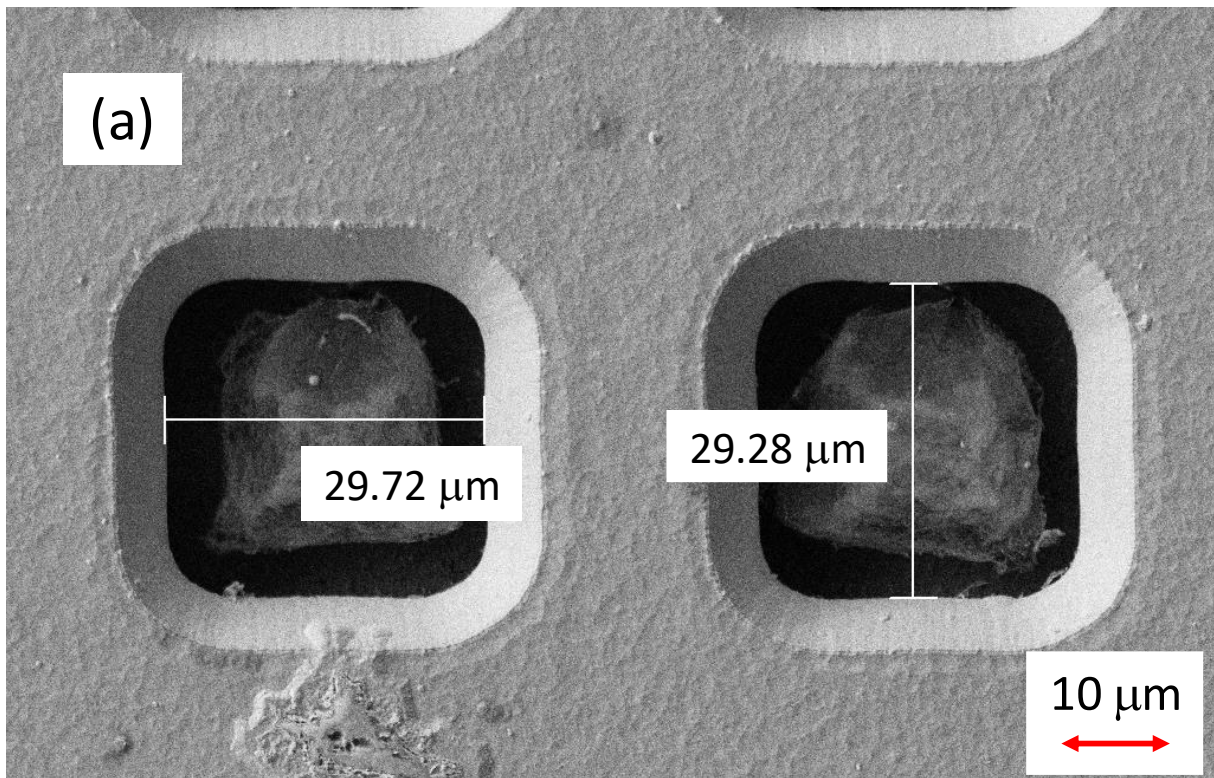


Figure 3.17: SEM image of the suspended structure for (a) perforation radius and (b) unit cell radius

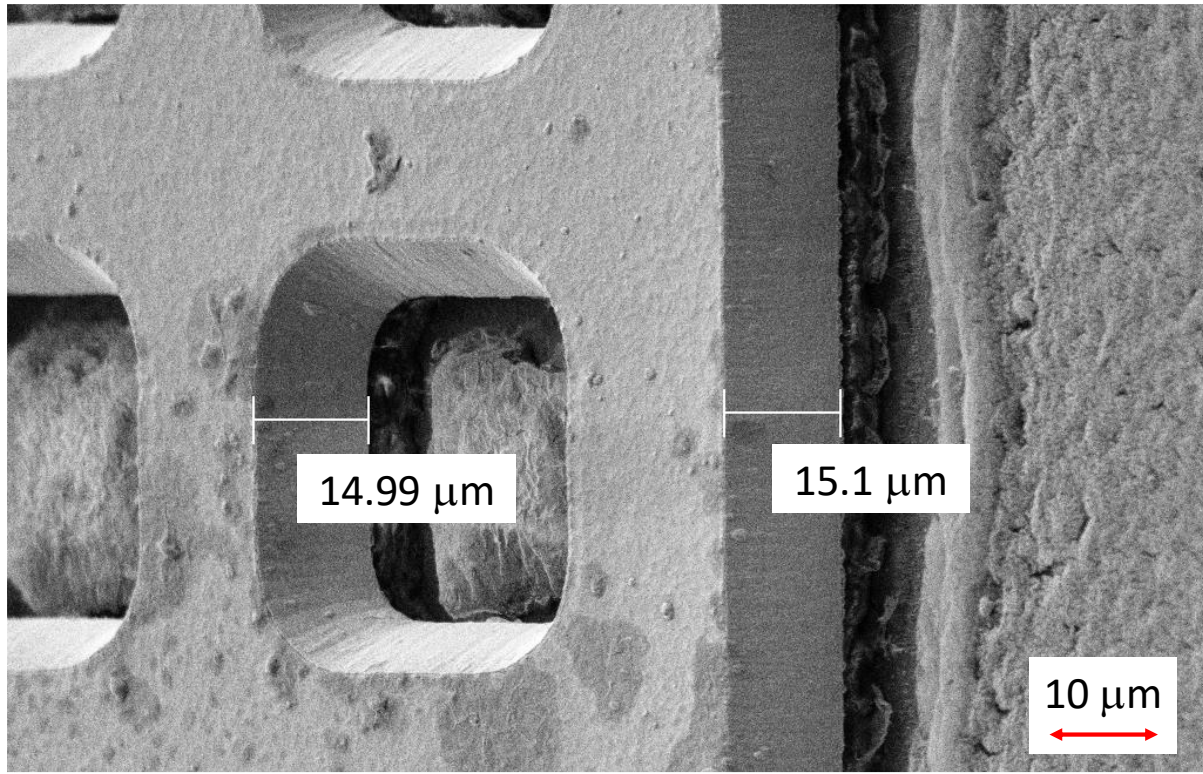


Figure 3.18: SEM image of the thickness of the suspended structure. The SEM stage was tilted by  $45^{\circ}$

### 3.5.2. Shifting of the optimum operating condition

From the simulation, the expected primary mode optimum frequency was 800 Hz as discussed in Section 3.2.2. However, characterization results show that the experimental optimum frequency is at 1150 Hz. The contact between the triboelectric layers can introduce new vibration modes that were not predicted by the simulation. Moreover, the mold layer for the electroplating process was slightly overdeveloped intentionally. This resulted in a slightly wider spring formation which is also a possible reason for the frequency shifting to a higher value [188].

The optimum load resistance of the system was predicted to be 10 M $\Omega$  from the initial simulation. Nevertheless, the experimental optimum load resistance is 256 K $\Omega$ . This deviation is attributed to two main

sources. The simulation predicts that the proof-mass bowing near the center portion of the suspended assembly reduces the optimum load resistance value. As discussed in the Figs. 3.10 (a) - (b), although the target air gap of the design was 14  $\mu\text{m}$ , near the center of the suspended structure, the air gap reaches to 24  $\mu\text{m}$ . In addition, the high degree of notching on the Teflon layer due the sacrificial polyimide ashing step also dramatically reduces the optimum load resistance. Unfortunately, we could neither obtain a high-confidence measurement of the air gap, nor could we measure and model the notching effect. A comparative study of how the air gap and Teflon thickness variation shift the optimum load resistance value is presented in Fig. 3.19.

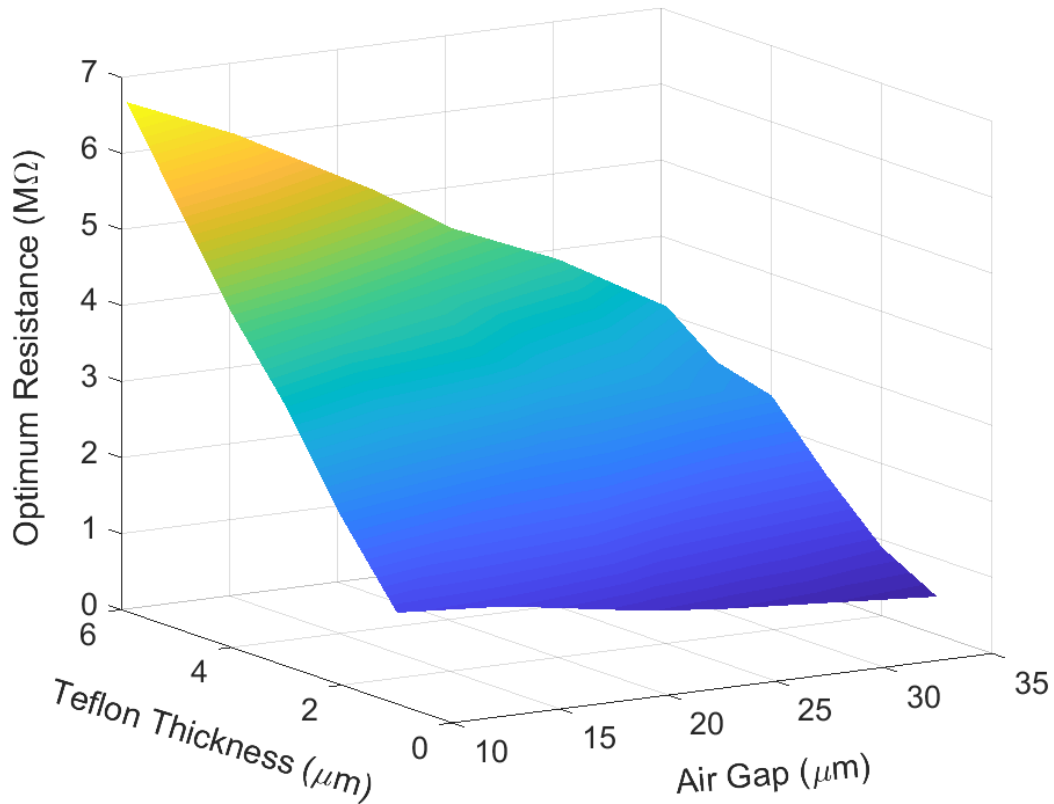


Figure 3.19: Variation of the optimum load resistance with the effective Teflon layer thickness and air gap.



### 3.5.3. Distortion of the simulated output voltage signal

As observed in Fig. 3.3(b), the simulation predicts distortion in the TEH output voltage, while it is insignificant in the measured one (Fig. 3.13(a)). This discrepancy can be explained by analyzing the characteristic electrical frequency of the circuit ( $1/RC_{ideal}$ ) and the mechanical vibration frequency of the system.

The TEH modeling was performed considering the ideal equivalent circuit model as discussed in Section 3.2.1. The total ideal capacitance for the model is  $1/C_{ideal} = 1/C_{device} + 1/C_{air}$  where,  $C_{device}$  is the fixed capacitance between the Teflon and the bottom electrode as defined earlier, and  $C_{air}$  is the variable capacitance between the triboelectric layers. These capacitances are plotted in Fig. 3.20(a).

Fig. 3.20(b) shows the characteristic electrical frequency of the circuit ( $1/RC_{ideal}$ ) as well as the angular mechanical vibrational frequency ( $\omega = 2\pi f$ ,  $f = 800$  Hz). It is evident that the latter is at the lower end of the range the electrical frequency sweeps. This mismatch leads to a distortion in the transferred charge through the load which results in a distorted voltage in the simulation [111] as in Fig. 3.3(b). If the same system is simulated at  $f = 2582$  Hz ( $\omega = 17.92$  kHz) to match the characteristic electrical frequency of the circuit, the distortion is not observed as depicted in Fig. 3.21.

The experimentally observed mechanical resonant frequency value is, however,  $f = 1150$  Hz. Moreover, in practice, an additional parasitic capacitance  $C_{par}$  is also present in the system (Fig. 3.22) [111], making the total capacitance  $C_{total} = C_{ideal} + C_{par}$ . This lowers  $1/RC_{total}$ . As a result, for the practical circuit, the mismatch between  $1/RC_{total}$  and  $\omega$  is insignificant, resulting in an almost distortionless output voltage profile as depicted in Fig. 3.13(a).

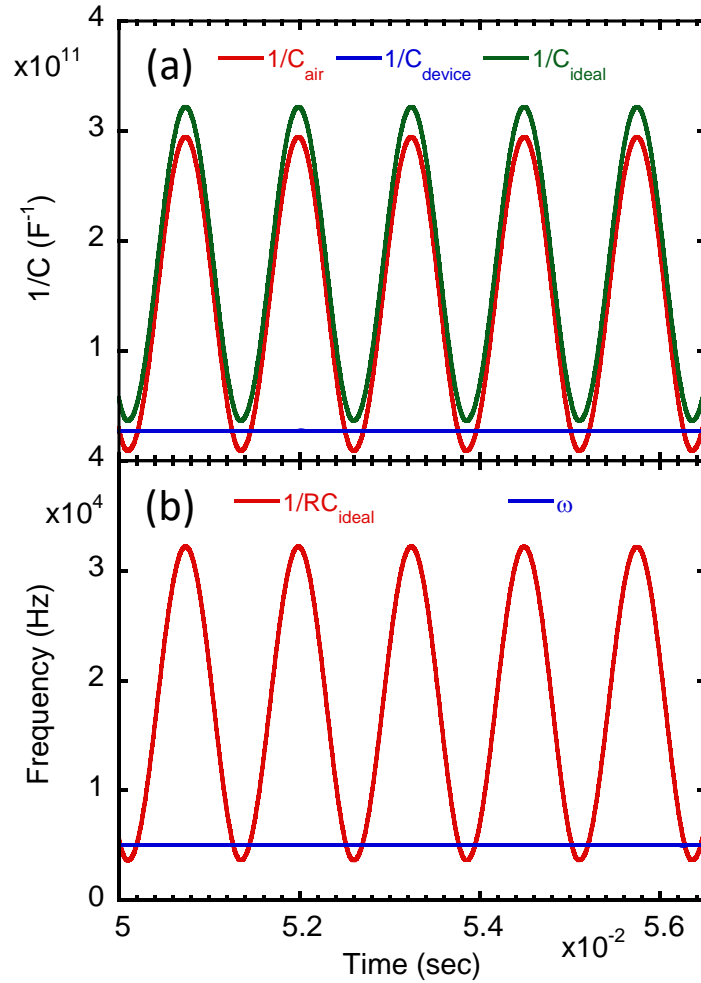


Figure 3.20: Initial model parameters. The system is simulated at 800 Hz vibration frequency and 1g acceleration. (a) System capacitances. (b) The resultant characteristic electrical frequency of the circuit ( $1/RC_{ideal}$ ) for  $R=10 \text{ M}\Omega$  and the mechanical vibration frequency of the system ( $\omega$ ).

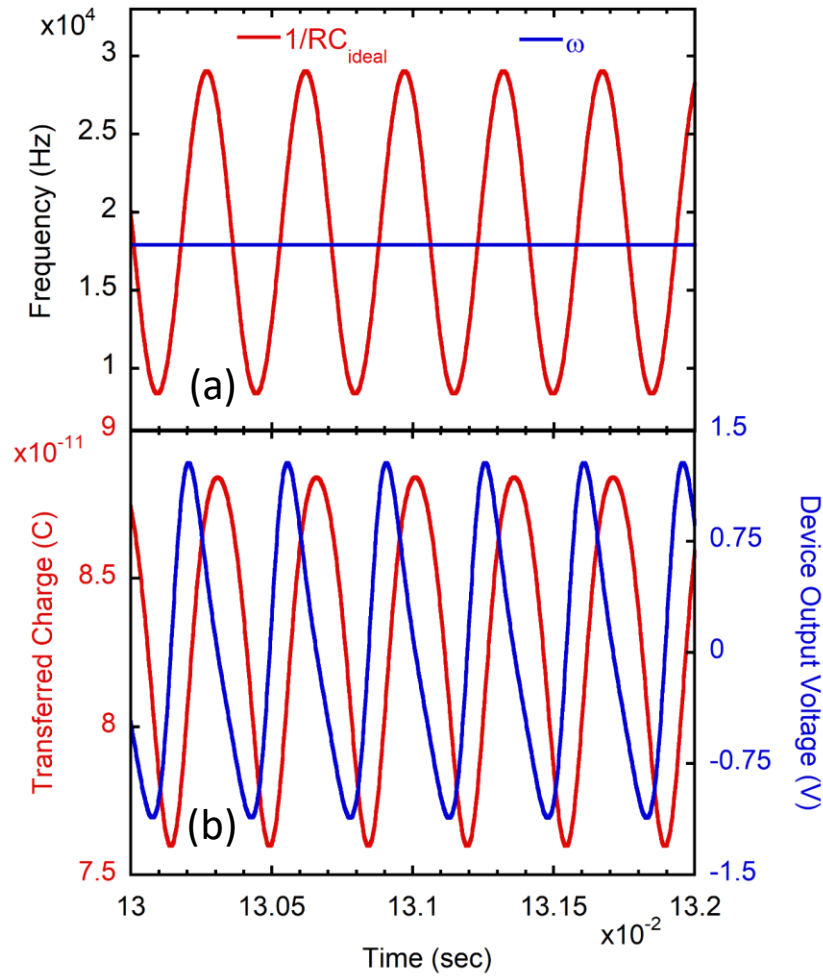


Figure 3.21: The same system in Fig. 3.20 is simulated at the vibration frequency of 2852 Hz and 1g acceleration. (a) The resultant characteristic electrical frequency of the circuit ( $1/RC_{ideal}$ ) for  $R = 10 \text{ M}\Omega$  and the mechanical vibration frequency of the system ( $\omega$ ). (b) TEH output charge and voltage profiles, showing no distortion.

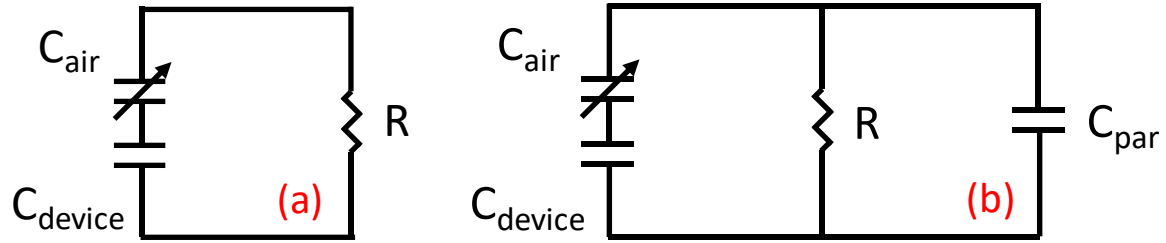


Figure 3.22: Equivalent circuit model of the triboelectric energy harvester. (a) Ideal circuit model. (b) Parasitic capacitance model

### 3.5.4. Summary

Discrepancies between the simulation and the experiment and, possible explanations for those discrepancies are presented in this section. Back simulation with the measured device parameters demonstrates that the average power predicted from the simulation matches closely to the experimentally obtained average power. Two major deviations between the simulation and the experiment are the value of the optimum load resistance and the output voltage profile distortion. The optimum load resistance is much smaller than that in the simulation because of the bowing of the proof-mass and the reduction in the effective Teflon thickness due to notching. Another discrepancy is in the output voltage profile. The simulated output voltage predicted the presence of distortions. However, this distortion was not observed in the experimental output voltage profile due to the presence of the parasitic capacitance in the system.

### 3.6. Comparison of the triboelectric energy harvester performance with the state-of-the-art

A comparison of the presented TEH design with some of the state-of-the-art energy harvester designs is displayed in Table 3.3. The effective volume of the presented TEH is much smaller than the conventional triboelectric energy harvesters published in the literature, resulting in a much smaller absolute power and higher operating frequency and wider relative frequency bandwidth. The effective volume is defined as the volume of the device configuration section that directly generates the energy (e.g. proof-mass volume for the presented TEH). The volumetric power density for vibrational energy harvesters is

usually quadratically normalized per acceleration [188], [189], [36], [37]. The volumetric power density, and acceleration-normalized power density of the presented TEH are competitive among the state-of-the-art designs, especially, if compared to the triboelectric energy harvesters.

The surface power density of the presented TEH is similar to the two reported in [35] and [190], but higher than the two reported in [103] and [104]. The spherical ball of [36] is a completely different geometry which cannot be incorporated into MEMS technology, although it is able to produce about twice as much surface power density. As for the one excited by a 50 N force [114], since the acceleration is unknown, no meaningful comparison is possible. Although included in the table, the surface power generated by the piezoelectric effect should not be directly compared with that obtained using TEHs, as piezoelectricity is a volume effect. Furthermore, the charge skin depth is not zero for the nonmetallic triboelectric energy harvesters, which makes it hard to achieve a meaningful comparison between metallic and nonmetallic TEH materials.

Table 3.3: Performance comparison of the presented TEH with the state of the art designs from literature

Type of the Energy Harvester	Device Configuration and Dimensions	Effective Volume (cm <sup>3</sup> )	Input Acceleration A (ms <sup>-2</sup> )	Center Frequency f (Hz)	Bandwidth (Hz)	Peak Power, P (μW)	Surface Power Density, SPD (μWcm <sup>-2</sup> )	Volumetric power Density, VPD (μWcm <sup>-3</sup> )	VPD/A <sup>2</sup> (μWcm <sup>-3</sup> )/g <sup>2</sup>
Electrostatic [188]	Rectangular proof-mass (1.95 mm × 1.26 mm × 7 μm)	$1.72 \times 10^{-5}$ (c)	8g	1900	–	0.032 (c)	1.30 (c)	$1.86 \times 10^3$ (c)	29.1 (c)
Electrostatic [191]	Rectangular proof-mass (11 mm × 6.5 mm × 0.86 mm)	$6.15 \times 10^{-2}$ (c)	0.23g	250	–	0.061	0.085 (c)	0.992 (c)	18.8 (c)
Piezoelectric [192]	Cantilever beam (4800 μm × 400 μm × 22 μm) and proof-mass (1415 μm × 1015 μm × 506 μm) system	$7.69 \times 10^{-4}$	0.75g	183.8	–	0.638 (c)	19.0 (c)	$8.30 \times 10^2$ (c)	$1.47 \times 10^3$ (c)
Piezoelectric [193]	Two separate cantilever structures (3.45 mm × 2 mm × 0.4 mm each)	$5.52 \times 10^{-3}$ (c)	0.8g	36	22	0.880 (c)	6.38 (c)	$1.59 \times 10^2$	$2.49 \times 10^2$ (c)
Piezoelectric [59]	Two rectangular proof-mass structures, (552 μm × 552 μm × 10 μm each)	$6.09 \times 10^{-6}$ (c)	1.4g	40	–	$7 \times 10^{-5}$	0.011 (c)	11.5 (c)	5.86 (c)
Electromagnetic + Piezoelectric [194]	Box shaped hybrid electromagnetic (8.3106 cm <sup>3</sup> volume) and piezoelectric (3.6231 cm <sup>3</sup> volume) system	11.9 (c)	35g	20	–	$2.50 \times 10^5$	–	$2.10 \times 10^4$ (c)	17.1 (c)

Triboelectric + Electromagnetic [190]	Hybrid triboelectric and electromagnetic system (4 cm × 4 cm × 2.5 cm)	40 (c)	2g	80	68	50.2	3.14 (c)	1.26 (c)	0.314 (c)
Triboelectric [114]	Rectangular plate (5 cm × 5 cm × 0.055 cm)	1.38 (c)	50 N (force)	5	–	3130	$1.25 \times 10^2$ (c)	$2.28 \times 10^3$ (c)	–
Triboelectric [103]	PTFE cylinder with 12 cm length, 5.5 cm diameter and 1 mm thickness. Ends of the cylinder were blocked with 50 μm thick PTFE films.	20.6 (c)	17.6g	5	22	$6.75 \times 10^2$ (c)	2.65	32.8 (c)	0.106 (c)
Triboelectric [104]	Rectangular PDMS plate (2 cm × 2 cm × 0.05 cm)	0.2 (c)	1g	30	22.05	0.91	0.238 (c)	4.55 (c)	4.55 (c)
Triboelectric [36]	Spherical ball (radius 1 cm)	4.19 (c)	3.66g (c)	20	–	128	10.2 (c)	30.5 (c)	2.27 (c)
Triboelectric [35]	Rectangular box with spiral cavity (3 cm × 3 cm × 6 cm)	54 (c)	2.35g	16	–	162 (c)	4.5	3.0 (c)	0.543 (c)
This paper (Triboelectric)	<b>Rectangular proof- mass (5000 μm × 3000 μm × 15.1 μm)</b>	<b><math>2.27 \times 10^{-4}</math></b>	<b>9.33g</b>	<b>1150</b>	<b>920</b>	<b>0.597</b>	<b>3.98</b>	<b><math>2.64 \times 10^3</math></b>	<b>30.3</b>

Here,  $g = 9.8 \text{ ms}^{-2}$  (gravitational acceleration) and (c) refers to calculated from the information provided on the respective references.

### 3.7. Conclusion

A micrometer-scale triboelectric vibrational energy harvester with a high operating frequency and wide bandwidth is presented. The TEH is structurally optimized to achieve the highest average power and power density while ensuring structural robustness. A novel hybrid fabrication technique is utilized involving conventional UV-LIGA and Teflon AF / aluminum triboelectric layers. If excited by an external vibration of  $\pm 9.33g$  at 1150 Hz frequency, the TEH can generate an average power of  $0.18 \mu W$  and a peak power of  $0.6 \mu W$  with an optimum load of  $256 k\Omega$ . The peak power density and acceleration-normalized power density reach  $2.64 mWcm^{-3}$  and  $30.22 \mu Wcm^{-3}/g^2$ , respectively. The TEH also demonstrates a wide operating bandwidth of 920 Hz. If operated as an accelerometer, the TEH demonstrates a linear sensitivity of  $43 mV/g$ . Differences between the simulated and the final fabricated device performance are also discussed in detail. The aforementioned triboelectric energy harvester can have specific applications in the sensor and actuator systems in the aircraft industry as well as in the automobile industry, micro-robotic systems, prosthetic systems, and sensor nodes in the internet of things (IoT) based on its operating frequency and frequency bandwidth range.



## Chapter 4 : Conclusion

More and more applications are now being opened up for the vibrational energy harvesters as the technological push for device dimension scaling and power-efficient designs are reducing the power requirement of every electronic device and sensor. This dissertation consists of two separate projects, both of which are focused on harvesting electrical energy from ambient vibration sources. The first project focuses on improving the piezoelectric performance of arguably the most popular piezoelectric material, ZnO, by controlled incorporation of substitutional Li doping. The second project focuses on a novel design of a MEMS scale triboelectric energy harvester with a high target frequency and wide frequency bandwidth.

### **4.1. Piezoelectric performance modification of ZnO nanowires with controlled incorporation of substitutional Li doping**

To mitigate a few major drawbacks of ZnO NWs including electron screening and low piezoelectric coefficient, controlled doping of substitutional Li was incorporated into its structure. This incorporation was achieved by the addition of a Li reagent into the nutrient solution of the hydrothermal growth process of ZnO NWs. Five samples with different Li doping concentrations were fabricated.

The as-grown NWs are then characterized intricately to observe the effect of Li doping. Physical characterization demonstrated that Li stunned the growth rate of the ZnO NWs while its density (no. of NWs per unit area) increased significantly. However, the doping did not have a significant impact on the NW diameter. Raman spectroscopy, XRD, EDS, and XPS analysis were conducted to observe the Li doping impact on the ZnO crystal structure from the material point of view. All of these analyses exhibited and confirmed the incorporation of the Li atoms in the ZnO crystal structure as a substitutional dopant.

The NWs were then subjected to a force to characterize their piezoelectric response. An AFM system was utilized for this force exertion purpose. The force normalized measured voltage demonstrated

that doping improved the piezoelectric sensitivity of the NWs by more than 22-fold. This improvement in the sensitivity, however, was due to the combination of improved piezoelectric response by the NWs and their modified physical dimensions. Simulation results disclosed that if the impact of physical dimension modifications is removed, the effective improvement in the sensitivity is reduced to 7-fold. We suspect that at sufficiently high doping concentration, the kick-out diffusion mechanism is introduced into the system which significantly reduces the electron screening effect. In addition, incorporation of Li into the substitutional sites of ZnO reduces its lattice constant, leading to a higher structural anisotropy and as a result, improved piezoelectric response. However, at very high doping concentrations, the formation of acceptor complexes, deep levels, and dislocations lead to lower structural quality for ZnO, which reduces the piezoelectric sensitivity. It is estimated that there is an optimum level of Li doping concentration which can lead to the best piezoelectric performance from the ZnO NWs.

#### **4.2. A MEMS scale triboelectric energy harvester with high operating frequency and wide bandwidth fabricated using UV LIGA technique**

The design, fabrication, and characterization of a MEMS scale triboelectric energy harvester was presented in the 2<sup>nd</sup> project of this dissertation. The TEH was designed to operate at a high target vibration frequency and achieve a wide frequency bandwidth. Teflon – Al pair was used as the triboelectric materials based on the large difference between their tendency to lose or gain electrons in the triboelectric series and their compatibility with common MEMS fabrication processing.

The dynamic model of the device was created considering the coupled electrical and mechanical systems. The model is then numerically solved to achieve optimum structural parameters for the device in terms of maximum average power and power density. Detailed spring designing techniques were presented to keep the generated stress within the yield strengths of the materials used and to achieve a stable system with large vibration mode separation.

The fabrication of the device included several novel approaches. For instance, spin-coated Teflon AF was used instead of a regular Teflon sheet to avoid any bubble formation and achieve improved adhesion properties considering the MEMS scale size of the device. A thick HD4110 photo definable polyimide was used as the sacrificial layer material to achieve a relatively high air gap between the triboelectric layers. This sacrificial layer was ashed off at the final fabrication step in high-pressure O<sub>2</sub> plasma. In addition, a modified UV-LIGA technique was adopted to achieve a relatively thick MEMS proof-mass.

Extensive characterization was conducted on the fabricated TEH device. The TEH achieved an average power of 0.18  $\mu\text{W}$  and peak power of 0.6  $\mu\text{W}$  with an optimum load of 256 k $\Omega$  if excited by an external vibration of  $\pm 9.33\text{g}$  acceleration at 1150 Hz frequency. The peak power density and acceleration-normalized power density reach 2.64  $\text{mWcm}^{-3}$  and 30.22  $\mu\text{Wcm}^{-3}/\text{g}^2$ , respectively. The TEH also demonstrates a wide operating bandwidth of 920 Hz. If operated as an accelerometer, the TEH demonstrates a linear sensitivity of 43 mV/g.

A back simulation was performed using the measured device parameters to compare the harmony between the simulated and the experimental data. The discrepancies observed between the simulation and the experiment were explained.

### **4.3. Applications**

Both devices developed in this work can be implemented in several application fields. The Li doped ZnO NWs demonstrated considerably higher sensitivity compared to its undoped counterpart which can lead to the development of high-performance sensors. On the other hand, the triboelectric energy harvester design presented in the 2<sup>nd</sup> project was dramatically scaled down in terms of volume compared to any other design available in the literature. The small MEMS scale size and low mass make it an attractive design for volume and mass constrained applications like in space exploration programs. Few possible applications of the presented designs include:

- Sensor nodes in internet of things (IoT)
- Automobile industry as self-powered sensors
- Aircraft industry as self-powered sensors
- Space exploration programs as self-powered sensors and energy harvesters
- Micro-robotics systems as sensors and accelerometers
- Prosthetic systems as sensors and accelerometers
- Defense and commercial navigation systems as sensors and accelerometers
- Self-powered sensor nodes for environmental monitoring systems

## Appendix A: Derivation of the circuit model for AFM tip-nanowire interaction

When the AFM tip interacts with the NWs and applies a force, it usually bends more than one NW. As a result, each of the bent NWs generate a piezoelectric voltage. These nanowires can be modeled as voltage sources with a contact resistance between them and the AFM tip. All of these NWs are connected in parallel to each other and also with the load resistance as shown in Fig. A.1. The final voltage observed at the load can be derived as follows:

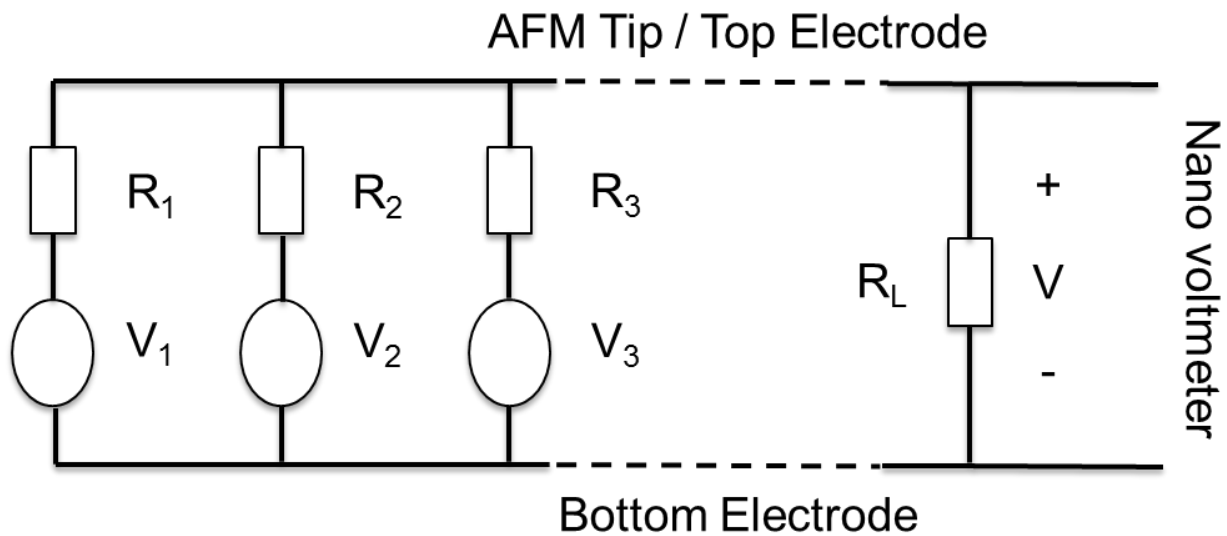


Figure A.1: Circuit model for the AFM tip-nanowire interaction

Let us consider,

$R_1, R_2, R_3 \dots$  = Contact resistance between the AFM tip and the nanowires

$V_1, V_2, V_3 \dots$  = Piezoelectric generated voltage (modeled as a voltage source) from the nanowires

$R_L$  = Load resistance ( $6.7 \text{ M}\Omega$ )

$V$  = Voltage across the nano voltmeter

Applying Kirchhoff's Current Law (KCL)

$$(V-V_1)/R_1 + (V-V_2)/R_2 + (V-V_3)/R_3 + V/R_L = 0$$

$$\Rightarrow (V-V_1)/R + (V-V_2)/R + (V-V_3)/R + V/R_L = 0 \text{ [Assuming all the contact resistances are equal]}$$

$$\Rightarrow (V-V_1+V-V_2+V-V_3)/R + V/R_L = 0$$

$$\Rightarrow (3V-V_1-V_2-V_3)/R = -V/R_L$$

$$\Rightarrow 3V-V_1-V_2-V_3 = -(R/R_L)V$$

Now,  $R_L \gg R$

Therefore,

$$3V-V_1-V_2-V_3 = 0$$

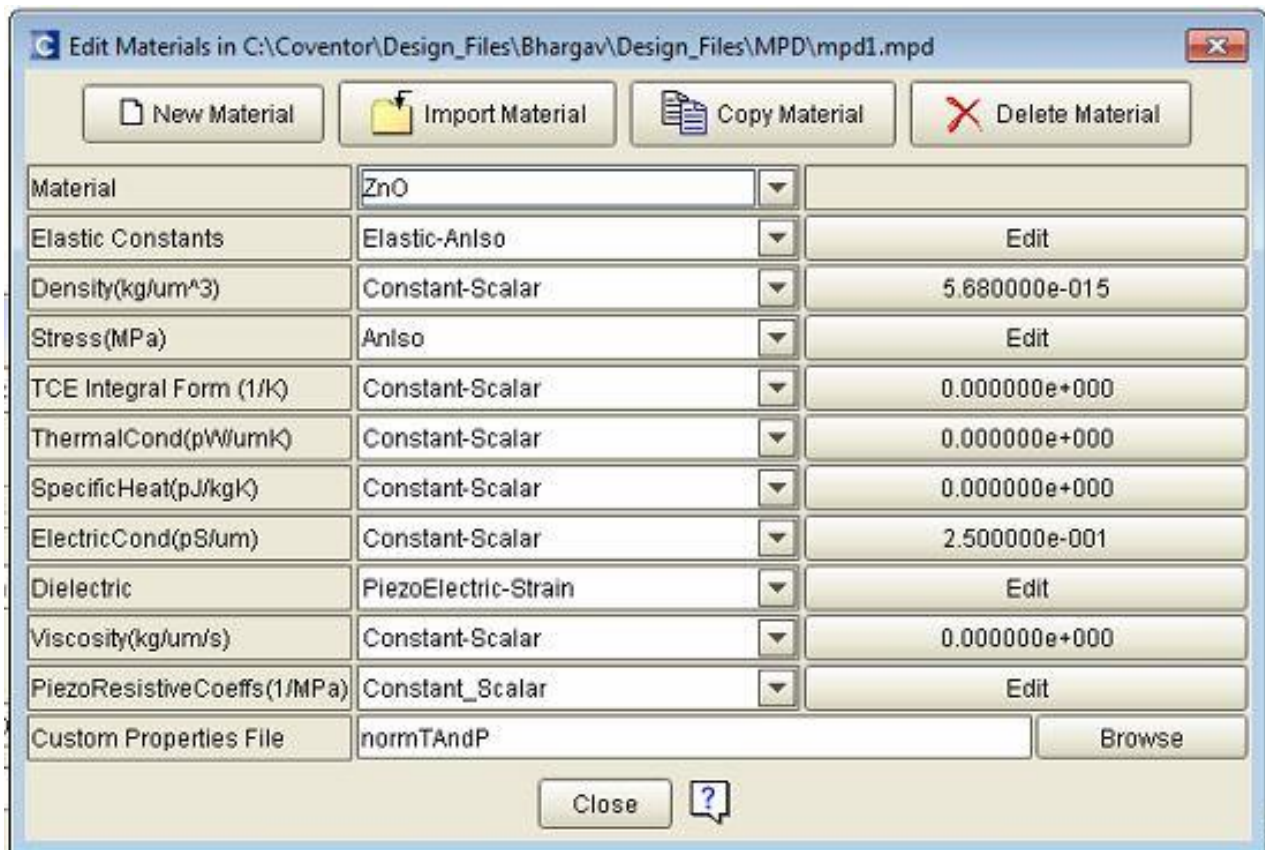
$$\Rightarrow 3V = V_1 + V_2 + V_3$$

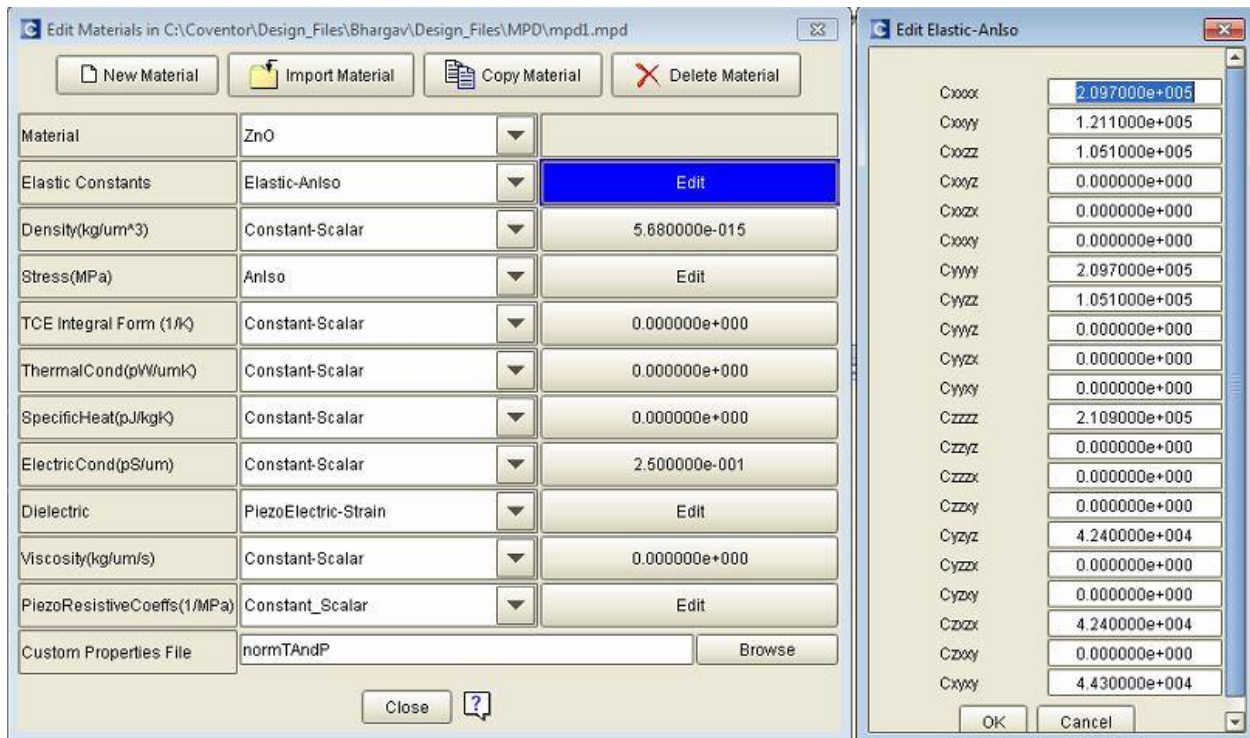
$$V = (V_1 + V_2 + V_3)/3 \tag{A.1}$$

The equation A.1 signifies that the voltage observed at the output is the average of the voltages generated by all of the NWs.

## Appendix B: Coventorware™ settings for the ZnO nanowire displacement simulation

Coventorware™ was used to simulate the displacement of the NWs corresponding to a defined force by the AFM tip. The parameter settings for the simulation are described as below:

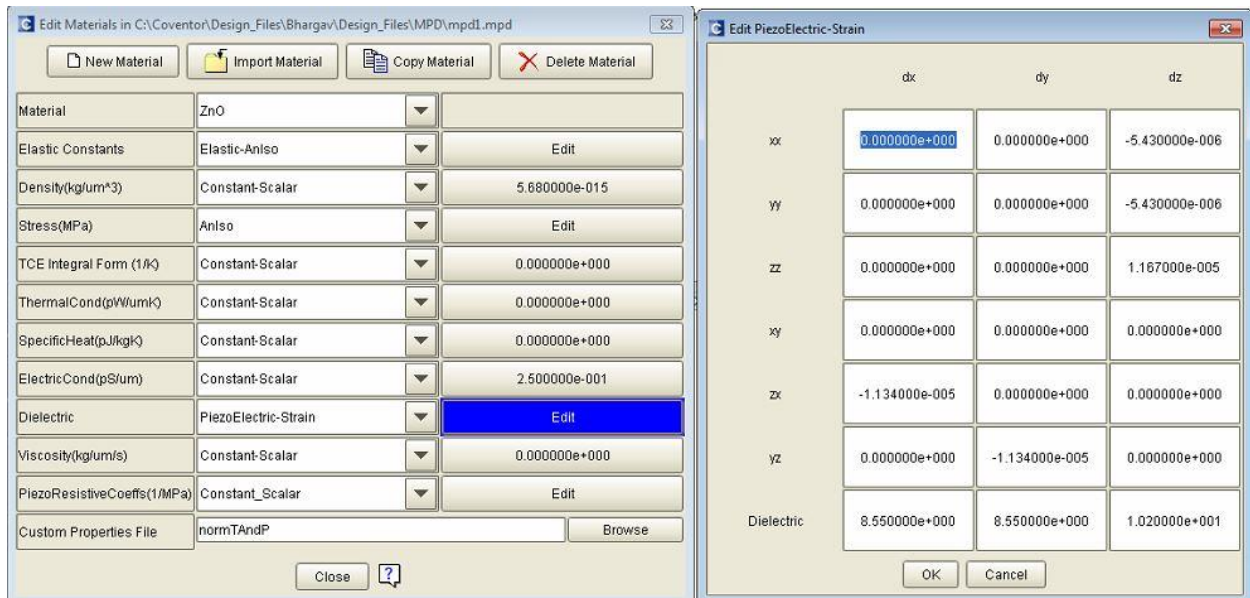




Edit Elastic-Aniso

Cxxxx	2.097000e+005
Cxyy	1.211000e+005
Cxzz	1.051000e+005
Cxyz	0.000000e+000
Cxxz	0.000000e+000
Cxxy	0.000000e+000
Cyyy	2.097000e+005
Cyyz	1.051000e+005
Cyyx	0.000000e+000
Cyyz	0.000000e+000
Cyyx	0.000000e+000
Czzz	2.109000e+005
Czyz	0.000000e+000
Czzx	0.000000e+000
Czzy	0.000000e+000
Cyzx	4.240000e+004
Cyzx	0.000000e+000
Cyzy	0.000000e+000
Czxx	4.240000e+004
Czxy	0.000000e+000
Cxyy	4.430000e+004

OK Cancel



Edit PiezoElectric-Strain

	dx	dy	dz
xx	0.000000e+000	0.000000e+000	-5.430000e-006
yy	0.000000e+000	0.000000e+000	-5.430000e-006
zz	0.000000e+000	0.000000e+000	1.167000e-005
xy	0.000000e+000	0.000000e+000	0.000000e+000
zx	-1.134000e-005	0.000000e+000	0.000000e+000
yz	0.000000e+000	-1.134000e-005	0.000000e+000
Dielectric	8.550000e+000	8.550000e+000	1.020000e+001

OK Cancel

Figure B.1: Material properties of ZnO in Coventorware™



Number	Step Name	Layer Name	Material Name	Thickness	Mask Name	Photoresist	Depth	Mask Offset	Sidewall Angle	Comments
0	Substrate	Substrate	SILICON_100	10	SubstrateMask					
1	Stack Material	ZnO_NR	ZnO	9.836						
2	Straight Cut				ZnO_NR	+		0	0	
3	Planar Fill	Sacrificial	POLYIMIDE	12.268						
4	Straight Cut				AFM_tip	-	12.5	0	-25	
5	Planar Fill	AFM_tip	SILICON_100	0						
6	Delete		POLYIMIDE							
7	Stack Material	AFM_cantilever	SILICON_100	4						
8	Straight Cut				SubstrateMask	+		0	0	
9	Stack Material	Marker	ALUMINUM	0.1						
10	Straight Cut				AFM_tip	+		0	0	

Figure B.2: Process flow in Coventorware™

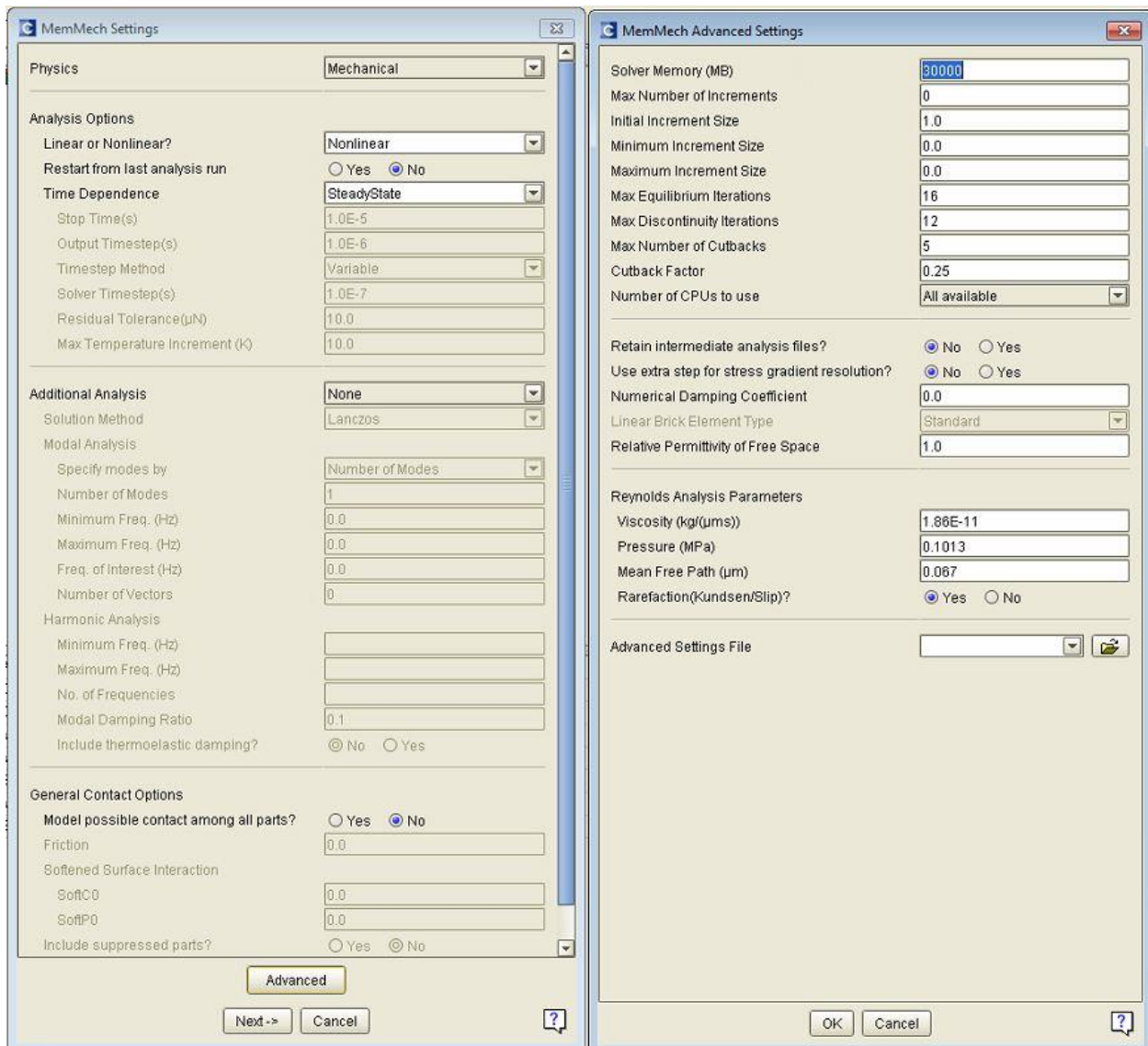


Figure B.3: MemMech solver settings in Coventorware™

# Appendix C: Ansys™ settings for the ZnO nanowire piezoelectric response simulation

Ansys™ was used to simulate the piezoelectric voltage generated corresponding to a defined force by the AFM tip. The parameter settings for the simulation are described as below:

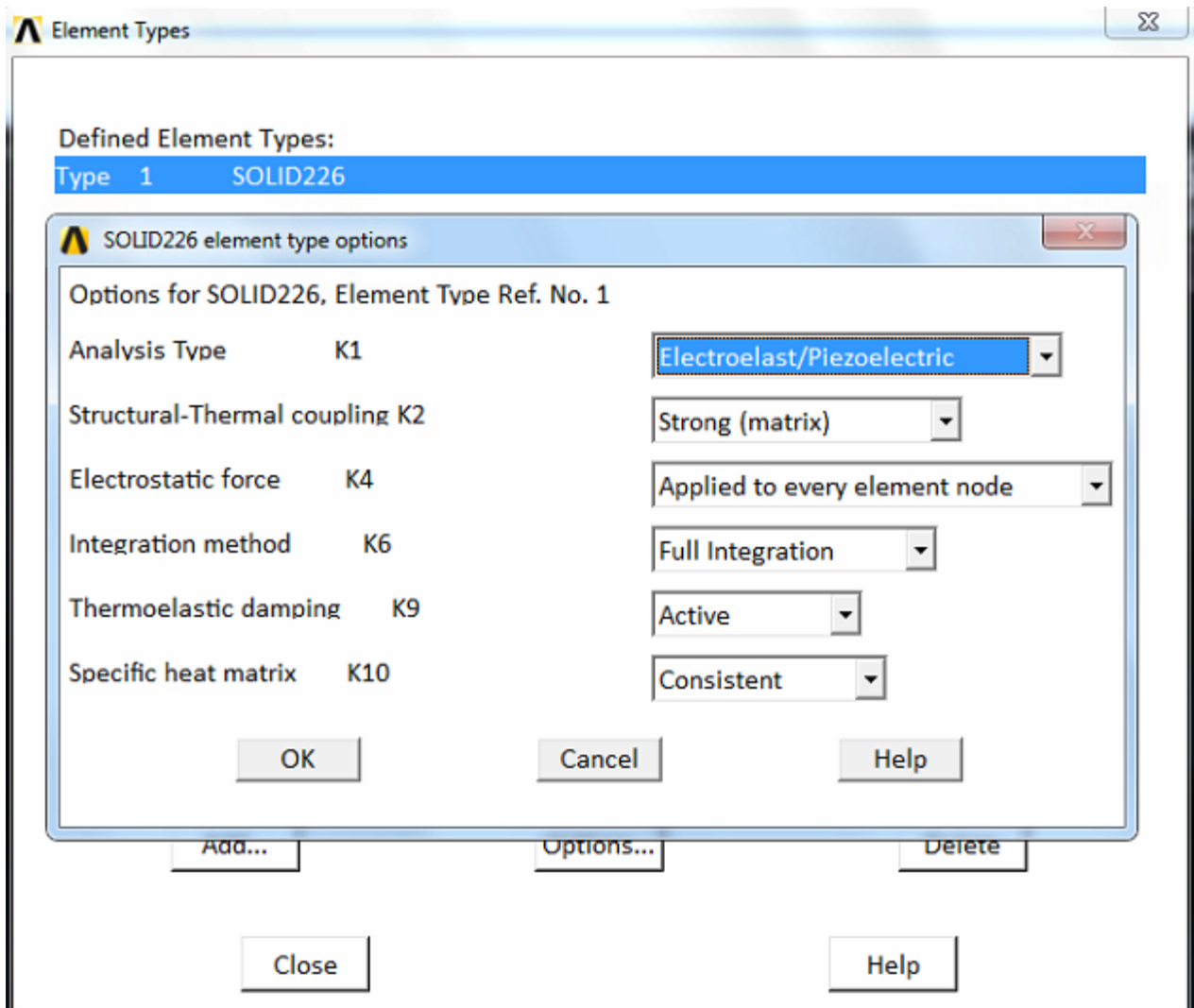
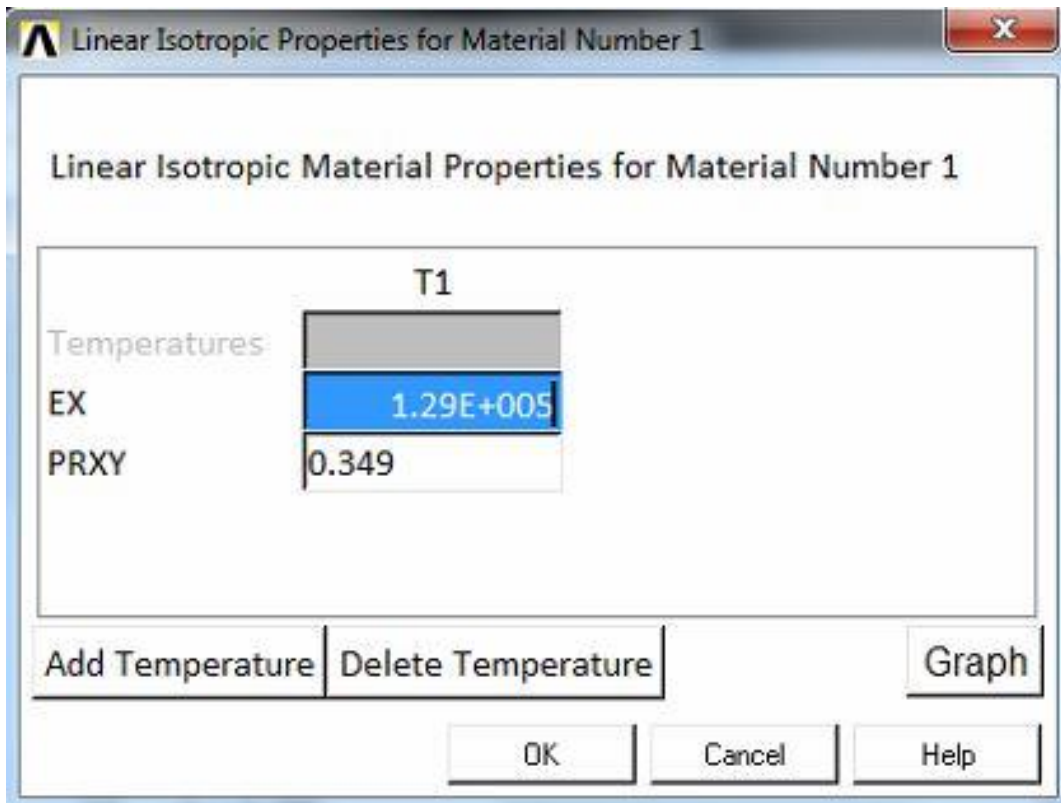
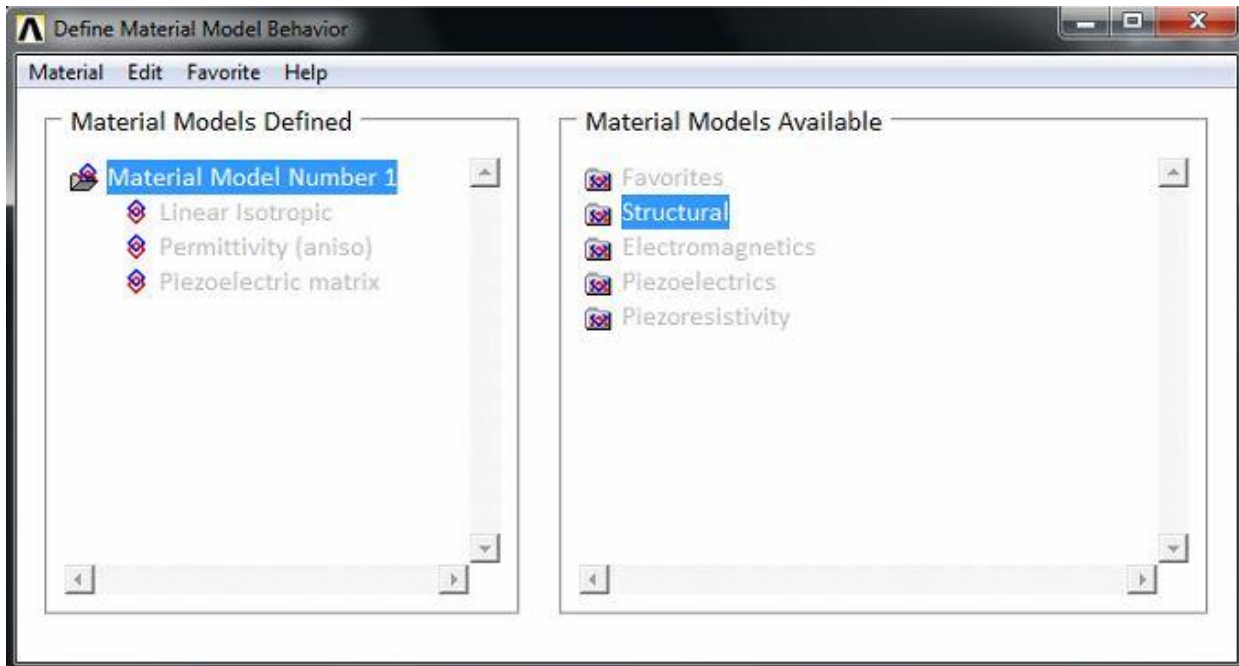


Figure C.1: Element type selection in Ansys™



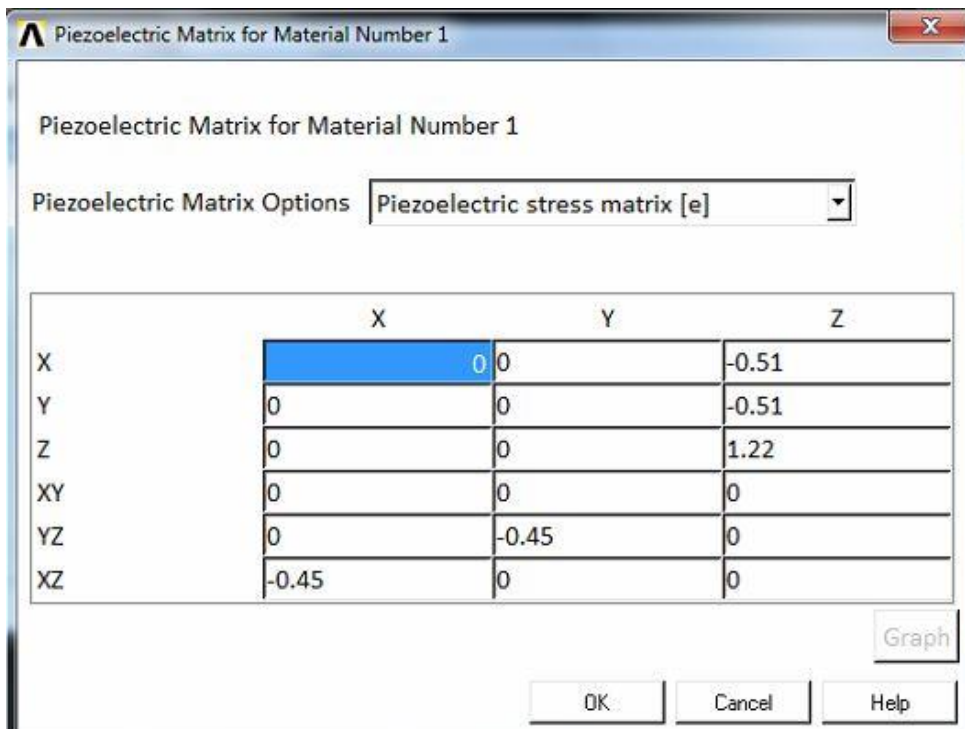
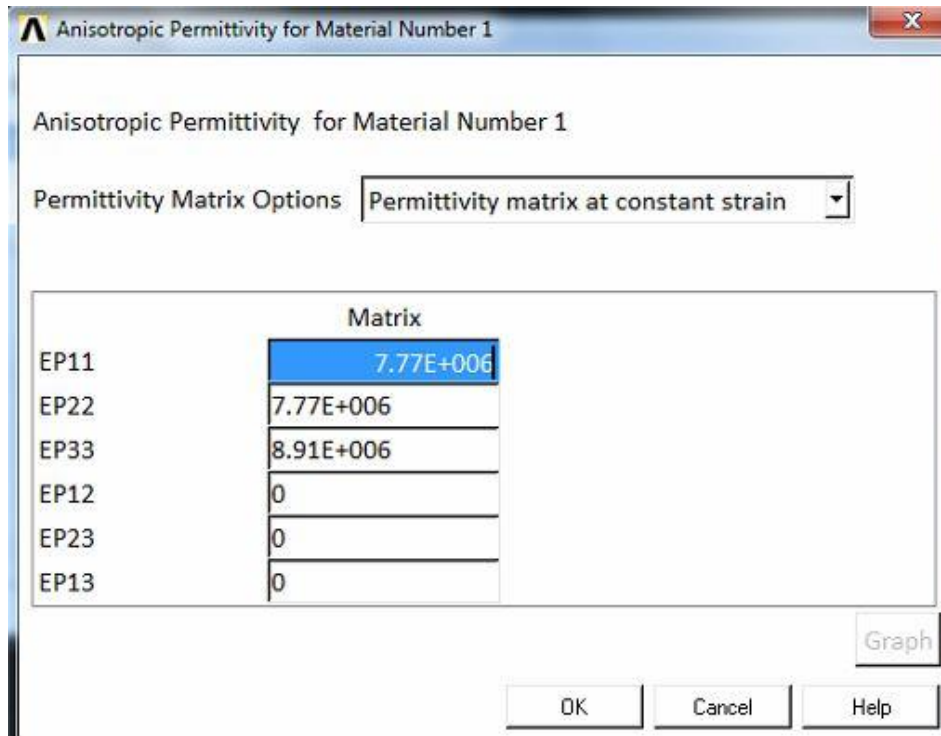


Figure C.2: Material property setting for ZnO nanowire in Ansys™

## Appendix D: Mask layout for the triboelectric energy harvester

The triboelectric energy harvester mask layouts were created using the Coventorware™ software.

A total of 4 masks were used to create the TEH. The mask layouts are provided below:



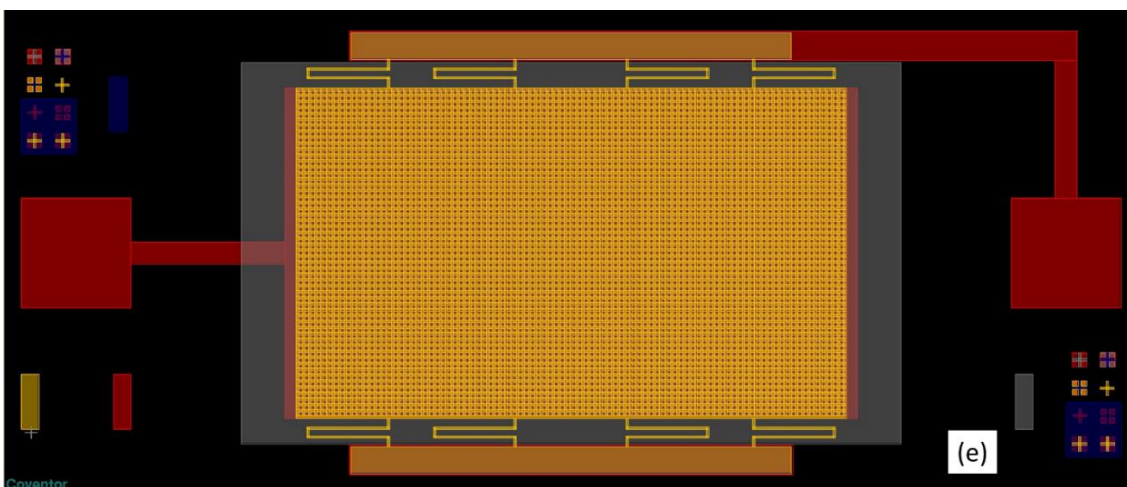
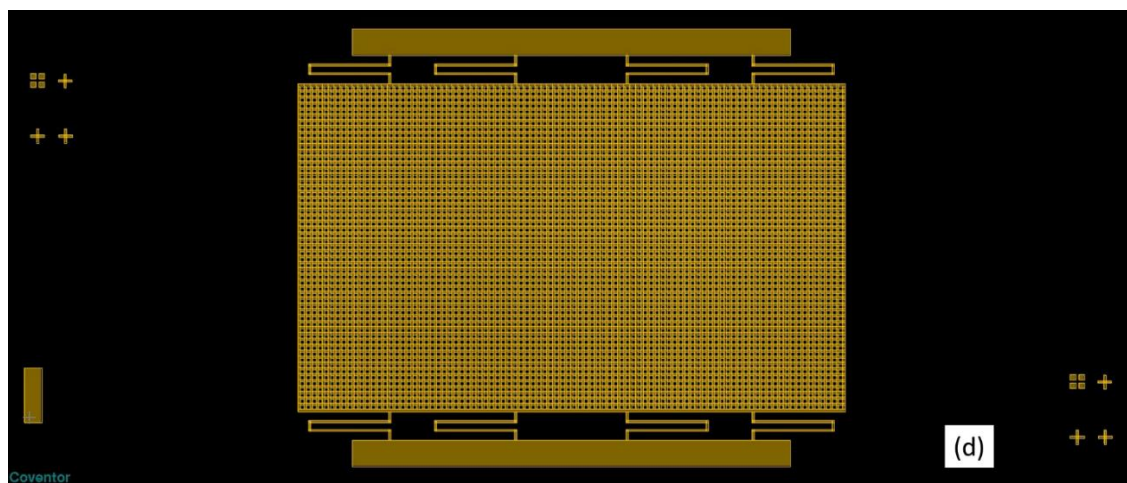
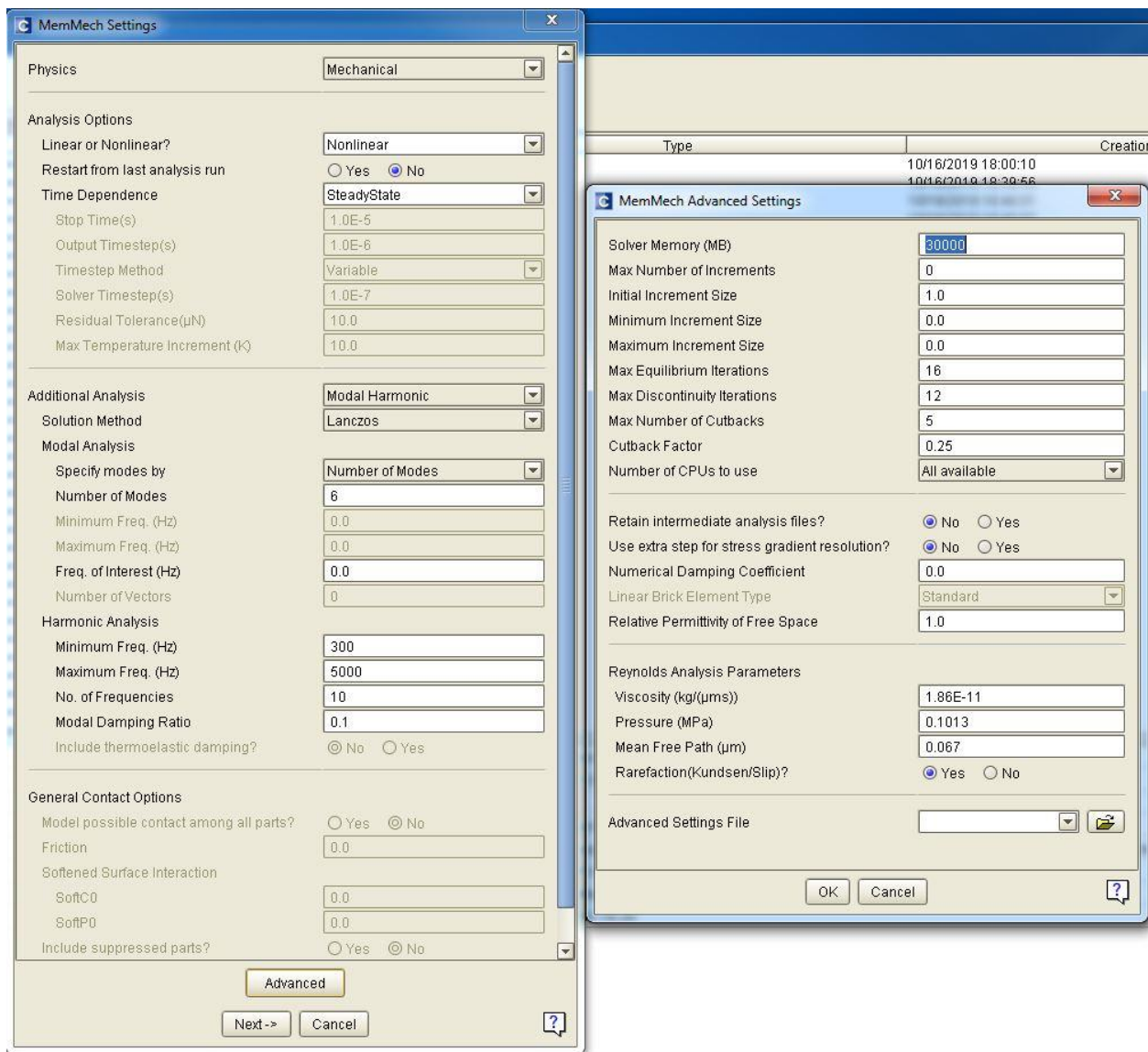


Figure D.1: Mask layout designs for the triboelectric energy harvester. (a) Bottom electrode mask (b) Teflon layer mask (c) Anchor mask (d) Anchor\_spring\_proofmass mask (e) All of the masks combined.

# Appendix E: Coventorware™ settings for the triboelectric energy harvester performance simulation

The triboelectric energy harvester model was simulated in Coventorware™ using the MemMech simulator for modal harmonic analysis and stress analysis. Following are the simulation settings for the simulations:



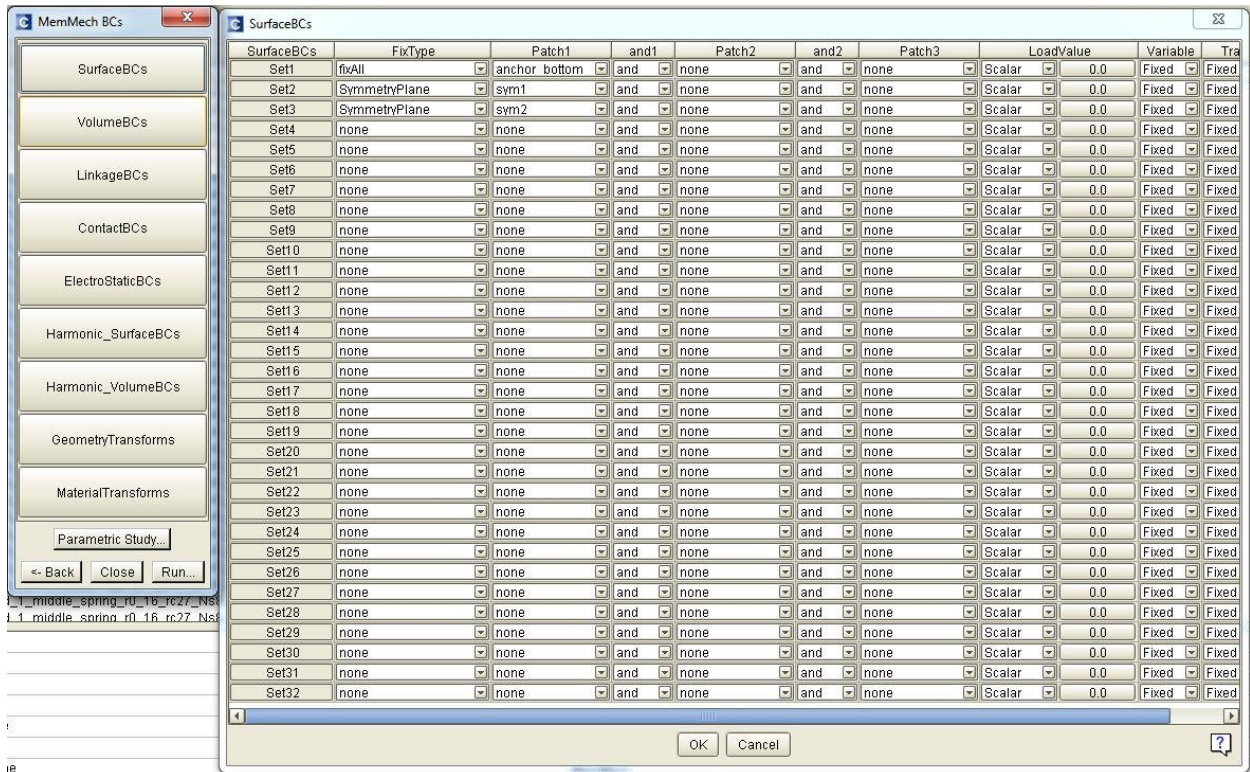


Figure E.1: Coventorware™ settings for the triboelectric energy harvester modal harmonic analysis.



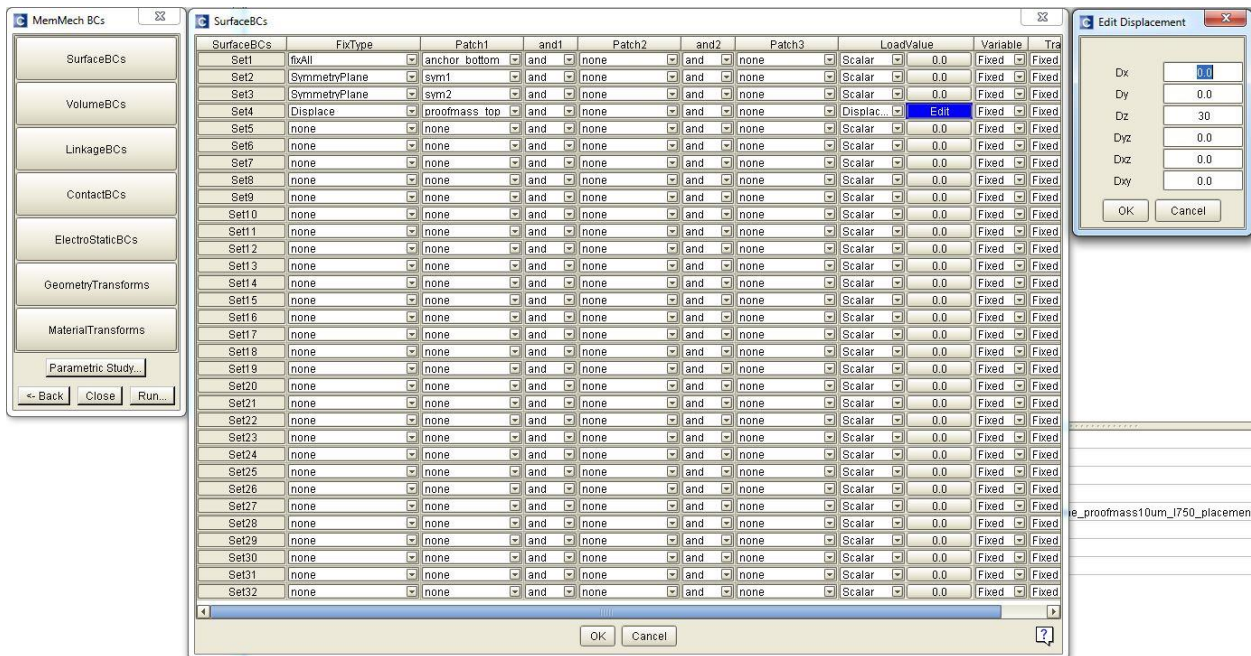
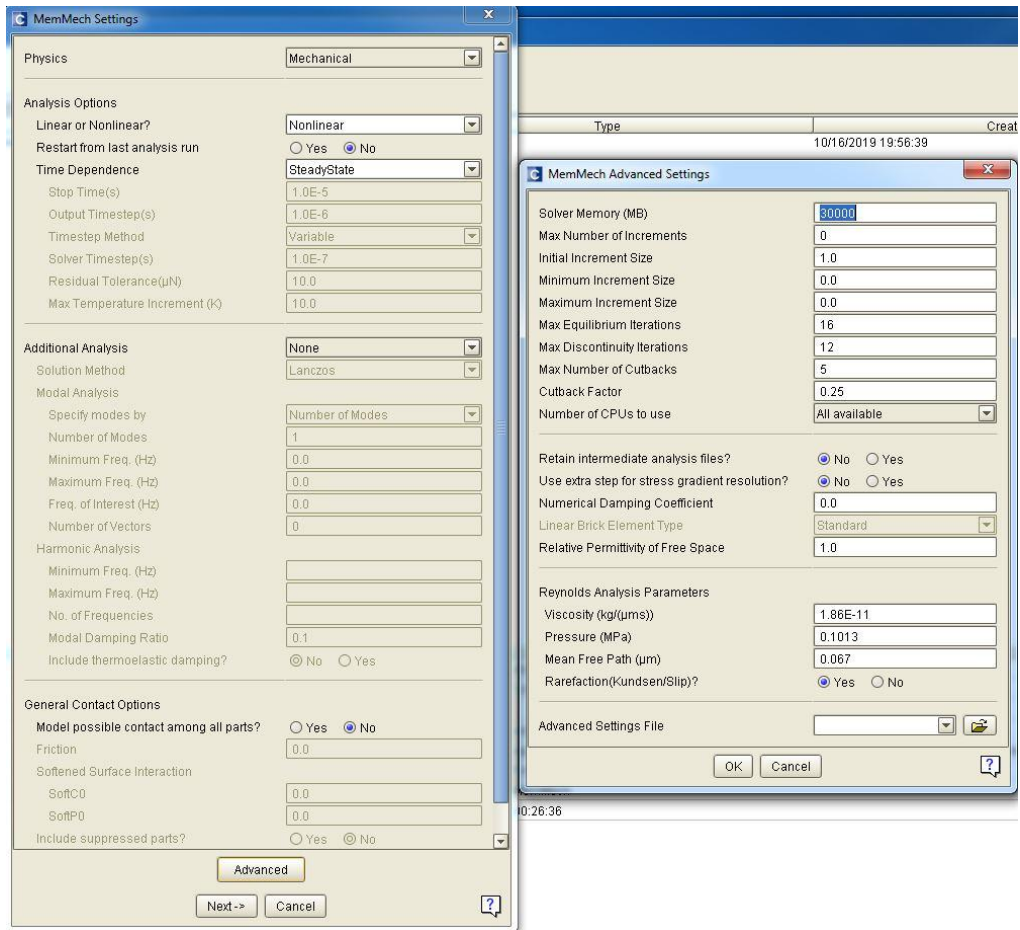


Figure E.2: Coventorware™ settings for the triboelectric energy harvester stress analysis.

## References

- [1] Z. L. Wang, T. Jiang, L. Xu, Piezoelectric nanogenerators based on ZnO nanowire arrays, *Science* 312 (2006) 242-246.
- [2] F. –R. Fan, Z. –Q. Tian, Z. L. Wang, Flexible triboelectric nanogenerator!, *Nano Energy* 1 (2012) 328-334.
- [3] Z. L. Wang, Triboelectric nanogenerators as new energy technology and self-powered sensors – principles, problems and perspectives, *Faraday Discuss. R. Soc. Chem.* 176 (2014) 447-458.
- [4] J.C. Maxwell. *Philos. Mag. J. Sci., Fourth series*, Edinburg and Dublin London, 1870.
- [5] Z. L. Wang, T. Jiang, L. Xu, Toward the blue energy dream by triboelectric nanogenerator networks, *Nano Energy* 39 (2017) 9-23.
- [6] W. Ren, B. Peng, J. Shen, Y. Li, Y. Yu, Study on vibration characteristics and human riding comfort of a special equipment car, *Journal of Sens.* 2018 (2018) 1-8, Article ID 7140610
- [7] S. Roundy, P. K. Wright, J. Rabaey, A Study of Low Level Vibrations as a Power Source for Wireless Sensor Nodes, *Comput Commun.* 26 (2003) 1131–1144.
- [8] S. Lee, B. Youn, A new piezoelectric energy harvesting design concept: multimodal energy harvesting skin, *IEEE Trans. Ultrason. Ferroelectr. Freq. Control* 58 (2011) 629-645.
- [9] Q. Zheng, B. Shi, F. Fan, X. Wang, L. Yan, W. Yuan, S. Wang, H. Liu, Z. Li, Z. L. Wang, In vivo powering of pacemaker by breathing-driven implanted triboelectric nanogenerator, *Adv. Mater.* 26 (2014) 5851-5856.
- [10] M. A. Karami, D. J. Inman, Powering pacemakers from heartbeat vibrations using linear and nonlinear energy harvesters, *Appl. Phys. Lett.* 100 (2012) 042901.
- [11] G. Hwang, H. Park, J. Lee, S. Oh, K. Park, M. Byun, G. Ahn, C. K. Jeong, K. No, H. Kwon, S. Lee, B. Joung, K. J. Lee, Self-powered cardiac pacemaker enabled by flexible single crystalline PMN-PT piezoelectric energy harvester, *Adv. Mater.* 26 (2014) 4880-4887.

- [12] M. L. Seol, J. W. Han, D. I. Moon, M. Meyyappan, Triboelectric nanogenerator for Mars environment, *Nano Energy* 29 (2017) 238-244.
- [13] Z. Zhao, X. Pu, C. Du, L. Li, C. Jiang, W. Hu, Z. L. Wang, Freestanding flag-type triboelectric nanogenerator for harvesting high-altitude wind energy from arbitrary directions, *ACS Nano* 10 (2016) 1780-1787.
- [14] Y. Yang, G. Zhu, H. Zhang, J. Chen, X. Zhong, Z. -H. Lin, Y. Su, P. Bai, X. Wen, Z. L. Wang, Triboelectric nanogenerator for harvesting wind energy and as self-powered wind vector sensor system, *ACS Nano* 7 (2013) 9461-9468.
- [15] X. Li, J. Tao, J. Zhu, C. Pan, A nanowire based triboelectric nanogenerator for harvesting water wave energy and its applications, *APL Mater.* 5 (2017) 074104.
- [16] J. Chen, J. Yang, Z. Li, X. Fan, Y. Zi, Q. Jing, H. Guo, Z. Wen, K. C. Pradel, S. Niu, Z. L. Wang, Networks of triboelectric nanogenerators for harvesting water wave energy: a potential approach toward blue energy, *ACS Nano* 9 (2015) 3324-3331.
- [17] G. Zhu, Y. Su, P. Bai, J. Chen, Q. Jing, W. yang, Z. L. Wang, Harvesting water wave energy by asymmetric screening of electrostatic charges on a nanostructured hydrophobic thin-film surface, *ACS Nano* 8 (2014) 6031-6037.
- [18] X. Wen, W. Yang, Q. Jing, Z. L. Wang, Harvesting broadband kinetic impact energy from mechanical triggering/vibration and water waves, *ACS Nano* 8 (2014) 7405-7412.
- [19] W. Yang, J. Chen, Q. S. Jing, J. Yang, X. N. Wen, Y. J. Su, G. Zhu, P. Bai, Z. L. Wang, 3D stack integrated triboelectric nanogenerator for harvesting vibration energy, *Adv. Funct. Mater.* 24 (2014) 4090.
- [20] J. Yang, J. Chen, Y. Liu, W. Q. Yang, Y. J. Su, Z. L. Wang, Triboelectrification-based organic film nanogenerator for acoustic energy harvesting and self-powered active acoustic sensing, *ACS Nano* 8 (2014) 2649.

- [21] A. F. Yu, M. Song, Y. Zhang, Y. Zhang, L. B. Chen, J. Y. Zhai, Z. L. Wang, Self-powered acoustic source locator in underwater environment based on organic film triboelectric nanogenerator, *Nano Res.* 8 (2014) 765-773.
- [22] X. Fan, J. Chen, J. Yang, P. Bai, Z. Li, Z. L. Wang, Ultrathin, rollable, paper-based triboelectric nanogenerator for acoustic energy harvesting and self-powered sound recording, *ACS Nano* 9 (2015) 4236-4243.
- [23] L. Dhakar, P. Pitchappa, F. E. H. Tay, C. Lee, An intelligent skin based self-powered finger motion sensor integrated with triboelectric nanogenerator, *Nano Energy* 19 (2016) 532-540.
- [24] J. Zhong, Y. Zhang, Q. Zhong, Q. Hu, Z. L. Wang, J. Zhou, Fiber-based generator for wearable electronics and mobile medication, *ACS Nano* 8 (2014) 6273-6280.
- [25] W. Q. Yang, J. Chen, X. N. Wen, Q. S. Jing, J. Yang, Y. J. Su, G. Zhu, W. Z. Wu, Z. L. Wang, Triboelectrification based motion sensor for human-machine interfacing, *ACS Appl. Mater. Interfaces*, 6 (2014) 7479.
- [26] W. Q. Yang, J. Chen, G. Zhu, J. Yang, P. Bai, Y. J. Su, Q. S. Jing, Z. L. Wang, Harvesting Energy from the Natural Vibration of Human Walking, *ACS Nano* 7 (2013) 11317.
- [27] J. Qian, D. -S. Kim, D. -W. Lee, On-vehicle triboelectric nanogenerator enabled self-powered sensor for tire pressure monitoring, *nano Energy* 49 (2018) 126-136.
- [28] W. Wu, X. Cao, J. Zou, Y. Ma, X. Wu, C. Sun, M. Li, N. Wang, Z. Wang, L. Zhang, Triboelectric nanogenerator boosts smart green tires, *Adv. Funct. Mater.* 29 (2019) 1806331.
- [29] T. Guo, G. Liu, Y. Pang, B. Wu, F. Xi, J. Zhao, T. Bu, X. Fu, X. Li, C. Zhang, Z. L. Wang, Compressible hexagonal-structured triboelectric nanogenerators for harvesting tire rotation energy, *Extreme Mech. Lett.* 8 (2018) 1-8.
- [30] H. M. A. Hamid, Z. Celik-Butler, Li-ZnO nanowire carpet as a micro-newton force sensor with nanometer resolution, in: *Proceedings of IEEE Sensors Conf.*, Glasgow, (2017).

- [31] B. P. Nabar, Z. Çelik-Butler, D. P. Butler, Self-powered tactile pressure sensors using ordered crystalline ZnO nanorods on flexible substrates toward robotic skin and garments, *IEEE Sens. J.* 15 (2015) 63-70.
- [32] Q. Shi, H. Wang, T. Wang, C. Lee, Self-powered liquid triboelectric microfluidic sensor for pressure sensing and finger motion monitoring applications. *Nano Energy* 30 (2016) 450–459.
- [33] L. Dhakar, S. Gudla, X. Shan, Z. Wang, F. E. H. Tay, C. –H. Heng, C. Lee, Large Scale Triboelectric Nanogenerator and Self-Powered Pressure Sensor Array Using Low Cost Roll-to-Roll UV Embossing. *Sci. Rep.* 6 (2016) 22253.
- [34] Y. Yang, H. Zhang, Z. –H. Lin, Y. S. Zhou, Q. Jing, Y. Su, J. Yang, J. Chen, C. Hu, Z. L. Wang, Human Skin Based Triboelectric Nanogenerators for Harvesting Biomechanical Energy and as Self-Powered Active Tactile Sensor System. *ACS Nano* 7 (2013) 9213–9222.
- [35] M. Xu, P. Wang, Y. –C. Wang, S. L. Zhang, A. C. Wang, C. Zhang, Z. Wang, X. Pan, Z. L. Wang, A soft and robust spring based triboelectric nanogenerator for harvesting arbitrary directional vibration energy and self-powered vibration sensing, *Adv. Energy Mater.* 8 (2018) 1702432.
- [36] H. Zhang, Y. Yang, Y. Su, J. Chen, K. Adams, S. Lee, C. Hu, Z. L. Wang, Triboelectric nanogenerator for harvesting vibration energy in full space and as self-powered acceleration sensor, *Adv. Funct. Mater.* 24 (2014) 1401-1407.
- [37] H. Wang, Z. Xiang, P. Giorgia, X. Mu, Y. Yang, Z. L. Wang, C. Lee, Triboelectric liquid volume sensor for self-powered lab-on-chip applications. *Nano Energy* 23 (2016) 80–88.
- [38] S. B. Jeon, M. –L. Seol, D. Kim, S. –J. Park, Y. –K. Choi, Self-Powered Ion Concentration Sensor with Triboelectricity from Liquid-Solid Contact Electrification. *Adv. Electronic Mater.* 2 (2016), 1600006.
- [39] X. Pu, W. Hu, Z. L. Wang, Toward wearable self-charging power systems: The integration of energy harvesting and storage devices, *Small* 14 (2017) 1702817.

- [40] X. Pu, L. Li, H. Song, C. Du, Z. Zhao, C. Jiang, G. Cao, W. Hu, Z. L. Wang, A self-charging power unit by integration of a textile triboelectric nanogenerator and a flexible lithium-ion battery for wearable electronics, *Adv. Mater.* 27 (2015) 2472-2478.
- [41] S. J. Roundy, Energy scavenging for wireless sensor nodes with a focus on vibration to electricity conversion, PhD Thesis, UC Berkeley, 2003.
- [42] P. Wang, K. Tanaka, S. Sugiyama, X. Dai, X. Zhao, J. Liu, A micro electromagnetic low level vibration energy harvester based on MEMS technology, *Microsys. Technol.*, 15 (2009) 941–951.
- [43] I. Sari, T. Balkan, H. Kulah, An electromagnetic micro power generator for wideband environmental vibrations, *Sensors and actuators A* 146 (2008) 405-413.
- [44] D. Hoffmann, B. Folkmer, Y. Manoli, Fabrication, characterization and modeling of electrostatic micro-generators, *J. Micromech. Microeng.* 19 (2009) 1-11.
- [45] X. Sheng, Y. Wei, J. Liu, R. Yang, Z. L. Wang, Integrated multilayer nanogenerator fabricated using paired nanotip-to-nanowire brushes, *Nano lett.* 8 (2008) 4027-4032.
- [46] Z. -H. Lin, G. Cheng, S. Lee, K. C. Pradel, Z. L. Wang, Harvesting water drop energy by a sequential contact-electrification and electrostatic-induction process, *Adv. mater.* 26 (2014) 4690-4696.
- [47] U. G. Musa, S. D. Cezan, B. Baytekin, H. T. Baytekin, The charging effects in contact-separation electrification, *Sci. Rep.* 8 (2018) 2472.
- [48] X. Pu, M. Liu, X. Chen, J. Sun, C. Du, Y. Zhang, J. Zhai, W. Hu, Z. L. Wang, Ultrastretchable transparent triboelectric nanogenerator as electronic skin for biomedical energy harvesting and tactile sensing, *Sci. Adv.* 3 (2017) e1700015.
- [49] J. Chen, G. Zhu, W. Yang, Q. Jing, P. Bai, Y. Yang, T. -C. Hou, Z. L. Wang, Harmonic-resonator-based triboelectric nanogenerator as a sustainable power source and a self-powered active vibration sensor, *Adv. Mater.* 25 (2013) 6094-6099.
- [50] [https://en.wikipedia.org/wiki/Zinc\\_oxide](https://en.wikipedia.org/wiki/Zinc_oxide), Accessed on February 22<sup>nd</sup>, 2020.

- [51] H. Morkoc, U. Ozgur, Zinc oxide: fundamentals, materials and device technology, 2009, ISBN: 978-3-527-40813-9
- [52] Y. Gao, Z. L. Wang, Electrostatic potential in a bent piezoelectric nanowire. The fundamental theory of nanogenerator and nanopiezotronics, *Nano lett.* 7 (2007) 2499-2505.
- [53] Z. L. Wang, Nanostructures of ZnO, *Materialstoday*, 7 (2004) 26-33.
- [54] Z. L. Wang, X. Wang, J. Song, J. Liu, and Y. Gao, Piezoelectric nanogenerators for self-powered nanodevices, *IEEE Pervas. Comput.*, 7 (2008) 49-55.
- [55] C. Liu, A. Yu, M. Peng, M. Song, W. Liu, Y. Zhang, J. Jhai, Improvement in the piezoelectric performance of a ZnO nanogenerator by a combination of chemical doping and interfacial modification, *J. Phys. Chem.*, 2016, 120, 6971-6977
- [56] K. C. Pradel, W. Wu, Y. Zhou, X. Wen, Y. Ding, Z. L. Wang, Piezotronic Effect in Solution-Grown p-Type ZnO Nanowires and Films, *Nano Lett.* 2013, 13, 2647–2653
- [57] X. Xue, Y. Nie, B. He, L. Xing, Y. Zhang, Z. L. Wang, Surface free-carrier screening effect on the output of a ZnO nanowire nanogenerator and its potential as a self-powered active gas sensor, *Nanotechnology* 24 (2013) 225501
- [58] B. P. Nabar, Z. Celik-Butler, D. P. Butler, Piezoelectric ZnO nanorod carpet as a NEMS vibrational energy harvester, *Nano Energy*, 10 (2014) 71-82.
- [59] Y. Li, Z. Celik-Butler, D. P. Butler, An integrated piezoelectric zinc oxide nanowire micro-energy harvester, *Nano Energy* 26 (2016) 456-465.
- [60] P. Parthangal, R. Cavicchi, M. Zachariah, A universal approach to electrically connecting nanowire arrays using nanoparticles application to a novel gas sensor architecture, *Nanotechnology* 17 (2006) 3786–3790.
- [61] J. X. Wang, X. W. Sun, Y. Yang, H. Huang, Y. C. Lee, O. K. Tan, L. Vayssieres, Hydrothermally grown oriented ZnO nanorod arrays for gas sensing applications, *Nanotechnology* 17 (2006) 4995–4998.

- [62] M. Willander, K. Khun, H. Ibupoto, Metal oxide nanosensors using polymeric membranes, enzymes and antibody receptors as ion and molecular recognition elements, *Sensors* 14 (2014) 8605–8632.
- [63] S. M. Usman Ali, O. Nur, M. Willander, B. Danielsson, A fast and sensitive potentiometric glucose microsensor based on glucose oxidase coated ZnO nanowires grown on a thin silver wire, *Sens. Actuators B* 145 (2010) 869–874.
- [64] A. Zainelabdin, S. Zaman, G. Amin, O. Nur, M. Willander, Stable white light electroluminescence from highly flexible polymer/ZnO nanorods hybrid heterojunction grown at 50 °C, *Nanoscale Res. Lett.* 5 (2010) 1442–1448.
- [65] F. Beyeler, A. Neild, S. Oberti, D. J. Bell, Y. Sun, J. Dual, B. J. Nelson, Monolithically fabricated microgripper with integrated force sensor for manipulating microobjects and biological cells aligned in an ultrasonic field, *J. Microelectromech. Syst.* 16 (2015) 7–15.
- [66] X. Li, C. Zhao, X. Liu, A paper-based microfluidic biosensor integrating zinc oxide nanowires for electrochemical glucose detection, *Microsystems and Nanoengineering* 1 (2015) 15014.
- [67] A. D. Astin, Finger force capability: measurement and prediction using anthropomorphic and myoelectric measures, M.S. thesis, Dept. Ind. Syst. Eng., Virginia Polytechnic Inst. State Univ., Blacksburg, VA, USA, 1999.
- [68] K. Y. Lee, B. Kumar, J. Seo, K. Kim, J. I. Sohn, S. N. Cha, D. Choi, Z. L. Wang, S. Kim, P-type polymer-hybridized high-performance piezoelectric nanogenerators, *Nano Lett.* 12 (2012) 1959–1964.
- [69] J. I. Sohn, S. N. Cha, B. G. Song, S. Lee, S. M. Kim, J. Ku, H. J. Kim, Y. J. Park, B. L. Choi, Z. L. Wang, J. M. Kim, K. Kim, Engineering of efficiency limiting free carriers and an interfacial energy barrier for an enhancing piezoelectric generation, *Energy Environ. Sci.* 6 (2013) 97–104.
- [70] S. Shin, Y. Kim, M. H. Lee, J. Jung, J. H. Seol, J. Nah, Lithium-doped zinc oxide nanowires-polymer composite for high performance flexible piezoelectric nanogenerator, *ACS Nano* 8 (2014) 10844–10850.



- [71] Y. C. Yang, C. Song, X. H. Wang, F. Zeng, F. Pan, Cr-substitution-induced ferroelectric and improved piezoelectric properties of  $Zn_{1-x}Cr_xO$  films, *J. Appl. Phys.* 103 (2008) 074107.
- [72] X. B. Wang, C. Song, D. M. Li, K. W. Geng, F. Zeng, F. Pan, The influence of different doping elements on microstructures, piezoelectric coefficient and resistivity of sputtered ZnO film, *Appl. Surf. Sci.* 253 (2006) 1639-1643.
- [73] D. Zhu, T. Hu, Y. Zhao, W. Zang, L. Xing, X. Xue, High performance self-powered/active humidity sensing of Fe-doped ZnO nanoarray nanogenerator, *Sens. Actuators B* 213 (2015) 382-389.
- [74] C. Hsu, I. Su, T. Hsueh, Sulfur-doped-ZnO-nanospire-based transparent flexible nanogenerator self-powered by environmental vibration, *RSC Adv.* 5 (2015) 34019-34026.
- [75] T. Zhao, Y. Fu, Y. Zhao, L. Xing, X. Xue, Ga-doped ZnO nanowire nanogenerator as self-powered/active humidity sensor with high sensitivity and fast response, *J. Alloys. Compd.* 648 (2015) 571-576.
- [76] S. Lee, J. Lee, W. Ko, S. Cha, J. Sohn, J. Kim, J. Park, Y. Park, J. Hong, Solution-processed Ag-doped ZnO nanowires grown on flexible polyester for nanogenerator applications, *Nanoscale* 5 (2013) 9609.
- [77] Y. Chang, J. Chen, T. Yang, C. Huang, C. Chiu, P. Yeh, W. Wu, Excellent piezoelectric and electrical properties of lithium-doped ZnO nanowires for nanogenerator applications, *Nano Energy* 8 (2014) 291-296.
- [78] J. Lee, S. Cha, J. Kim, H. Nam, S. Lee, W. Ko, K. L. Wang, J. Park, J. Hong, P-type conduction characteristics of lithium-doped ZnO nanowires, *Adv. Mater.* 23 (2011) 4183-4187.
- [79] G. Liu, M. C. Tam, L. Hu, K. El-Rayes, Q. Guo, J. Yang, N. Mrad, D. Ban, Optical and piezoelectric properties of p-type ZnO nanowires on transparent flexible substrate for energy harvesting, *Proc. SPIE 9202, Photonics Applications for Aviation, Aerospace, Commercial, and Harsh Environments V*, 92020H (2014); <http://dx.doi.org/10.1117/12.2061237>

- [80] S. Chawla, K. Jayanthi, R. K. Kotnala, Room temperature ferromagnetism in Li-doped p-type luminescent ZnO nanorods, *Phys. Rev. B* 79 (2009) 125204.
- [81] L. Wang, N. C. Giles, Temperature dependence of the free-exciton transition energy in zinc oxide by photoluminescence excitation spectroscopy, *J. Appl. Phys.* 94 (2003) 973.
- [82] J. Yin, G. Zhang, H. Liu, J. Liang, Hydrothermal fabrication and ferroelectric behavior of lithium-doped zinc oxide nanoflakes, *Sci. Adv. Mater.* 5 (2013) 1139-1149.
- [83] J. N. Dhananjay, S. B. Krupanidhi, Off-centered polarization and ferroelectric phase transition in Li-doped ZnO thin films grown by pulsed-laser ablation, *J. Appl. Phys.* 101 (2007) 104104.
- [84] Y. C. Yang, C. Song, X. H. Wang, F. Zeng, F. Pan, Giant piezoelectric  $d_{33}$  coefficient in ferroelectric vanadium doped ZnO films, *Appl. Phys. Lett.* 92 (2008) 012907.
- [85] T. S. Bjorheim, S. Erdal, K. M. Johansen, K. E. Knutsen, T. Norby, H and Li related defects in ZnO and their effect on electrical properties, *J. Phys. Chem. C* 116 (2012) 23764-23772.
- [86] G. Liu, E. A. Rahman, D. Ban, Performance optimization of p-n homojunction nanowire-based piezoelectric nanogenerators through control of doping concentration, *J. Appl. Phys.* 118 (2015) 094307.
- [87] C. Lizandara-Pueyo, S. Dilger, M. R. Wagner, M. Gerigk, A. Hoffmann, S. Polarz, Li-doped ZnO nanorods with single crystal quality-non-classical crystallization and self-assembly into mesoporous materials, *CrystEngComm.* 16 (2014) 1525-1531.
- [88] A. Janotti, C. G. V. D. Walle, Fundamentals of zinc oxide as a semiconductor, *Rep. Prog. Phys.* 72 (2009) 126501.
- [89] R. Panat, J. Wang, E. Parks, Effect of triboelectric charging between polymer surfaces in manufacturing and test of integrated circuit packages, *IEEE Trans. Compon. Packag. Manuf. Technol.* 4 (2014) 943-946.
- [90] <https://www.alamy.com/static-electricity-on-comb-attracts-pieces-of-paper-image1418192.html>, accessed on February 23<sup>rd</sup>, 2020.
- [91] [http://www.nexentire.com/webzine/201712/en/content\\_08.html](http://www.nexentire.com/webzine/201712/en/content_08.html), accessed on February 23<sup>rd</sup>, 2020.

- [92] K. A. Winters, B. C. Roberts, M. McGrath, M. McClell, The impact of triboelectrification on the Ares I-X and considerations for other launch vehicles, 15th Conference on Aviation, Range, and Aerospace Metrology, Los Angeles. USA, August 2011.
- [93] F. Galembeck, T. A. L. Burgo, L. B. S. Balestrin, R. F. Gouveia, C. A. Silva, A. Galembeck, Friction, tribochemistry and triboelectricity: Recent progress and perspectives, *RSC Adv.* 4 (2014) 64280.
- [94] <https://blog.csiro.au/bushfire-basics/>, accessed on February 23<sup>rd</sup>, 2020.
- [95] [https://en.wikipedia.org/wiki/Static\\_discharger](https://en.wikipedia.org/wiki/Static_discharger), accessed on February 23<sup>rd</sup>, 2020.
- [96] <https://www.alamy.com/stock-photo-electronic-integrated-circuit-ic-on-a-computer-pcb-after-suffering-30453914.html>, accessed on February 23<sup>rd</sup>, 2020.
- [97] Z. L. Wang, “Triboelectric nanogenerators as new energy technology for self-powered systems and as active mechanical and chemical sensors,” *ACS Nano*, 7 (2013) 9533-9557.
- [98] <https://www.keyence.com/ss/products/static/resource/feature/property.jsp>, accessed on February 23<sup>rd</sup>, 2020.
- [99] Z. L. Wang, J. Chen, L. Lin, Progress in triboelectric nanogenerators as a new energy technology and self-powered sensors, *Energy Environ. Sci.* 8 (2015) 2250.
- [100] S. Niu, S. Wang, L. Lin, Y. Liu, Y. S. Zhou, Y. Hu, Z. L. Wang, Theoretical study of contact mode triboelectric nanogenerators as an effective power source, *Energy Environ. Sci.* 6 (2013) 3576-3583.
- [101] S. L. Zhang, Y. -C. Lai, X. He, R. Liu, Y. Zi, Z. L. Wang, Auxetic foam-nased contact mode triboelectric nanogenerator with highly sensitive self-powered strain sensing capabilities to monitor human body movement, *Adv. Funct. Mater.* 27 (2017) 1606695.
- [102] C. Jin, D. S. Kia, M. Jones, S. Towfighian, On the contact behavior of micro-/nano-structure interface used in vertical-contact-mode triboelectric nanogenerators, *nano Energy* 27 (2016) 68-77.

- [103] S.-B. Jeon, D. Kim, M. -L. Seol, S. -J. Park, Y. -K. Choi, 3-Dimensional broadband energy harvester based on internal hydrodynamic oscillation with a package structure, *Nano Energy* 17 (2015) 82–90.
- [104] L. Dhakar, F. E. H. Tay, C. Lee, Development of a broadband triboelectric energy harvester with SU-8 micropillars, *J. Microelectromech. Syst.* 24, 91–99 (2015).
- [105] S. Niu, Y. Liu, S. Wang, L. Lin, Y. S. Zhou, Y. Hu, Z. L. Wang, Theory of sliding-mode triboelectric nanogenerators, *Adv. Mater.* 25 (2013) 6184-6193.
- [106] S. Niu, S. Wang, Y. Liu, Y. S. Zhou, L. Lin, Y. Hu, K. C. Pradel, Z. L. Wang, A theoretical study of grating structured triboelectric nanogenerators, *Energy Environ. Sci.* 7 (2014) 2339.
- [107] S. Wang, L. Lin, Y. Xie, Q. Jing, S. Niu, Z. L. Wang, Sliding-triboelectric nanogenerators based on in-plane charge separation mechanism, *Nano. Lett.* 13 (2013) 2226-2233.
- [108] G. Zhu, Y. S. Zhou, P. Bai, X. S. Meng, Q. Jing, J. Chen, Z. L. Wang, A shape-adaptive thin-film-based approach for 50% high-efficiency energy generation through micro-grating sliding electrification, *Adv. Mater.* 26 (2014) 3788-3796.
- [109] S. Niu, Y. Liu, S. Wang, L. Lin, Y. S. Zhou, Y. Hu, Z. L. Wang, theoretical investigation and structural optimization of single-electrode triboelectric nanogenerators, *Adv. Funct. Mater.* 24 (2014) 3332-3340.
- [110] S. Wang, Y. Xie, S. Niu, L. Lin, Z. L. Wang, Freestanding triboelectric-layer-based nanogenerators for harvesting energy from a moving object or human motion in contact and non-contact modes, *Adv. Mater.* 26 (2014) 2818-2824.
- [111] J. Peng, S. D. Kang, G. J. Snyder, Optimization principles and the figure of merit for triboelectric generators, *Sci. Adv.* 3 (2017) eaap8576.
- [112] Y. Yang, Y. S. Zhou, H. Zhang, Y. Liu, S. Lee, Z. L. Wang, A single-electrode based triboelectric nanogenerator as self-powered tracking system, *Adv. Mater* 25 (2013) 6594.

- [113] Y. Yang, H. Zhang, J. Chen, Q. Jing, Y. S. Zhou, X. Wen, Z. L. Wang, Single-electrode-based sliding triboelectric nanogenerator for self-powered displacement vector sensor system, *ACS Nano* 7 (2013) 7342.
- [114] J. Chen, H. Guo, P. Ding, R. Pan, W. Wang, W. Xuan, X. Wang, H. Jin, S. Dong, J. Luo, Transparent triboelectric generators based on glass and polydimethylsiloxane, *Nano Energy* 30 (2016) 235-241.
- [115] V. Wowk, A brief tutorial on machine vibration, [https://www.machinedyn.com/docs/machine\\_vibration\\_tutorial.pdf](https://www.machinedyn.com/docs/machine_vibration_tutorial.pdf) (accessed 2nd February 2020).
- [116] T. J. Gordon, Z. Bareket, Vibration transmission from road surface features – vehicle measurement and detection, The University of Michigan Transportation Research Institute (2007).
- [117] Y. Xie, S. Wang, S. Niu, L. Lin, Q. Jing, J. Yang, Z. Wu, Z. L. Wang, Grating-structured freestanding triboelectric-layer nanogenerator for harvesting mechanical energy at 85% total conversion efficiency, *Adv. Mater.* 26 (2014) 6599-6607.
- [118] J. Gubbi, R. Buyya, S. Marusic, M. Palaniswami, Internet of things (IoT): A vision, architectural elements, and future directions, *Future Gener. Comput. Syst.* 29 (2013) 1645-1660.
- [119] H. Liu, C. Lee, T. Kobayashi, C. J. Tay, C. Quan, Investigation of a MEMS piezoelectric energy harvester system with a frequency-widened-bandwidth mechanism introduced by mechanical stoppers, *Smart mater.* 21 (2012) 035005.
- [120] T. Maeguchi, A. Masuda, H. Katsumura, H. Kagata, H. Okumura, Band widening of piezoelectric vibration energy harvesters by utilizing mechanical stoppers and magnets, *J. Phy.: Conf. Ser.* 660 (2015) 012099.
- [121] M. Bao, H. yang, Y. Sun, P. J. French, Modified Reynold's equation and analytical analysis of squeeze film air damping of perforated structures, *J. Micromech. Microeng.* 13 (2003) 795-800.
- [122] M. Bao, H. Yang, Squeeze film air damping in MEMS, *Sens. Actuators A* 136 (2007) 3-27.
- [123] A. K. Pandey, R. Pratap, Effect of flexural modes on squeeze film damping in MEMS cantilever resonators, *J. Micromech. Microeng.* 17 (2007) 2475-2484.

- [124] M. –L. Seol, S. –H. Lee, J. –W. Han, D. Kim, G. –H. Cho, Y. –K. Choi, Impact of contact pressure on output voltage of triboelectric nanogenerator based on deformation of interfacial structures, *Nano Energy* 17 (2015) 63-71.
- [125] Y. Zi, S. Niu, J. Wang, Z. Wen, W. Tang, Z. L. Wang, Standards and figure-of-merits for quantifying the performance of triboelectric nanogenerators, *Nat. Commun.* 6 (2015) 8376.
- [126] Y. Zhu, B. yang, J. Liu, X. Wang, L. Wang, X. Chen, C. Yang, A flexible and biocompatible triboelectric nanogenerator with tunable internal resistance for powering wearable devices, *Sci. Rep.* 6 (2016) 22233.
- [127] H. M. A. Hamid, Z. Celik-Butler, ZnO nano-sensors and nano-energy harvesters (invited), in: *Proceedings of IEEE Sensors Conf., Glasgow, (2017)*.
- [128] H. M. A. Hamid, Z. Celik-Butler, Characterization and Performance Analysis of Li-Doped ZnO Nanowire as a Nano-Sensor and Nano-Energy Harvesting Element, *Nano Energy* 50 (2018) 159-168.
- [129] M. C. Akgun, A. Afal, H. E. Unalan, Hydrothermal zinc oxide nanowire growth with different zinc salts, *J. Mater. Res.* 1 (2012) 1-7.
- [130] S. Baruah and J. Dutta. Hydrothermal growth of ZnO nanostructures. *Science and Technology of Advanced Materials* 10(1), pp. 013001. 2009.
- [131] L. N. Demianets, D. V. Kostomarov, Mechanism of zinc oxide single crystal growth under hydrothermal conditions, *Ann. Chim. Sci. Mat.* 26 (2001) 1139-1149.
- [132] K. Pradel, W. Wu, Y. Zhou, X. Wen, Y. Ding, Z. L. Wang, Piezotronic effect in solution-grown p-type ZnO nanowires and films, *Nano Lett.* 13 (2013) 2647-2653.
- [133] C. Zandalazini, M. Villafuerte, M. Oliva, S. P. Heluani, Aluminum as a catalyst for ZnO nanostructures growth, *arXiv:1501.01594* , accessed 12th April 2018.
- [134] B. H. Kim, J. W. Kwon, Metal catalyst for low-temperature growth of controlled zinc oxide nanowires on arbitrary substrates, *Sci. Rep.* 4 (2014) 4379.

- [135] F. Khan, S. Baek, J. H. Kim, Dependence of performance of Si nanowire solar cells on geometry of the nanowires, *Sci. World J.* 2014, <http://dx.doi.org/10.1155/2014/358408>.
- [136] H. Qi, E. R. Glaser, J. D. Caldwell, S. M. Prokes, Growth of vertically aligned ZnO nanowire arrays using bilayered metal catalysts, *J. Nanomater.* 2012. doi:10.1155/2012/260687
- [137] W. Hwang, J. Choi, T. H. Kim, J. Sung, J. Myoung, D. Choi, B. Sohn, S. S. Lee, D. H. Kim, C. Park, Control of the area density of vertically grown ZnO nanowires by blending PS-b-P4VP and PS-b-PAA copolymer micelles, *Chem. Mater.* 20 (2008) 6041-6047.
- [138] X. Wang, J. Song, C. J. Summer, J. H. Ryou, P. Li, R. D. Dupuis, Z. L. Wang, Density-controlled growth of aligned ZnO nanowires sharing a common contact: A simple, low cost, and mask-free technique for large-scale applications, *J. Phys. Chem. B* 110 (2006) 7720-7724.
- [139] S. Najjar, D. Talaga, Y. Coffinier, S. Szunerits, R. Boukherroub, L. Servant, M.I. Couzi, S. Bonhommeau, Characterization of single transition metal oxide nanorods by combining atomic force microscopy and polarized micro-Raman spectroscopy, *Chemical Phys Letters*, 514 (2011) 128-133.
- [140] R. Kirste, Y. Aksu, M. R. Wagner, S. Khachadorian, S. Jana, M. Driess, C. Thomsen, A. Hoffmann, Raman and photoluminescence spectroscopic detection of surface-bound Li(+)O2(-) defect sites in Li-doped ZnO nanocrystals derived from molecular precursors, *ChemPhysChem.* 12 (2011) 1189-1195.
- [141] J. J. Li, W. C. Hao, H. Z. Xu, T. M. Wang, J. Shi, Enhancement of ferromagnetism in Zn<sub>0.95</sub>Co<sub>0.05</sub>O films by lithium codoping, *J. Appl. Phys.* 106 (2009) 063915.
- [142] S. U. Awan, S. K. Hasanain, M. F. Bertino, G. H. Jaffari, Ferromagnetism in Li doped ZnO nanoparticles: the role of interstitial Li, *J. Appl. Phys.* 112 (2012) 103924.
- [143] A. L. Patterson, The Scherrer formula for X-ray particle size determination, *Phys. Rev.* 56 (1939), 978-982.

- [144] S. U. Awan, S. K. Hasanain, M. F. Bertino, G. H. Jaffari, Effects of substitutional Li on the ferromagnetic response of Li co-doped ZnO:Co nanoparticles, *J. Phys.:Condens. Matter* 25 (2013) 156005.
- [145] C. Rauch, W. Gehlhoff, M. R. Wagner, E. Malguth, G. Callsen, R. Kirste, B. Salameh, A. Hoffmann, S. Polarz, Y. Aksu, M. Driess, Lithium related deep and shallow acceptors in Li-doped ZnO nanocrystals, *J. Appl. Phys.* 107 (2010) 024311.
- [146] L. J. Brillson, Y. Lu, ZnO Schottky barriers and Ohmic contacts, *J. Appl. Phys.* 109 (2011) 121301.
- [147] <https://www.brukerafmprobes.com/p-3394-tesp.aspx> (Accessed 15 November 2017)
- [148] M. Lu, J. Song, M. Lu, M. Chen, Y. Gao, L. Chen, Z. L. Wang, Piezoelectric Nanogenerator Using p-Type ZnO Nanowire Arrays, *Nano Lett.*, 9 (2009) 1223-1227.
- [149] W. Han and F. M. Serry. Force spectroscopy with the atomic force microscope. *Application Note/Ww W.Agilent.comS* 2011.
- [150] J. H. McDonald, *Handbook of Biological Statistics* (3rd ed.), Sparky House Publishing, Baltimore, Maryland (2014) 140-144, Accessed 15th November 2017 as <http://www.biostathandbook.com/transformation.html> .
- [151] K. Benoit, *Linear regression models with logarithmic transformations*, London School of Economics, London (2011) 1-8. Accessed 15th November 2017 as <http://kenbenoit.net/assets/courses/ME104/logmodels2.pdf> .
- [152] N. L. Johnson, S. Kotz, N. Balakrishnan, Lognormal distributions, in: *Continuous univariate distributions*, vol. 1, Wiley Series in Probability and Mathematical Statistics: Applied Probability and Statistics (2nd ed.), John Wiley & Sons, New York, 1994, pp. 207-258.
- [153] <https://www.brukerafmprobes.com/p-3394-tesp.aspx> , accessed 13th December 2017.
- [154] C. Q. Chen, Y. Shi, Y. S. Zhang, J. Jhu, Y. J. Yan, Size dependence of Young's modulus in ZnO nanowires, *Phys. Rev. Lett.* 96 (2006) 075505.
- [155] A. Carvalho, A. Alkauskas, A. Pasquarello, A. K. Tagantsev, N. Setter, A hybrid density functional study of lithium in ZnO: stability, ionization levels, and diffusion, *Phys. Rev. B* 80 (2009) 195205.



- [156] J. J. Lander, Reactions of lithium as a donor and an acceptor in ZnO, *J. Phys. Chem. Solids* 15 (1960) 324-334.
- [157] K. E. Knutsen, K. M. Johansen, P. T. Neuvonen, B. G. Svensson, A. Y. Kuznetsov, Diffusion and configuration of Li in ZnO, *J. Appl. Phys.* 113 (2013) 023702.
- [158] G. Li, L. Yu, B. M. Hudak, Y. Chang, H. Baek, A. Sundararajan, D. R. Strachan, G. Yi, B. Guiton, Direct observation of Li diffusion in Li-doped ZnO nanowires, *Mater. Res. Express* 3 (2016) 054001.
- [159] G. Huang, C. Wang, J. Wang, First-principles study of diffusion of Li, Na, K and Ag in ZnO, *J. Phys.: Condens. Matter.* 21 (2009) 345802.
- [160] I. Stenger, M. A. Pinault-Thaury, T. Kociniowski, A. Lusso, E. Chikoidze, F. Jomard, Y. Dumont, J. Chevallier, J. Barjon, Impurity-to-band activation energy in phosphorus doped diamond, *J. Appl. Phys.* 114 (2013) 073711.
- [161] K. Hansen, E. Peiner, A. Schlachetzki, Dopant activation energy and hole effective mass in heavily Zn-doped InP, *J. Electron. Mater.* 23 (1994) 935-941.
- [162] D. Schechter, Carrier concentration and activation energy in heavily donor-doped silicon, *J. Appl. Phys.* 61 (1987) 591.
- [163] C. Liu, A. Yu, M. Peng, M. Song, W. Liu, Y. Zhang, J. Zhai, Improvement in the piezoelectric performance of a ZnO nanogenerator by a combination of chemical doping and interfacial modification, *J. Phys. Chem.* 120 (2016) 6971-6977.
- [164] K. C. Pradel, W. Wu, Y. Zhou, X. Wen, Y. Ding, Z. L. Wang, Piezoelectric effect in solution-grown p-type ZnO nanowires and films, *Nano Lett.* 13 (2013) 2647-2653.
- [165] H. M. A. Hamid, Z. Celik-Butler, Design and optimization of a MEMS triboelectric energy harvester for nano-sensor applications, 2019 IEEE Sensors Application Symposium, Nice, France, March 2019. DOI: 10.1109/SAS.2019.8706072

- [166] H. M. A. Hamid, Z. Celik-Butler, A novel MEMS triboelectric energy harvester and sensor with a high vibrational operating frequency and wide bandwidth fabricated using UV LIGA technique, submitted, 2020.
- [167] S. Niu, S. Wang, L. Lin, Y. Liu, Y. S. Zhou, Y. Hu, Z. L. Wang, Theoretical study of contact-mode triboelectric nanogenerators as an effective power source, *Energy Environ. Sci.* 6 (2013) 3576-3583.
- [168] S. Roundy, P. K. Wright, J. M. Rabaey, *Energy scavenging for wireless sensor networks*, Springer, Boston, MA, USA, 2004.
- [169] <https://www.mathworks.com/help/matlab/ref/ode15s.html> , (accessed 23rd March 2020)
- [170] N. Lobontiu, *Dynamics of microelectromechanical systems*, First ed., Springer, USA, 2007. DOI: 10.1007/978-0-387-68195-5
- [171] L. Wang, Investigation of the mechanical behavior of freestanding polycrystalline Au films deposited by evaporation and sputtering methods, PhD thesis, Auburn University, Auburn, Alabama, USA (2007).
- [172] W. N. Sharpe Jr., A. McAleavey, Tensile properties of LIGA Nickel, *SPIE Conf. on Mater. Dev. Character. in Micromachining* 3512 (1998) 130-137.
- [173] T. Fritz, H. S. Cho, K. J. Hemker, W. Mokwa, U. Schnakenberg, Characterization of electroplated Ni, *Microsyst. Technol.*, 9 (2002) 87-91.
- [174] S. Goyal, K. Srinivasan, G. Subbarayan, T. Siegmund, Estimating the yield strength of thin metal films through elastic-plastic buckling induced debonding, *IEEE Trans. Device Mater. Reliab.* 11 (2011) 358-361.
- [175] A. Datta, I. -Y. Eom, A. Dhar, P. Kuban, R. manor, I. Ahmad, S. Gangopadhyay, T. Dallas, M. Holtz, H. Temkin, P. K. Dasgupta, Microfabrication and characterization of Teflon AF-coated liquid core waveguide channels in silicon, *IEEE Sens. J.* 3 (2003) 788-795.
- [176] P. R. Resnick, W. H. Buck, Teflon® AF: a family of amorphous fluoropolymers with extraordinary properties. In: G. Hougham, P. E. Cassidy, K. Johns, T. Davidson (Eds.)

- Fluoropolymers 2, Topics in Applied Chemistry, Springer, Boston, MA (2002). DOI: [https://doi.org/10.1007/0-306-46919-7\\_2](https://doi.org/10.1007/0-306-46919-7_2)
- [177] I. E. Gonenli, Z. Çelik-Butler, D. P. Butler, Surface micromachined MEMS accelerometers on flexible polyimide substrate, *IEEE Sens. J.* 11 (2011), 2318-2325.
- [178] B. Thedjoisworo, D. Cheung, Comparison of effects of downstream H<sub>2</sub>- and O<sub>2</sub>- based plasmas on the removal of photoresists, silicon and silicon nitride, *J. Vac. Sci. Technol. B* 31 (2013) 021206.
- [179] Y. K. Pang, X. H. Li, M. X. Chen, C. B. Han, C. Zhang, Z. L. Wang, Triboelectric nanogenerators as a self-powered 3D acceleration sensor, *ACS Appl. Mater. Interfaces* 7 (2015) 19076-19082.
- [180] Y. Lee, S. Lee, H. Choi, K. Min, Analysis of vibration on an engine block caused by combustion in a diesel engine, *Int. J. Auto. Tech.* 20 (2019) 187-195.
- [181] Y. Wu, J. K. Yim, J. Liang, Z. Shao, M. Qi, J. Zhong, Z. Luo, X. Yan, M. Zhang, X. Wang, R. S. Fearing, R. J. Full, L. Lin, Insect-scale fast moving and ultrarobust soft robot, *Sci. Robotics* 4 (2019) eaax1594.
- [182] A. A. Alshuhri, T. P. Holsgrove, A. W. Miles, J. L. Cunningham, Development of a non-invasive diagnostic technique for acetabular component loosening in total hip replacements, *Med. Eng. Phys.* 000 (2015) 1-7.
- [183] I. Koene, R. Viitala, P. Kuosmanen, Internet of things based monitoring of large rotor vibration with a micromechanical systems accelerometer, *IEEE Access* 7 (2019) 92210-92219.
- [184] M. -L. Seol, J. -H. Woo, D. -I. Lee, H. Im, J. Hur, Y. -K. Choi, Nature-replicated nano-in-micro structures for triboelectric energy harvesting, *Small* 10 (2014) 3887-3894.
- [185] X. Y. Wei, G. Zhu, Z. L. Wang, Surface-charge engineering for high-performance triboelectric nanogenerator based on identical electrification materials, *Nano Energy* 10 (2014) 83-89.
- [186] L. Zhao, Q. Zheng, H. Ouyang, H. Li, L. Yan, B. Shi, Z. Li, A size-unlimited microstructure modification method for achieving high performance triboelectric nanogenerator, *Nano Energy* 28 (2016) 172-178.

- [187] I. –W. Tcho, W. –G. Kim, S. –B. Jeon, S. –J. Park, B. J. Lee, H. –K. Bae, D. Kim, Y. –K. Choi, Surface structural analysis of a friction layer for a triboelectric nanogenerator, *Nano Energy* 42 (2017) 34-42.
- [188] Y. Li, Z. Celik-Butler, D. P. Butler, A hybrid electrostatic micro-harvester incorporating in-plane overlap and gap closing mechanisms, *J. Micromech. Microeng.* 25 (2015) 035027.
- [189] Y. C. Shu, I. C. Lien, Analysis of power output for piezoelectric energy harvesting systems, *Smart Mater. Struct.* 15 (2006) 1499-1512.
- [190] R. K. Gupta, Q. Shi, L. Dhakar, T. Wang, C. H. Heng, C. Lee, Broadband energy harvester using non-linear polymer spring and electromagnetic/triboelectric hybrid mechanism, *Scientific Reports*, 7 (2017) 41396.
- [191] P. Basset, D. Galayko, A. Mahmood Paracha, F. Marty, A. Dudka, T. Bourouina, A batch-fabricated and electret-free silicon electrostatic vibration energy harvester, *J. Micromech. Microeng.* 19 (2009) 115025.
- [192] D. Shen, J. -H. Park, J. H. Noh, S. -Y. Choe, S. -H. Kim, H. C. Wickle III, D. -J. Kim, Micromachined PZT cantilever based on SOI structure for low frequency vibration energy harvesting, *Sens. Actuator A* 154 (2009) 103-108.
- [193] H. Liu, C. Lee, T. Kobayashi, C. J. Tay, C. Quan, Piezoelectric MEMS-based wideband energy harvesting systems using a frequency-up-conversion cantilever stopper, *Sens. Actuators, A* 186 (2012) 242–248.
- [194] Y. Tadesse, S. Zhang, S. Priya, Multimodal energy harvesting system: piezoelectric and electromagnetic, *J. Intell. Mater. Syst. Struct.* 20 (2008) 625–632.

## **Biographical Information**

H. M. Ashfiqul Hamid received his B.Sc. in Electrical and Electronic Engineering from Bangladesh University of Engineering and Technology (BUET) in 2014. He joined the University of Texas at Arlington (UTA) as a PhD student in 2015. His primary research focus includes the design, optimization, fabrication, and characterization of MEMS and NEMS scale piezoelectric, triboelectric and electrostatic energy harvesters and sensors. He also taught the EE 5343 (Silicon IC Fabrication Technology) course at UTA as an instructor. He has authored 4 conferences and 2 journal papers. He is the recipient of the ‘L3 Link Innovation Award’ in 2018 and ‘Best Graduate Project Award’ back to back in 2018 and 2019 in the Annual Innovation Day, organized by the College of Engineering, UTA. He also received the ‘Outstanding Graduate Teaching Associate Award’ from the Electrical Engineering Department in 2018 and the Summer Dissertation Fellowship from the College of Engineering, UTA in 2020. He was also a finalist for the ‘Best Student Poster Award’ in the 2017 IEEE Sensors Conference (Glasgow, UK). He received his PhD from the University of Texas at Arlington in 2020.